

Electronic Thesis and Dissertation Repository

2-12-2018 2:30 PM

Numerical studies of Electrohydrodynamic Flow Induced by Corona and Dielectric Barrier Discharges

Chaoao Shi
The University of Western Ontario

Supervisor
Adamiak, Kazimierz
The University of Western Ontario Co-Supervisor
Castle, G.S. Peter
The University of Western Ontario

Graduate Program in Electrical and Computer Engineering
A thesis submitted in partial fulfillment of the requirements for the degree in Master of
Engineering Science
© Chaoao Shi 2018

Follow this and additional works at: <https://ir.lib.uwo.ca/etd>



Part of the [Electrical and Electronics Commons](#), [Numerical Analysis and Computation Commons](#), and
the [Plasma and Beam Physics Commons](#)

Recommended Citation

Shi, Chaoao, "Numerical studies of Electrohydrodynamic Flow Induced by Corona and Dielectric Barrier Discharges" (2018). *Electronic Thesis and Dissertation Repository*. 5203.
<https://ir.lib.uwo.ca/etd/5203>

This Dissertation/Thesis is brought to you for free and open access by Scholarship@Western. It has been accepted for inclusion in Electronic Thesis and Dissertation Repository by an authorized administrator of Scholarship@Western. For more information, please contact wlsadmin@uwo.ca.

Abstract

Electrohydrodynamic (EHD) flow produced by gas discharges allows the control of airflow through electrostatic forces. Various promising applications of EHD can be considered, but this requires a deeper understanding of the physical mechanisms involved.

This thesis investigates the EHD flow generated by three forms of gas discharge. First, a multiple pin-plate EHD dryer associated with the positive corona discharge is studied using a stationary model. Second, the dynamics of a dielectric barrier discharge (DBD) plasma actuator is simulated with a time-dependent solver. Third, different configurations of the extended DBD are explored to enhance the EHD flow.

The results of the numerical simulations include the discharge current, space and surface charges, velocity profiles, EHD force and efficiency, which have been validated with the experimental data from collaborating researchers and those available in literature. This thesis provides a valuable insight into the physics of the EHD flow induced by gas discharge.

Keywords

Corona discharge, dielectric barrier discharge, extended DBD, electrohydrodynamics, numerical simulation, stationary model, finite element method, EHD dryer, DBD actuator, airflow control.

Co-Authorship Statement

This thesis is completed by C.A. Shi under supervision of Dr. Kazimierz Adamiak and Dr. G.S. Peter Castle. Parts of the material presented in Chapters 3 and 4 have been published in peer-reviewed journals or reported at academic conferences. The individual contributions of all authors of each included article are indicated.

Chapter 3

Article Title: “Electrically-induced mass transport in a multiple pin-plate electrohydrodynamic (EHD) dryer.”

Authors: C.A. Shi, A. Martynenko, T. Kudra, P. Wells, K. Adamiak, and G.S.P. Castle

Status: Published in *Journal of Food Engineering*, vol. 211, pp. 39-49 (2017)

The first draft of this article was written by C.A. Shi who also performed the numerical simulation and data analysis under the joint supervision of Dr. Adamiak and Dr. Castle. The relevant experiments were conducted by the collaborative research group led by Dr. Martynenko from the Department of Agriculture at Dalhousie University. Various drafts of this article were reviewed and modified by Dr. Adamiak, Dr. Castle and Dr. Martynenko.

Chapter 4

Article Title: “Numerical study of the characteristics of a dielectric barrier discharge plasma actuator”

Authors: Chaoao Shi, Kazimierz Adamiak, and G. S. Peter Castle

Status: Published in *Journal of Physics D: Applied Physics* (2018) 095201

Presented in *2017 Annual Meeting of Electrostatic Society of America (ESA)*

Presented in *International Symposium on Electrohydrodynamics (ISEHD)*

This article was written by C.A. Shi who also conducted the investigation and numerical analysis. Dr. Adamiak and Dr. Castle helped to understand of the concept of the airflow control using DBD and clarified several difficulties in model observations. Various manuscripts for conference proceedings as well as journal submission were reviewed and modified by Dr. Adamiak and Dr. Castle.

Acknowledgments

I would like to extend my deepest appreciation and gratitude to my supervisors, Dr. Adamiak and Dr. Castle, for their continuous encouragement, productive guidance, constructive criticism and considerate support throughout my Master's program. Their great insight and profound knowledge was of great help for me. Their consistent enthusiasm in research will always be remembered.

I have been extremely fortunate to have excellent and friendly colleagues at various stages of my thesis. My sincere thanks to Zhuangbo Feng for his help in numerical modeling and result interpretation, Peyman Dordizadeh for his teaching on conducting experiments and Dr. Chongshan Zhong for his fruitful discussion about the further investigation of the EHD dryer. My gratitude is also extended to all group members and new contacts I met at conferences, who made the research journey an enjoyable and a memorable experience.

I am also greatly indebted to the many professors, administrators, library staff, Faculty of Music and others at Western University. They provide varied and colorful events that allow me as an international student to explore the Canadian culture. Moreover, the financial support from NSERC of Canada and Western University, and the access to the COMSOL commercial software provided by CMC Microsystems are gratefully acknowledged.

It was a pleasant but not totally smooth experience over the past two years. An accident that occurred to me significantly disturbed my life. I would like to express my deepest gratitude to all those offered help and support, especially my supervisors. As the saying goes, "Some beautiful paths cannot be discovered without getting lost." The obstacles and mistakes eventually became my teachers.

Last but not least, I take this opportunity to thank my family who have continuously supported and encouraged me throughout my entire life. Without their love, trust, inspiration and support, I could not go so far in the journey of my life. I also want to express my heartfelt gratitude to my fiancée, Hanqing, who accompanied me with love, understanding and unconditional support during the years of study.

Table of Contents

Abstract	i
Co-Authorship Statement.....	ii
Acknowledgments.....	iii
Table of Contents	iv
List of Tables	ix
List of Figures	x
Nomenclature	xiv
Chapter 1	1
1 Introduction and Objectives	1
1.1 Plasma	1
1.1.1 Corona Discharge.....	2
1.1.2 Dielectric Barrier Discharge	3
1.2 Electrohydrodynamic Wind	4
1.2.1 General Description	4
1.2.2 Applications	4
1.3 Objectives of the Research.....	6
Chapter 2.....	8
2 Literature Review: Principles of Gas Discharge and EHD Flow.....	8
2.1 The Mechanisms of Gas Discharge	8
2.1.1 Breakdown Mechanism	8
2.1.2 Onset Voltage.....	9
2.1.3 Difference Between CD and DBD.....	9
2.2 Corona Discharge Enhanced Drying	10
2.2.1 Experimental Data	11

2.2.2	Numerical Simulation	12
2.3	Dielectric Barrier Discharge for Flow Control	13
2.3.1	Experimental Data	13
2.3.2	Numerical Simulation	17
2.4	Extended DBD	20
2.4.1	Experimental Data	21
2.4.2	Numerical Simulation	23
Chapter 3	25
3	Investigation of Corona Discharge in a Multiple Pin-plate Electrohydrodynamic Dryer	25
3.1	Introduction.....	25
3.2	Numerical Model	25
3.2.1	Geometry.....	26
3.2.2	Assumptions.....	26
3.2.3	Numerical Algorithm	27
3.3	Experimental Setup.....	29
3.3.1	Experimental Setup.....	29
3.3.2	Volt-Ampere Characteristics	30
3.3.3	Drying Experiments	31
3.4	Results.....	31
3.4.1	Electric Field on the Pin Tip	31
3.4.2	Volt-Ampere Characteristics	33
3.4.3	Voltage-Induced Total Air Mass Flow	36
3.4.4	Relationship Between Charge and Mass Transport	37
3.4.5	Airflow Pattern for Different Geometric Configurations	38
3.4.6	Total Air Mass Crossing Different Planes	43

3.5 Conclusions.....	44
Chapter 4.....	45
4 Numerical Study of the Characteristics of a Dielectric Barrier Discharge Plasma Actuator.....	45
4.1 Introduction.....	45
4.2 Methodology.....	46
4.2.1 Model of the Problem.....	46
4.2.2 Governing Equations.....	47
4.3 Electrical results.....	50
4.3.1 Electric Field Intensity.....	50
4.3.2 Electric Current.....	51
4.3.3 Effects of Voltage Level and Frequency.....	52
4.3.4 Space Charge Density.....	54
4.3.5 Surface Charge Density.....	57
4.3.6 Power Consumption.....	57
4.4 Fluid Flow Results.....	59
4.4.1 Evolution of Velocity Field.....	59
4.4.2 Effect of DBD.....	60
4.4.3 Effect of External Flow.....	63
4.4.4 Effect of Voltage Level.....	64
4.4.5 Effect of Frequency.....	65
4.4.6 Drag Reduction.....	66
4.4.7 Efficiency.....	67
4.5 Conclusions.....	68
Chapter 5.....	70
5 Numerical Investigation of Extended DBD for Flow Control.....	70

5.1 Introduction.....	70
5.2 Numerical Model	70
5.2.1 Geometry.....	70
5.2.2 Numerical Algorithm	71
5.2.3 Boundary Conditions	71
5.3 Simulation Results for the Model Studied by Moreau.....	72
5.3.1 Three-electrode Configuration.....	72
5.3.2 The Role of the Third Electrode	74
5.4 Simulation Results for the Model Studied by Nishida.....	75
5.4.1 Low DC Voltage.....	75
5.4.2 High DC Voltage	78
5.5 Conclusions.....	81
Chapter 6.....	83
6 Conclusions and Future Work.....	83
6.1 Summary	83
6.1.1 Corona Discharge.....	83
6.1.2 Dielectric Barrier Discharge	84
6.1.3 Extended DBD.....	85
6.2 Conclusions.....	85
6.3 Reflections on the Numerical Simulation.....	86
6.3.1 Modeling.....	86
6.3.2 Reducing the Calculation Time	88
6.3.3 Divergence	89
6.3.4 Validation of the Numerical Model	92
6.3.5 Prediction	93
6.4 Future Study.....	93

6.4.1 Corona Discharge for Drying..... 93

6.4.2 DBD Plasma Actuator..... 94

6.4.3 Extended DBD 94

6.4.4 Enhancing of the EHD flow..... 95

References..... 96

Appendices..... 102

Curriculum Vitae 115

List of Tables

Table 1: The slope coefficients of air mass transfer-voltage curves.....	37
Table 2: Physics and equations in the EHD dryer model	102
Table 3 Boundary conditions in EHD dryer model	103
Table 4 Physics and equations in the DBD actuator model.....	106
Table 5 Boundary conditions in the DBD actuator model.....	107
Table 6 Physics and equations in the extended DBD actuator model	111
Table 7 Boundary conditions in the extended DBD actuator model	111

List of Figures

Figure 1.1 Principle of a) a corona discharge based EHD dryer and b) a surface DBD actuator	3
Figure 2.1 Typical discharge current versus time and fast imaging of the developing plasma layer (images are for a top-view and opening gate width of 100 μ s).....	15
Figure 2.2 Schlieren images of DBD actuator jet supplied with 14.5 kV and 5 kHz at different delay times.	16
Figure 2.3 Sketch of a three-electrode discharge plasma actuator.....	20
Figure 2.4 View of the plasma sheet of a) the conventional DBD that is similar to extended DBD and b) sliding discharge.....	21
Figure 2.5 Experimental results of time-average flow field for a) sliding discharge and b) the extended DBD.....	22
Figure 2.6 Simulation results of time-average flow field for a) sliding discharge, b) conventional DBD and c) the extended DBD.....	23
Figure 3.1 Geometry of the model (a) 3D view, (b) analyzed area (2D view).....	26
Figure 3.2 Schematics of experimental setup for EHD drying.....	30
Figure 3.3 Distribution of electric field intensity (dashed line) and space charge density (solid line) on the pin tip.....	32
Figure 3.4 Distribution of the space charge density (C/m^3) in the area near the discharge electrode.....	33
Figure 3.5 Volt-ampere characteristics in different electrode configurations (a) 1 \times 1cm, (b) 2 \times 2 cm. Experimental data (circles) are shown vs. simulation results (dotted lines). The gap is increasing from the left (20 mm) to the right (40 mm).....	35

Figure 3.6 Air mass-voltage characteristics in different geometric configurations (simulation results).....	36
Figure 3.7 Current-induced air mass transport (lines, simulated for the gaps from 20 to 35 mm) and drying rate (circles, experimental data for the gaps from 20 to 40 mm) for 2×2 electrode.	38
Figure 3.8 Airflow in the 30 mm gap and 1×1 electrode configurations at 20 kV: (a) streamlines of velocity field, (b) velocity field.	39
Figure 3.9 Airflow in the 40 mm gap and 1×1 electrode configurations at 20 kV: (a) streamlines of velocity field, (b) velocity field.	40
Figure 3.10 Airflow in the 30 mm gap and 2×2 electrode configurations at 20 kV: (a) streamlines of velocity field, (b) velocity field, (c) schematic representation of vortices structure.....	41
Figure 3.11 Airflow in the 40 mm gap and 2×2 electrode configurations at 20 kV: (a) streamlines of velocity field, (b) velocity field.	42
Figure 3.12 Air mass transport characteristics in different geometries and 20 kV voltage....	43
Figure 4.1 Unscaled sketch of a DBD actuator.....	46
Figure 4.2 Electric field intensity on the electrode tip in the Laplacian and Poissonian models	50
Figure 4.3 Electric current and voltage applied on the electrode as a function of time.....	51
Figure 4.4 Maximum current versus voltage level and frequency.....	52
Figure 4.5 Definition of different phases in the electric field intensity and current on the tip of electrode in one voltage cycle.....	53
Figure 4.6 Distribution of space charge density [C/m^2] for $f=200$ Hz (left) and $f = 10$ kHz (right) with supplied voltage of 20 kV at the time of a) $1/6T$, b) $2/6T$, c) $3/6T$ and d) $4/6T$..	53

Figure 4.7 Electric field intensity and space charge density along the arc of electrode tip at the time of most intensive discharge for $V=16$ kV, 20 kV and 24 kV.	56
Figure 4.8 The evolution of total space charge in the calculation domain for the case of 20 kV, 1 kHz.	56
Figure 4.9 Time-dependent plot of charge density accumulated on dielectric wall.	57
Figure 4.10 Electrical power consumption versus voltage for different frequencies.	58
Figure 4.11 Evolution of velocity field at 2 ms, 5 ms, 10 ms, 15 ms, 20 ms and a steady state. External velocity equal to 1 m/s.	59
Figure 4.12 Velocity field in the wall boundary layer produced by DBD at 50 ms. External velocity equal to 1 m/s.	60
Figure 4.13 Velocity profiles along the lines perpendicular to the dielectric wall and downstream the discharge electrode.	60
Figure 4.14 Time variation of the velocity at different positions.	61
Figure 4.15 Velocity profiles along the lines parallel to the dielectric wall.	61
Figure 4.16 Velocity profiles along the line perpendicular to the dielectric wall 15 mm downstream from the discharge electrode.	63
Figure 4.17 Velocity profiles along the line 1 mm above the dielectric wall with different external flows for the 20 kV, 1 kHz case.	63
Figure 4.18 The effects of voltage level on the maximum value of enhancement velocity with different external flows (1 kHz).	65
Figure 4.19 The effects of frequency on the maximum value of enhancement velocity with different external flows (22 kV)	65
Figure 4.20 a) Forces acting on the dielectric surface and b) total drag force for different conditions calculated at 1 kHz.	66

Figure 4.21 Efficiency of a DBD actuator when the external flow is 1 m/s.....	68
Figure 5.1 Unscaled sketch of the extended DBD actuator in two configurations.....	71
Figure 5.2 Current waveform in the first five voltage cycles when the DC voltage equal to 0 kV and 4 kV.....	73
Figure 5.3 Time-dependent plot of the space charge density on the electrode (1).	73
Figure 5.4 Time-averaged velocity of the EHD wind along the vertical line $X=5$ mm from the edge of the active electrode for the DC voltage equal to 0 kV and 4 kV.	74
Figure 5.5 Unscaled sketch of the two-electrode actuator. The electrode (2) is connected to a DC voltage of 4 kV.....	75
Figure 5.6 Electric field intensity on the tip of the electrode (3).....	76
Figure 5.7 The electric field contributed by the DC electrode on the electrode (1) tip.	76
Figure 5.8 The current waveform in the first 5 cycles regardless of the DC voltage ranging from 0 kV to 10 kV.....	77
Figure 5.9 Time-averaged velocity field regardless of the DC voltage ranging from 0 kV to 10 kV.....	77
Figure 5.10 Electric lines of force over the domain at one time point.....	78
Figure 5.11 Current waveform in the first 5 cycles when $V_{dc}=20$ kV.....	78
Figure 5.12 Time-dependent plot of the surface charge density on the dielectric plate.	79
Figure 5.13 Time-averaged velocity field when $V_{dc}=20$ kV.	80
Figure 5.14 EHD force induced by the simple DBD and the extended DBD in one typical cycle.	81

Nomenclature

A	cross-section area, m^2
b	ionic mobility, $\text{m}^2/(\text{V}\cdot\text{s})$
C	constant in Eq. 1, $1/(\Omega\cdot\text{V})$
D	ion diffusion coefficient, m^2/s
d	distance between electrodes, m
E	electric field strength, V/m
E_0	Peek's value, V/m
E_{x0}	x components of the Laplacian electric field intensity, V/m
E_{y0}	y components of the Laplacian electric field intensity, V/m
E_x	x components of the Poissonian electric field intensity, V/m
E_y	y components of the Poissonian electric field intensity, V/m
F	electric body force, N
f_{AC}	frequency of the applied voltage, Hz
g	electrode geometry parameter, $1/\text{m}$
I	current, A
J	drift current density, A/m^2
P	pressure, Pa
Pe	electrical power, W
Pm	mechanical power, W

Q	air mass flux, $\text{g}/(\text{s}\cdot\text{m}^2)$
R	radius of discharge electrode, cm
u	velocity, m/s
V	voltage, V
V_o	onset voltage, V
V_{ap}	electric potential on the AC electrode, V
V_{dc}	electric potential on the DC electrode, V
w	width of the system, m
z	vertical coordinate, m

Greek symbols:

ε_o	dielectric constant of free space ($8.85\cdot 10^{-12}$ F/m)
μ	gas viscosity, Pa·s
μ_c	ion mobility, $\text{m}^2 /(\text{s}\cdot\text{volt})$
ρ	gas density, kg/m^3
ρ_c	space charge density, C/m^3
ρ_s	surface charge density, C/m^2
Φ	electrical potential, V
τ	stress tensor, MPa
η	electromechanical energy conversion efficiency
∇	nabla operator

Chapter 1

1 Introduction and Objectives

The main concepts considered in this thesis including plasma, corona discharge, dielectric barrier discharge and electrohydrodynamic flow have been introduced in this Chapter. The objectives of the research have also been described.

1.1 Plasma

In the past 300 years, the utilization of fossil fuels, electronics and semiconductors have brought three technology revolutions based on steam power, electric power and information technology, respectively. The subsequent commercialization of these technologies rewrote the material conditions of human existence and also reshaped culture, society and even human nature. Historically speaking, civilization progresses due to the developments of technology, which usually follow the breakthroughs in basic research.

Over the past few decades, more and more basic research has been done in the field of plasma. The interest in plasma can be traced back to our ancestors' curiosity in fire, lightning and the sun. However, this curiosity always turned into nature worship because people did not have sophisticated tools that are required for studying plasma in those times. Nowadays, with the availability of cutting-edge facilities and large-scale computation, the basic research on plasma has been significantly pushed forward.

Plasma, the most common state of matter in the universe, is a gas that has been energized to break down into charged particles. It exhibits complicated and rich physical phenomena, including numerous chemical reactions, ultraviolet radiation, electric wind and interactions with materials. It has been widely used in various applications, such as material processing, medical disinfection, water purification, microelectronics fabrication, electrostatic precipitation, propulsion engines, etc. Studying plasma not only promotes technological development, but also critically enhances the understanding of stars, atoms and those matters in the plasma state. This would help to reveal hidden principles of the universe. Discoveries and innovations in plasma would possibly play the

role of a trigger of a chain of numerous and unpredictable changes that may profoundly transform the human society again.

There are several ways to generate plasma, but all include pumping the gas with energy. In a star, large amounts of gas are “condensed” by the tremendous gravitational force into a tight space. At some point, the nuclei of atoms are squeezed so tight that would lead to nuclear fusion. The enormous energy released by fusion keeps ionizing the atoms and forming plasma. Similarly, a spark in gas may also create plasma. It is relatively easier to do this in a vacuum chamber with very low density of ions and electrons than in a normal atmospheric pressure. Different forms of plasma are dependent on the type of gas and the amount of energy absorbed for ionization. In this thesis, only the plasmas produced by the passage of electric current through gases, which is a common way to create plasma in the laboratory, are investigated and discussed.

1.1.1 Corona Discharge

The name corona comes from the Latin word for “crown”. During stormy weather at sea, sailors noticed the appearance of flamelike reddish or bluish lights on the tops of masts that wore this light like a crown or halo on the head [1]. Many years later, the same phenomena were observed in the high-voltage experiments conducted in the laboratory. These were referred to as corona in align with previous reports of Latin-oriented scholars.

Corona is defined by ASTM standards as a visible electrical discharge that partially bridges the insulation between conductors. It is created by a transient gaseous ionization occurring in an insulation system, if the local electric field exceeds a critical value when some electrons break free from, but coexist with, atoms and molecules. The impressive glow and streamers of corona are the visualization of photons, which are mainly released in the recombination of electrons and positive ions to form neutral atoms. Although most of the research attention has been given to ionized particles, neutral particles play an important role in ionization, energy loss, and diffusion processes in a discharge.

Corona discharge consumes energy but in a very economic way. The voltage required for corona discharge is usually a few kV, but the current is very low, 10^{-10} to 10^{-4} A. This leads to relatively low energy consumption.

1.1.2 Dielectric Barrier Discharge

Plasma discharges do not necessarily take place between a pair of conducting electrodes or surfaces. They can occur between two electrodes separated by an insulating dielectric layer. The process normally uses high alternating voltage with a frequency ranging from a few hundred to a few thousand hertz. This type of electrical discharge is called a Dielectric Barrier Discharge (DBD). The presence of the dielectric layer restrains the discharge intensity and makes it more controllable. The properties of DBD can be easily manipulated by the geometry, dielectric material and the applied AC voltage.

DBD can be generated either in a volume (VDBD) or on a surface (SDBD). The typical VDBD devices are made in planar or cylindrical configurations. The former uses parallel conducting plates separated by a dielectric, and the latter uses coaxial metallic electrodes with a dielectric tube between them. For SDBD, it is typically made out of two strip electrodes, one exposed and one buried in a dielectric plate. The discharge occurs on the top of the dielectric surface. The plasma appears in an area around the exposed electrode and does not usually extend over the entire surface of dielectric plate.

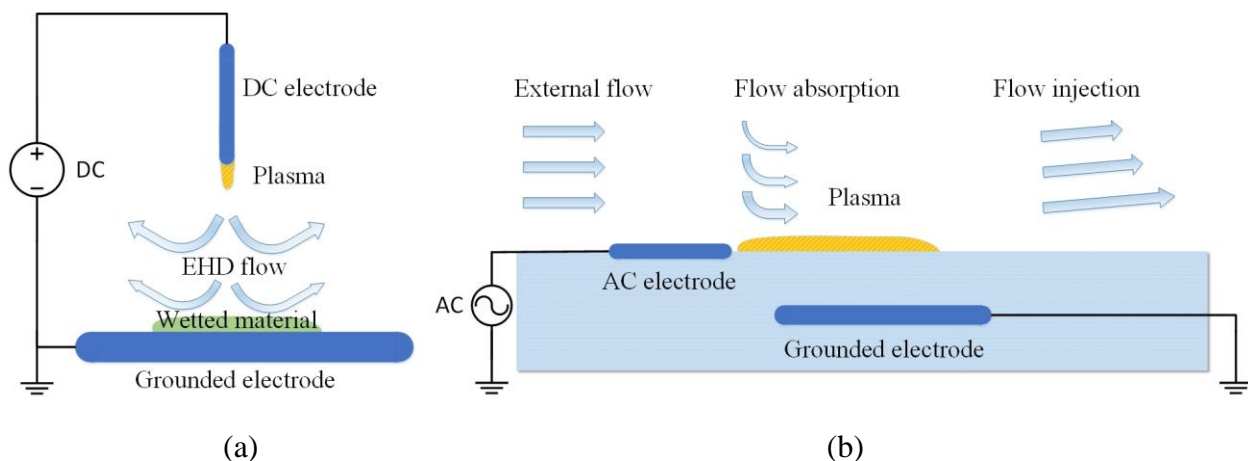


Figure 1.1 Principle of a) a corona discharge based EHD dryer and b) a surface DBD actuator

1.2 Electrohydrodynamic Wind

1.2.1 General Description

The presence of plasma is always accompanied by electrohydrodynamic (EHD) flow – or, more colloquially, “ionic wind” – which results from the motion of ionized particles and their interaction with the electric field and the surrounding fluid. As the cloud of ions in plasma moves away from the discharge electrode, it collides with the surrounding air molecules, forming a wind along the direction of discharge. The phenomenon of ionic air movement in corona discharge was observed and studied from the earliest day of the discovery of electricity in the early 18th Century. Normally, EHD wind associated with plasma discharge in the laboratory has a low-velocity of a few meters per second. It directly converts electrical energy into kinetic energy without moving parts, which offers an essential advantage in various applications.

1.2.2 Applications

Electrohydrodynamics focuses on the dynamics of electrically charged fluids. Practical fields of interest of EHD include the ionocrafts, plasma actuators, electrostatic precipitators, EHD cooling systems and electrical generators.

a) Ionocrafts: Ionocraft, also known as “EHD lifter”, is a kind of vertical takeoff EHD thruster, which firstly appeared in the 1960s. They are usually lightweight vehicles made of sharp wire, aluminum foil and balsa wood. As voltage is applied, the plasma discharge occurs on the sharp wire. The ionized particles migrate in the electric field, because they are strongly repelled by the wire and attracted to the aluminum foil. Due to the collisions between ions and surrounding neutral air molecules, a wind is generated along the direction of particle movement, which creates a reaction force on the ionocraft in the opposite direction. The ionocraft will lift off and hover with increased voltage. This technology offers interesting possibilities particularly for small devices of aviation applications within the atmosphere.

b) Plasma actuators: Intensive research has been conducted to develop plasma actuators with the purpose to modify boundary layers over airfoils in aerodynamics applications. In these applications, EHD wind receives very close attention because of its ability to modify the boundary-layer properties such as velocity profile, drag force and the stability of airflow. The main advantage

of plasma actuators over other systems is that they do not require a mechanical actuator that is dependent on motors or fuel, and they can be flexibly controlled by the applied voltage with a very short reaction time. The applications of plasma actuators will be extremely promising once the EHD flow with large velocities can be generated.

c) Electrostatic precipitators: An electrostatic precipitator is a device that charges particles suspended in a flowing gas and then collects them through electrostatic attraction. It has been widely used in industry to remove polluting fine particles from exhaust fumes because of its high total particle collection efficiency (>99.9%). In certain situations, the EHD flow generated by the corona discharge has significant influence on the electrostatic precipitator performance. It remains an open field for future studies to eliminate an undesired increase of turbulence caused by EHD flow.

d) EHD cooling systems: As electronic devices become miniaturized and more power consuming, there is not enough surface for the heat to disperse quickly. EHD cooling systems are proposed to address the challenge of efficiently removing heat from electronic elements in small spaces. They have no moving parts, function with low vibration and noise emission, consume low energy and can be easily controlled by varying the applied voltage. EHD cooling systems can be manufactured with a simple structure in different sizes, from large plates to microscale devices, and can withstand extreme conditions.

e) Electrical generators: As a charged fluid flows through a shaped electrostatic field, the energy will be added to the system and can be extracted from the potential difference between electrodes. Despite of its low energy conversion efficiency, compared with traditional electromagnetic machines, EHD power generator merits attention because of its safety, stability and unexplored possibilities in practical situations.

In general, the application of EHD wind offers human the ability to control the wind through electrostatic force, as a fundamental element of nature, to achieve lift, modify boundary layers, conduct heat and generate power. The desired functionality is achieved by injecting charged particles into neutral fluid and then leveraging them with electric field, which has already been mastered and can be easily controlled. However, EHD wind also has some undesired side effects,

such as ozone generation and low electrical-to-mechanical energy conversion efficiency, which limit its practical applications.

1.3 Objectives of the Research

The recent trends of research on EHD flows generated by plasma discharge is to compare the experimental data with simulation results, which would provide a valuable understanding of the physics of EHD flow and benefit the design of EHD devices at the same time. The research work presented in this thesis includes numerical studies of different types of plasma discharge and the coexisting EHD flow. The main objectives of this research include:

1.3.1 Developing Numerical Models for EHD Flows Generated by Plasma Discharge

Numerical models have been developed for EHD flows generated by different types of plasma discharge, including corona, DBD and extended DBD discharges. Despite the existence of a number of previously published numerical studies on the plasma discharge and EHD flow, most of them were constrained to simple configurations. This study proposes some numerical models having relatively more realistic configurations. The results of numerical simulation have been validated with the previously published experimental data and a close agreement was observed. In addition, some parameters of the numerical model have been optimized to improve the performance of EHD systems. This is extremely important for the industrial scaling and practical applications of EHD technology.

1.3.2 Study of a Multiple Pin-plate EHD Dryer Based on Corona Discharge

The EHD flow produces air motion at a very small pressure difference and can be used to enhance a drying technology for the preservation of food. Although experimental verifications were conducted for this drying concept, a thorough study of interactions between the electric field, space charge and secondary airflow could not be fully understood without numerical simulation. In this study, a numerical model of corona discharge for multiple pin-plate EHD dryer is proposed. The objective of this study is to study both theoretically and experimentally the current-voltage characteristics, airflow patterns, charge and mass transport in a multiple-pin EHD dryer.

1.3.3 Numerical Study of a DBD Plasma Actuator

The DBD plasma actuator can be applied to control air flow within its boundary layer. DBD is a complicated process involving the periodic variation of electric field, space charge transport, surface charge accumulation, air flow motion and ionic reactions. Despite the large number of publications, the DBD plasma and EHD flow have not yet been fully understood. This thesis uses the proposed two-species numerical model to get a better insight into the physics of DBD, and to predict the electrohydrodynamic properties of a DBD actuator for airflow control.

1.3.4 Numerical Study of an Extended DBD Plasma Actuator

The extended DBD has one more DC electrode mounted on the dielectric plate, as compared with the traditional DBD that has just two electrodes. It has been suggested that the third electrode possibly can enhance the discharge intensity in the negative phase and increase the velocity of EHD wind. This study aims to have a deeper understanding of how strong this influence is and which parameters are the most important.

Chapter 2

2 Literature Review: Principles of Gas Discharge and EHD Flow

The EHD flow induced by gas discharges have been explored and intensely studied over the past decades. The concepts of gas discharge are presented in this Chapter. The experimental and simulation research results on EHD enhanced drying and airflow control are reviewed.

2.1 The Mechanisms of Gas Discharge

2.1.1 Breakdown Mechanism

The theory of electric breakdown in uniform field was developed by Townsend, who used the electron-avalanche concept [2]. He showed that a free electron with high kinetic energy could eject an electron from a neutral gas molecule on their collision. Each ionizing electron moving in a sufficiently high electric field can generate an exponential number of free electrons through such collisions. This electron avalanche causes gas ionization and ultimately the breakdown between electrodes. The thickness of an ionization zone is usually in the order of a fraction of a millimeter, but the whole gap between electrodes is filled with ions drifting in the electric field. The breakdown in nature is composed of discrete sparks, despite the fact that it seems consecutive in the corona discharge that is produced by a high voltage not high enough to generate arc discharges.

The electrons, as well as negative ions, produced in the discharge are absorbed by the anode, and the positive ions left drift towards the cathode. The ionic bombardment at the surface of cathode liberates additional electrons [3]. This process is called the secondary electron emission. In addition, other mechanisms are found to be able to supply free electrons. For example, photoelectric emission caused by the photons in the ionization process or from an outer radiation source can also excite gas molecules and release free electrons [4].

Besides the Townsend avalanche theory, a streamer theory was also proposed independently by Meek and Raether [5, 6]. This theory uses the streamer discharge mechanism to explain the breakdown process in highly nonuniform electric field configurations, for instance, having dielectric boundaries. Since streamer discharges are neglected in the numerical models proposed

in this thesis, the streamer theory is not discussed here. The related information can be found in [3, 7].

2.1.2 Onset Voltage

In a laboratory, the discharge is usually generated by applying a high voltage between electrodes. The value of the onset voltage significantly depends on the geometric configurations. In the case of the same applied voltage, the electric field is much stronger near a sharper electrode. The breakdown occurs because once the electric field reaches above a threshold, a free electron can get sufficient energy to start the Townsend avalanche. Therefore, the curvature radius of electrodes dictates the onset voltage. Moreover, the distance between electrodes also affects the electric field and thus changes the value of onset voltage.

The onset voltage also depends on the probability of electron regeneration at the cathode surface (secondary electron emission) [3]. For this reason, the onset voltage is expected to be impacted by the characteristics of the electrode surfaces, and a difference should exist when the metallic electrodes are replaced by dielectric ones. In the early pioneering studies on corona discharge, Mason found that the onset voltage between dielectric voids was 10 to 20 percent lower than that between metallic electrodes with the same gap separation [8].

In addition, other conditions, such as the existence of an outside radiation source and the type of gas, could also renew the supply of free electrons and, therefore, influence the value of onset voltage.

2.1.3 Difference Between CD and DBD

The dielectric barrier discharge is different from the corona discharge mainly due to the presence of a dielectric plate between the anode and cathode. The ions generated in the discharge will be accumulated on the dielectric surface. DC voltage cannot be used to produce DBD because the accumulated surface charge will balance the electric field and eventually stops the discharge process [9]. Moreover, in the case of an extremely high DC voltage, the dielectric breakdown might occur and destroy the whole system, just like what may happen in a failed capacitor. As a result, alternating voltage or pulses are applied on the electrodes in DBD. The voltage can be varied from

a traditional sinusoidal waveform to a specifically designed triangle or trapezoidal waveform such as investigated in [10, 11].

The characteristics of the dielectric surface can influence the discharge mechanisms. In the system with metallic electrodes, a breakdown taking place at any point on the electrode will determine the overall electric field and charge distribution, which will prevent the occurrence of another simultaneous breakdown. However, when a discharge occurs in the system with the dielectric plate, the charge distribution on some portion of the dielectric plate remains unaffected because of the low mobility of the surface charges [12]. As a result, simultaneous discharges can and do occur at different sites in DBD.

The dielectric barrier discharge in nature is asymmetric. When the system is supplied with a sinusoidal voltage, streamer discharges dominate the positive half-cycle while the Trichel pulses appear in the negative half-cycle. The streamer discharges are characterized by high current pulses with relatively large time gaps. On the contrary, the Trichel pulses have small magnitude current pulses, but they are very dense [13]. This asymmetric properties can be explained by the difference between positive ions and electrons, which are released into space in the positive and negative half-cycle, respectively [3].

In DBD, the additional electric field contributed by released charges reduces the overall electric field intensity in the same discharge phase, whereas, it is enhanced in the opposite phase. This mechanism makes drifting ions fluctuate in each cycle. Therefore, one way to increase the velocity of EHD flow is to eliminate the fluctuations that consume a significant portion of energy by applying a specifically designed voltage waveform [14].

2.2 Corona Discharge Enhanced Drying

Besides freezing, drying is another commonly used technology for long-term preservation of perishable foods. The natural drying is known from an early history of humanity, but industrial drying requires techniques for process intensification [15]. Contact and radiant heating, and forced convection of hot gas are the most used techniques, accelerating mass transport from food containing moisture. Contact heating is efficient, but energy consuming and may lead to the food degradation due to the material overheating [16]. Thin-layer convective drying seems to be the

most economical option, since exposing of the material surface to air flow would require a very small pressure difference and relatively low degree of thermal energy [17].

One of the simplest techniques to produce air motion at a very small pressure difference is based on the electrohydrodynamic (EHD) flow caused by electrical discharges [18]. The ions migrated in the electric field impinge on the wet material deposited on the surface of collecting electrode, and facilitate the evaporation process. Compared with conventional thermal drying, EHD drying has the advantages of lower energy consumption [19], higher rehydration ratio [20], preserved color [21], and preserved vitamin C content [22].

2.2.1 Experimental Data

EHD drying has been proven efficient for different materials, such as water evaporation [23], fully wetted glass beads [24], apple slices [25], tomato slices [26], carrots and miscanthus [27].

The critical issue for improving the performance of an EHD dryer is selection of electrode geometry, in particular the curvature of the discharge electrode (typically pins or wires), the distance between these pins/wires and the gap between the discharge electrode and the material surface. It was found in the early study of electrical engineering that a sharper electrode has a higher discharge current at the same voltage [28-30]. Regrettably, the effect of the other two parameters have not be systematically investigated, because most previous experiments were constrained to simple configurations, like a single pin/wire discharge system. Although the performance of single-pin electrode has a higher local drying rate than multi-pin electrodes [31, 32], it has no potential in industrial application [33]. In the multi-pin discharge system, the interference effects of neighboring objects and edge effects need to be considered [33]. In order to reach the best performance, the geometry of electrodes in EHD dryer need to be optimized [34].

Mass transfer in drying can be categorized into different modes dependent on the moisture content of the materials [35]. The observed drying curves reveals the difference between drying mechanisms of fully wetted material, such as the bed of glass beads [36, 37], and of partially wetted material, such as mushrooms [38]. Related background information of mechanisms of drying such as driving forces, mass transfer, effects of internal and external conditions can be found in the literature [35, 39, 40]. In addition, forced convection significantly affects the convective mass

transfer. On one hand, forced external airflow could remove the water vapor from the liquid-gas interface, and facilitate the EHD drying process [41]. On the other hand, forced external airflow would suppress the effects of EHD drying, if it dominates over the EHD flow [32].

EHD drying is not considered as an energy-efficient technology because only 0.6–1.4% of electric energy is converted into kinetic energy of EHD flow [42]. However, EHD is mainly a surface phenomenon and the consumed energy is targeted for moisture removal [43]. Drifting ions disturb the boundary layer and significantly facilitate the evaporation process. To further explain the lost energy, a few hypotheses have been proposed. The hypothesis of heat dissipation is not convincing because significant temperature drop in the boundary layer at liquid-gas interface was found in experiments [44, 45]. Another hypothesis is that most of the energy is transformed into the electrochemical potential of excited particles. The phenomenon of enhanced corrosion and oxidation at metal-gas interface supports this hypothesis very well [42].

The EHD flow velocity is usually measured by a vane or hot-wire anemometer located outside the discharge gap. The drying rate is calculated by the reduction of water content in a dried sample over a period of time [41]. It is extremely hard in an experiment to investigate the local electric field, space charge distribution and other significant factors contributing to drying. In addition, intrusive sensor probes inevitably interfere with the electric field and EHD flow. Even non-intrusive optical techniques, such as particle image velocimetry (PIV), would affect fields in experiment by injecting charged tracer particles. A thorough study of the complicated electrically induced transport phenomena is possible only through numerical simulation.

2.2.2 Numerical Simulation

Numerical studies on EHD flow generated by corona discharge have been reported since the 1960s [46, 47]. It was followed by a number of detailed investigations on EHD flow in electrostatic precipitators [48-51]. However, few numerical studies are available in the literature regarding EHD-enhanced drying because of the complicated interactions among the electric field, gas ionization, gas flow and mass transfer. The complexity of drying can be furthered by considering the liquid-gas interface [52, 53].

Most of the proposed numerical models adopt single wire/pin electrode because of its simplicity [54-56]. Those studies focus on the proof of the EHD concept and its feasibility, but not on the design of an industrial device. It is expected that multiple electrodes should be used to satisfy the needs of mass production [32].

Numerical simulation of a multiple discharge electrode system revealed existence of local vortices, induced by interaction of ionic and air streams [57, 58]. These vortices could be essential in their interaction with the boundary layer [59, 60]. Mahmoudi et al. [60] put forward the hypothesis of interaction between ionic wind vortices and forced airflow, which could affect charge and mass transport at the boundary layer. Although these local vortices are inherently three-dimensional phenomena, they were oversimplified as a two-dimensional flow in the previous numerical studies.

It is well known that the properties of EHD flows depend on the polarity of the corona discharge. Compared with the DC positive corona discharge, the negative corona discharge is less stable and produces a much larger turbulence intensity [55]. As a result, the numerical studies of EHD flows usually adopt the positive corona discharge to reasonably simplify the problem [61, 62].

2.3 Dielectric Barrier Discharge for Flow Control

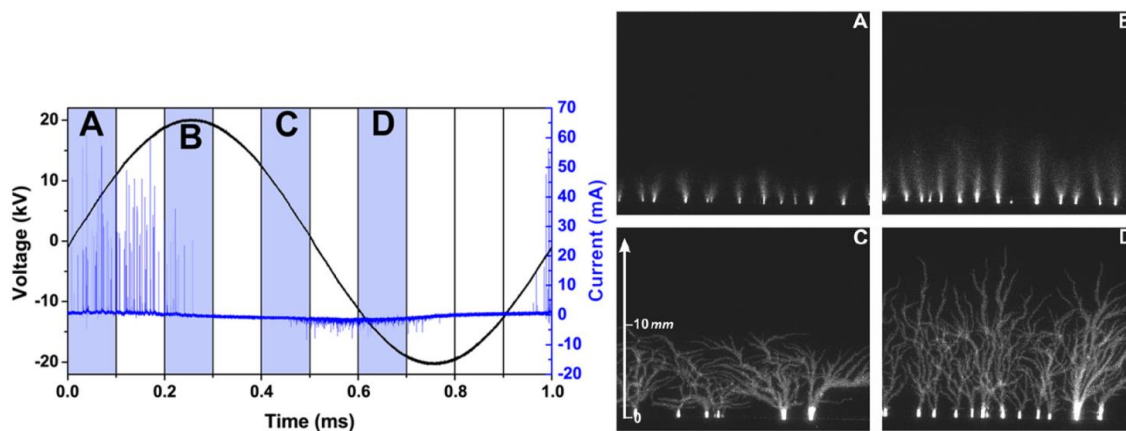
Actuators for controlling the flow boundary layer were initially based on the corona discharge. Later, it was shown that the dielectric barrier discharge (DBD) is more advantageous [63, 64]. The dielectric layer (e.g. Kapton, Teflon, Glass, Plexiglas or PMMA) limits the value of the discharge current resulting in low energy consumption. The charged species generated by the discharge collide with neutral air molecules, and then produce a wall-jet like stream known as EHD wind. DBD actuators can be conveniently manipulated and installed at the surface of linear or curved objects, and their dynamic properties can be easily controlled by the geometry and the applied electrical signals [65-69]. The advantage of DBD actuators over other systems is that they do not involve moving parts and can be almost instantaneously controlled.

2.3.1 Experimental Data

The results of experimental flow control studies were reviewed in [13, 70]. Different configurations of the actuator supplied by a high voltage periodic sine waveform have been investigated experimentally trying to find an optimum device configuration. Various

characteristics have also been closely examined in order to have a better insight into the physical aspects of DBD actuators. These included the current, plasma extension, velocity profiles, EHD force, power consumption and efficiency. Sophisticated experimental tools offer the possibility of not only taking the time-average measurements, but also focusing on the time and space resolved results.

Current is usually measured by recording the voltage across a non-inductive shunt resistor (100 Ω), or with the help of a high-bandwidth current transformer [13]. This discharge current is composed of a displacement current, due to the capacitance of the system, and a conduction current due to the movement of charged species. The displacement current is commonly subtracted in the graph of discharge current. Figure 2.1a shows a typical current waveform in a DBD actuator supplied with 20 kV, 1 kHz voltage source [71]. Although the surface discharge looks like a uniform glow, in reality it is composed of many micro-discharges. As shown in Figure 2.1b these discharges start from individual spots along the electrode with current peaks up to 70 mA. The average current is usually a few mA. Moreover, two different discharge regimes can be observed: a streamer discharge appears in the positive half-cycle and a glow-like discharge occurs in the negative half-cycle [72]. As shown in Figure 2.1b, the propagation of streamers can extend from the discharge electrode up to about 20 mm, while the glow discharges extend up to 10 mm with a plume shape. It has also been proved that DBD acts differently in velocity induction during the positive and negative half-cycles [73]. Some works were also reported to optimize the voltage waveform in order to increase the induced velocity [71]. However, the mechanism of different discharge regimes in DBD has not yet been fully explained.



(a) (b)

Figure 2.1 Typical discharge current versus time and fast imaging of the developing plasma layer (images are for a top-view and opening gate width of 100 μ s). [71]

The current, as the signature of discharge intensity, can be significantly affected by the geometry of the actuator (such as electrode curvature, electrode gap, dielectric thickness), the supplied voltage (magnitude, frequency, waveform for instance), the environmental conditions (such as temperature, humidity and pressure), and the material of electrode and dielectric plate.

The typical energy consumption of a plasma actuator ranges from 0.1 to a few W/cm (per electrode unit length). It was observed that the electric power consumption is a linear function of the frequency and a power function of voltage with the order ranging from 2 up to 3.5 [73]. The electric power sustains the plasma, but a large portion is lost in the dielectric heating especially at a low voltage condition [74]. Therefore, research interests were aroused in investigating the barrier thickness and dielectric materials besides the geometry of electrodes and applied voltage in order to reduce the dissipated energy [75, 76].

The DBD actuator produces an EHD wind along the dielectric plate. As shown in Figure 2.2, starting vortices are generated during the ignition phase, they move downstream along the discharge electrode and eventually evolve into a wall jet of a few mm thickness in the steady state. The maximum velocity is a few m/s (7 m/s in [68], for instance) and always located at the discharge extension of 5-15mm downstream the discharge electrode and about 1 mm above the dielectric. It was reported that the maximum velocity increases with frequency as well as with voltage, because of the enhanced ionization and more intensive collisions between ions and gas molecules [73]. In addition, there is a suction effect above the discharge in the vertical direction caused by the flow acceleration in the horizontal direction. The evolution of EHD wind usually takes more than 30 ms before it reaches a steady state. The formation process is discussed in detail in [77].

Although the EHD wind seems steady, there are strong oscillations of the flow at some spatial locations [78]. This experiment has also proved that DBD does not equally contribute to the production of velocity during the positive and negative half-cycles. The glow discharges in the negative half-cycle affects velocity stronger than the streamer discharges (3.6 m/s) in the positive half-cycle (2.4 m/s).

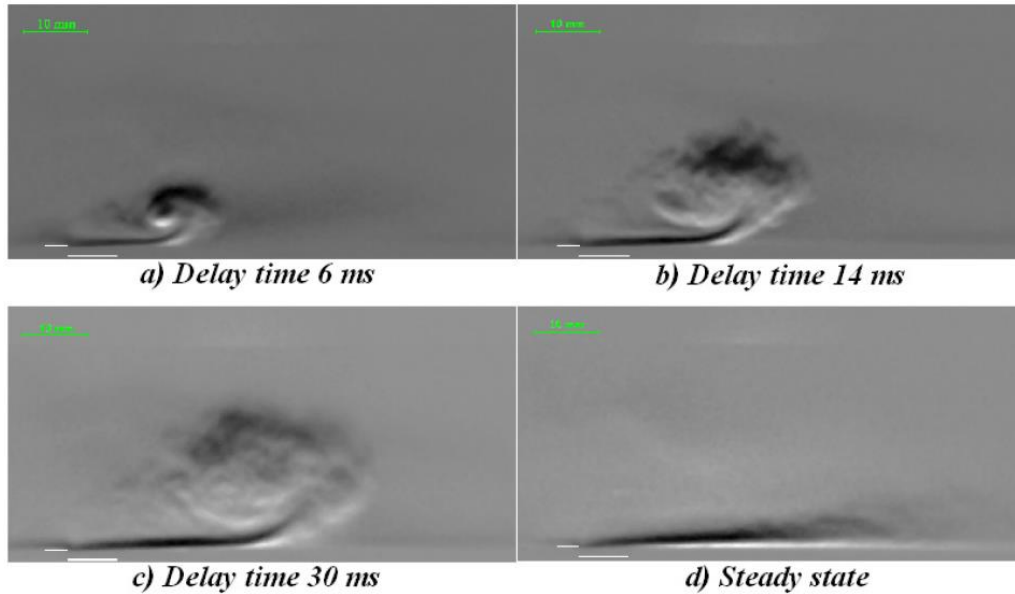


Figure 2.2 Schlieren images of DBD actuator jet supplied with 14.5 kV and 5 kHz at different delay times. [69]

The EHD wind is produced by the EHD force, which in experiments can either be calculated from velocity measurements [79] or estimated by a mechanical system [80]. It was reported by Benard et al. [79] that the horizontal component of the time-average EHD force is 34.2 mN/m and the vertical component is much smaller (-0.37 mN/m), while the instant horizontal EHD force can be up to 350 mN/m. It was also found that the negative and positive half-cycles produce the EHD force in the same direction, but only the negative half-cycle can sustainably overcome the drag force to accelerate the flow in the boundary layer [80]. The drag force consists of the pressure force due to the pressure difference and the viscous force due to the friction on the dielectric plate. However, the pressure contribution is usually neglected in the calculations compared with the viscous contribution [79]. According to Kriegseis et al. [81], a significant portion of energy is dissipated by the viscous effect, and about 30% of the induced momentum was consumed by the wall friction. In order to estimate the DBD actuator's ability to accelerate the airflow, researchers always investigate the thrust force, which is defined as the EHD force minus the drag force. It is shown that the thrust increases with voltage and is almost proportional to the consumed power [68].

DBD actuators transform electric energy into kinetic energy and the electromechanical efficiency is a useful parameter to evaluate the performance of DBD actuators. The efficiency is very low (0.1% ~ 1 %), but DBD actuators are still effective in modifying the boundary layers because of their ability to introduce small perturbations. Moreover, it is observed that the efficiency increases with power consumption and then it reaches a plateau.

In addition, surface DBD can also be generated by a nanosecond high voltage pulse, but this will be not discussed in this thesis. A related review was presented by Adamovich [82].

2.3.2 Numerical Simulation

There have also been a few attempts to simulate this problem numerically to get a better understanding of the physical aspects of the gas discharge. This also helps to find a way to improve the performance of DBD actuators.

The most important challenge in the modeling of a DBD actuator is that the gas discharge is a very complicated process involving several hundred ionic reactions [83], which requires extraordinarily high computing capability. Therefore, any realistic numerical algorithm must adopt a significant problem simplification.

It is common to assume just three ionic species (electrons, positive and negative ions) and a few ionic reactions [84-86]. However, it is still very difficult to simulate the randomly distributed, highly luminous and concentrated micro-discharges in DBD that involve streamers and Trichel pulses. Since these pulses have very steep rise time and very narrow width [87-89], the process must be simulated using a very small time step, which leads to extremely long calculations. The complexity of a numerical model is exponentially increasing by considering all physical mechanisms including ionization, recombination, attachment, detachment, particle mobility and electron temperature. In addition, these published papers [84-86] usually focus on the study of current and EHD force, but lack the adequate investigation of velocity profiles as well as the validation of kinetic characteristics. Another simplification is to assume that the DBD operates in the inert gases or pure nitrogen without the presence of negative ions [90-94]. These attempts include the generation, decay, drift and diffusion of electrons and positive ions, but always ignore some essential characteristics of DBD actuators. For example, the self-limiting corona-to-spark

transition is highlighted, but the velocity field is not included in [64, 90]; a simplifying assumption of a constant voltage pulse were made without considering the effects of frequency on DBD [92]; the development of plasma cannot be resolved in [93]. Moreover, due to the absence of negative ions, the “push-push” mode of EHD flow in the negative half-cycle cannot be accurately modeled according to Likhanskii et al. [85]. Therefore, a different two-species approximation that only concerns negative and positive ions is proposed [95]. Although the asymmetric properties in the positive and negative half-cycles are not captured, it proved to be sufficiently accurate to calculate the EHD wind in some engineering applications.

Other challenges in modeling DBD actuators include the ionization processes, the space charge drift, effects of photons, surface charge accumulation and secondary electrons emission from the dielectric wall.

The ionization of DBD is mainly caused by the avalanche of free electrons [96]. This process can be modeled by solving the continuity equation for charged species coupled with Poisson equation for electrical field, where the constants are determined empirically [85]. This method is a very direct depiction of the related physical mechanisms and takes a long time for calculation. Even so, the spatial and temporal scales of individual micro-discharges are still numerically irresolvable [90], and the calculation of a sudden micro-discharge would generate nonphysical oscillations known as Gibbs phenomenon in the numerical simulations [90, 97]. There is another approximation of the ionization that space charges are injected from the electrode surface when the field exceeds the threshold, which is based on Kaptzov’s hypothesis and Peek’s formula [95]. The movement of space charges is also governed by the classic drift-diffusion theory. This model significantly reduces the calculating time and provides an adequately accurate description of DBD, which is especially useful for engineering applications in air flow control.

According to Golubovskill et al. [98], in the inert gases or pure nitrogen, the photoemission is negligible because the energy of photons in the visible range is too small to cause the emission of electrons. However, in air, this phenomenon could be significant and result in the acceleration of ion propagation, which is associated with streamers in the positive half-cycle [99]. Regrettably but unavoidably, the mechanisms of photoemission and photoionization are neglected in almost all the numerical models because of their complexity, except for [100]. As a result, even for such an

idealistic model, there are only a few spikes in the positive half-cycle (streamer regime), which are different from numerous micro-discharges experimentally observed (Figure 2.1) [86].

The surface charge accumulated on the dielectric surface plays the key role in understanding the DBD discharge [85]. It alters the electric field within the discharge domain and prevents DBD transition to spark. The surface charge accumulation, recombination, diffusion and desorption can be sophisticatedly modeled from the view of atom collisions [98], but it is beyond the scope of the present numerical studies. To simplify the problem, the diffusion and desorption of surface charges can be neglected. The instantaneous recombination of charged particles is plausibly and widely accepted [84-86, 90-94]. Although the charging of the dielectric has been included in most of the proposed DBD models, the simulation results about surface charge have not been discussed, probably due to the difficulty of presenting its time varying distribution on the dielectric barrier.

Secondary electron emission is another important mechanism of the interaction between charged particles and the dielectric. In the positive half-cycle, the electrons can be pulled from the surface and can then initiate avalanche ionization [85]. The presence of electrons, as well as secondary electron emission, plays an important role in forming streamers in the positive half-cycle, which is distinguished from the glow discharge in the negative one [86]. The emission rate depends on the positive charge density above the emission surface, electric field intensity and dielectric material [96].

Moreover, the momentum transfer between charged particles and air molecules produces the EHD wind. There is a large difference between the time constants involved in the electrical and mechanical phenomena. For example, for the electrical effects it is possible to consider a short interval of the order of a few voltage half-cycles, while the longer mechanical time constant would require simulations for 30-50 cycles. Although different models have been proposed to provide insights into the physics of the discharge, almost all the previous efforts in modeling DBD mentioned above lack a validation study especially in the field of kinetic characteristics.

To push forward the understanding of DBD, a consistent, comprehensive and physically based numerical model should be built up. In order to make such calculations feasible, this thesis proposes a simplified model that only includes positive and negative ions, and ignores the presence

of free electrons, ionic reactions and secondary electron emission. In other words, the discharge pulses contributed by electrons and photons are completely neglected. The computational difficulties increase with the range of included mechanisms, the complexity of boundary conditions, the geometric size of numerical model, the number of computational elements, and the time steps adopted to reach a quasi-steady state of the discharge.

2.4 Extended DBD

A conventional DBD actuator cannot be used in large-scale applications because of its limited plasma range (up to 2 cm) and low EHD wind velocity (up to 8 m/s). In order to extend the surface of actuation and enhance the thrust, a new geometry based on a three-electrode configuration is proposed with the inspiration coming from earlier investigations for other applications [101-103]. It has two air-exposed electrodes mounted on the upper side of the dielectric plate and one electrode encapsulated to avoid the formation of undesired discharge below the plate, as shown in Figure 2.3. Different types of power supply connection can generate different three-electrode discharges that have different electrical and mechanical properties.

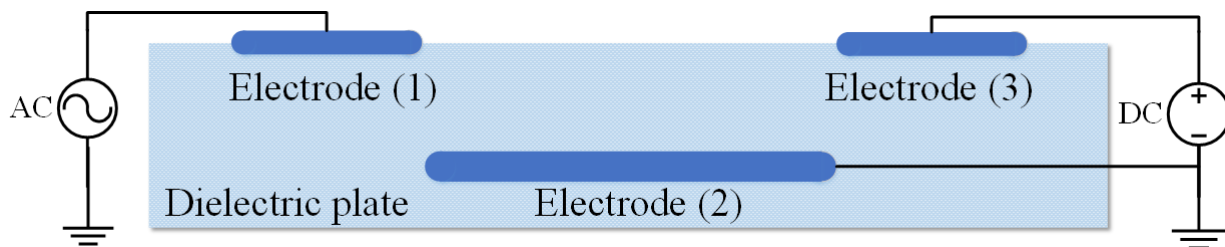


Figure 2.3 Sketch of a three-electrode discharge plasma actuator.

Typically, electrode (1) is supplied with an AC high voltage (V_{ac}), electrode (2) is grounded and electrode (3) is connected to a DC high voltage (V_{dc}). If V_{dc} is negative, it generates a luminescent plasma sheet that covers the whole electrode gap (sliding discharge) [13, 104, 105]. If V_{dc} is positive, the discharge essentially looks like a conventional DBD but the velocity is slightly enhanced (extended DBD) [105, 106]. These discharges depend largely on the polarity of DC voltage because of the asymmetric properties of DBD generated between electrode (1) and the other two electrodes [14].

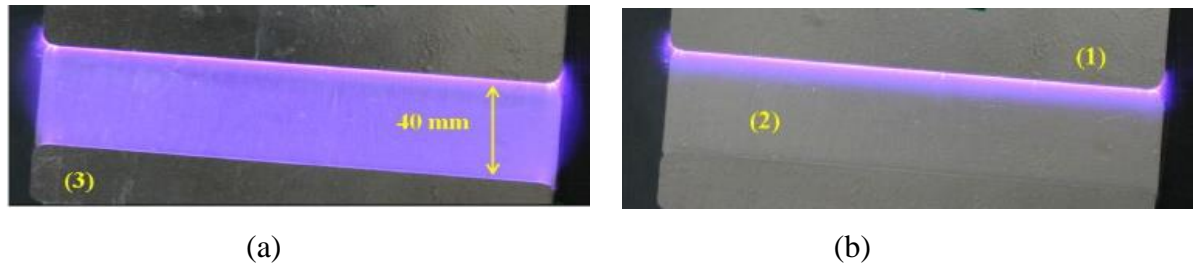


Figure 2.4 View of the plasma sheet of a) the conventional DBD that is similar to extended DBD and b) sliding discharge. [107]

As previously stated, the power supply connected to each electrode may have different configurations. Moreau and Sosa investigated the configuration where electrode (1) is supplied with an AC voltage and both electrode (2) and (3) are connected to a DC voltage [107-109]. Huimin replaced the sinusoidal waveform voltage on electrode (1) with a microsecond pulse power supply [110]. Guo tested the design where two air-exposed electrodes are linked to a switch that connects electrode (1) to a negative DC voltage source and electrode (3) to one positive in each half-cycle separately [111]. Debian exchanged the power supply connected to electrodes (1) and (2) [106]. All these attempts produce different types of discharges that may have some advantages under different conditions and specific applications. However, in this thesis, only a few configurations of the extended DBD is studied and compared with the conventional DBD.

2.4.1 Experimental Data

The experiments on the three-electrode discharges can be categorized into two groups: sliding discharge and extended DBD, which depends on the polarity of the applied DC voltage [13].

A sliding discharge can cover the entire gap between the exposed electrodes, which is substantially different from the conventional DBD. The generated flow, experimentally observed, shows a jet perpendicular to the dielectric plate. It is caused by the collision of two EHD flows, one due to the DBD between electrodes (1) and (2), and the second mainly resulting from negative ions drift produced by the ionization near the electrode (3), supplied with negative DC high voltage [107]. Compared with the conventional two-electrode DBD, the added third electrode in the sliding discharge not only accelerates the original EHD flow by intensifying the electric field, but also induces a counter EHD flow, if the negative DC voltage exceeds some critical threshold. Although the sliding discharge enhances the total body force and velocity field, the direction of EHD wind

is not along the dielectric wall [105]. Therefore, it might not be able to modify the boundary layer as efficiently as a conventional DBD. In addition, the jet direction can be modified by changing the value of DC voltage applied to electrode (3), and this voltage is limited to prevent occurring of arc and sparks that might damage the whole structure. A sliding discharge does not necessary produce an upward deflection of the jet. In a different configuration proposed by Debian [106], the EHD wind could be in fully parallel to the wall under certain conditions. The jet behavior has not been explained from the physical viewpoint of the plasma dynamics.

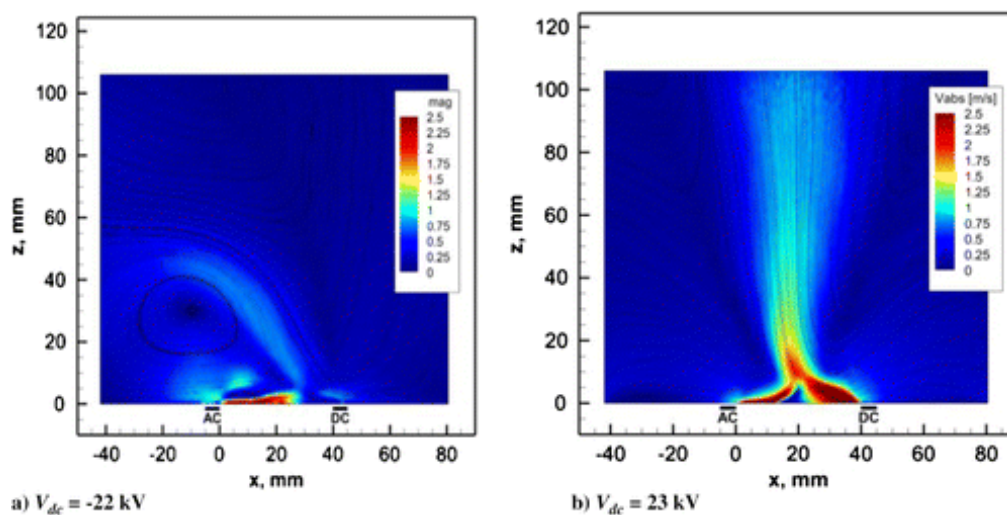


Figure 2.5 Experimental results of time-average flow field for a) sliding discharge and b) the extended DBD. [105]

The plasma layer of the extended DBD is confined to the region close to discharge electrode supplied with a high AC voltage. This is very similar to the conventional DBD regarding EHD wind topology, plasma stability and current waveform, but extended DBD shows the enhancement of mechanical performances. The velocity profiles of the extended DBD are slightly thicker and the maximum velocity higher to some degree, because of the increase of the body force ranging from 10% to 45% under different conditions [106]. There is no vertical jet in the extended DBD investigated by Debian [106], but it appears in another experiment conducted by Nishida [105]. The reason has not been discussed or explained yet.

Generally speaking, the three-electrode plasma device changes the actuator performance by exploiting the asymmetric properties of DBD in the positive and negative half-cycles. A negative DC voltage enhances the streamer propagation in the positive half-cycle and suppresses the corona

discharge in the negative half-cycle. A counter EHD wind is also induced by the discharge on electrode (3). On the contrary, a positive DC voltage enhances the negative corona and depresses the positive streamer discharges on electrode (1) [108].

2.4.2 Numerical Simulation

Although intensive studies have been conducted on DBD, only a few experimental papers referred to above have been published on the three-electrode discharges regardless of their various configurations. This limits the numerical studies due to the lack of sufficient and reliable experimental results. In addition, the complexity of modeling three-electrode discharges is much higher than that of modeling a conventional DBD, because the asymmetric properties of discharges are reinforced by the DC electrode [14]. To author's best knowledge, only Nishida's group successfully investigated a tri-electrode plasma actuator using a numerical model [104, 105, 112].

Nishida used the plasma fluid model proposed by Boeuf et al. [113], which takes into consideration three species and a few ionic reactions. Despite the quantitative discrepancies compared with experiments, the simulation reproduced the qualitative characteristics of the sliding discharge and the extended DBD (Figure 2.6). Time-averaged thrust is observed as a function of DC voltage. It has also been found that once the DC voltage exceeds a critical value, the vertical thrust appears and, at the same time, the horizontal thrust drastically decreases. This results in the production of a jet, which was perpendicular to the wall. In addition, the time-resolved and spatial body force was closely examined and provided an insight into the physical mechanism of the counter EHD flow produced by the DC electrode.

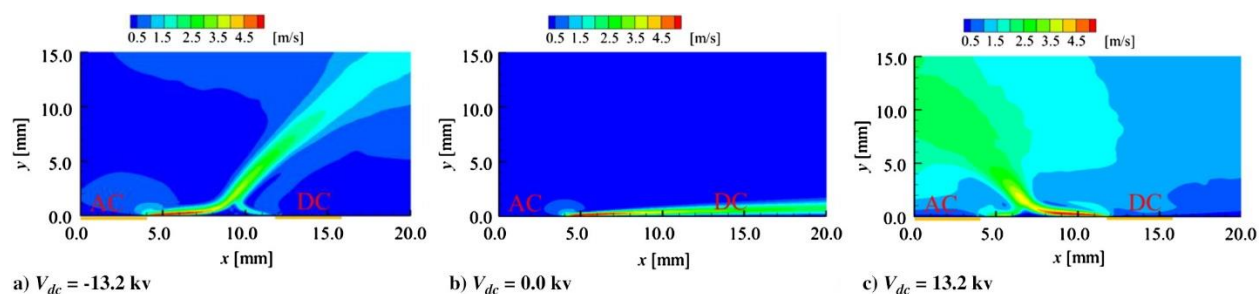


Figure 2.6 Simulation results of time-average flow field for a) sliding discharge, b) conventional DBD and c) the extended DBD. [105]

However, this numerical study was not completely satisfactory. First of all, the direction of simulated jet was not consistent with the experimental observation as in Figure 2.5. Secondly, the current waveform was not calculated and validated with the experimental data available in literature. Thirdly, the surface charge accumulated on the dielectric, which significantly affects the plasma behavior, was not investigated. Moreover, the vertical jet in the extended DBD numerically and experimentally observed in [105] does not exist in the work of other groups [106-108], and a further explanation is needed.

Chapter 3

3 Investigation of Corona Discharge in a Multiple Pin-plate Electrohydrodynamic Dryer

3.1 Introduction

Electrohydrodynamic (EHD) dryers have been researched and developed due to their potential for accelerating rehydration and preserving nutrition values. In this Chapter, the numerical model of a multiple pin-plate EHD dryer is investigated by the author and the simulation results are compared with the data from experiments conducted by A. Martynenko, T. Kudra and P. Wells from Dalhousie University.

The numerical model quantifies the electric field intensity, space charge density and mass transport in an EHD dryer based on corona discharge. A few idealizing assumptions have been adopted to save the calculation time. The results show that corona current strongly depends on voltage and geometry. This conclusion has been validated by the experimental results, which proves the correctness of the model. The air mass flux, which is associated with the drying rate, is also presented. The results indicate that the drying rate can be controlled by the applied voltage as well as the discharge current.

In order to optimize the performance of a multiple pin-plate EHD dryer, different geometries have been studied with varying distances between pins as well as the gap between the electrode and plate. The numerical results of EHD flow predict velocity profile and occurrence of aerodynamic vortices in the air. The patterns of EHD flow in different geometries are also presented.

3.2 Numerical Model

The numerical model for the corona discharge in a pin matrix-plate configuration developed previously [114] has now been extended to quantify the effects of voltage, current, gap and spacing between pins. All simulations were based on the COMSOL (Comsol Inc, MA, USA) commercial software package based on the Finite Element Method (FEM). Although it may be less accurate than the numerical algorithms based on a hybrid FEM-Method of Characteristics, it runs much faster and is applicable for 3D geometries [115].

3.2.1 Geometry

The discharge electrode resembles the uniform array of identical pins attached to a conducting plate and supplied with a positive high voltage. In the theoretical model, it is assumed that pins form an infinite array with identical discharge cells. Each pin is a cylinder of given length and radius, ended with a conical section and a hemispherical tip. The pin length, pin-to-pin spacing and air gap between the discharge and collecting electrodes were considered as the model variables. Given the symmetry of the geometry, only a triangular prism zone of a single pin electrode was analyzed. Figure 3.1 shows how 10×10 mm triangular prism with the single pin was adopted to analyze infinite pin matrix with 20×20 mm cells. The origin of the x, y and z coordinate system coincided with the pin tip.

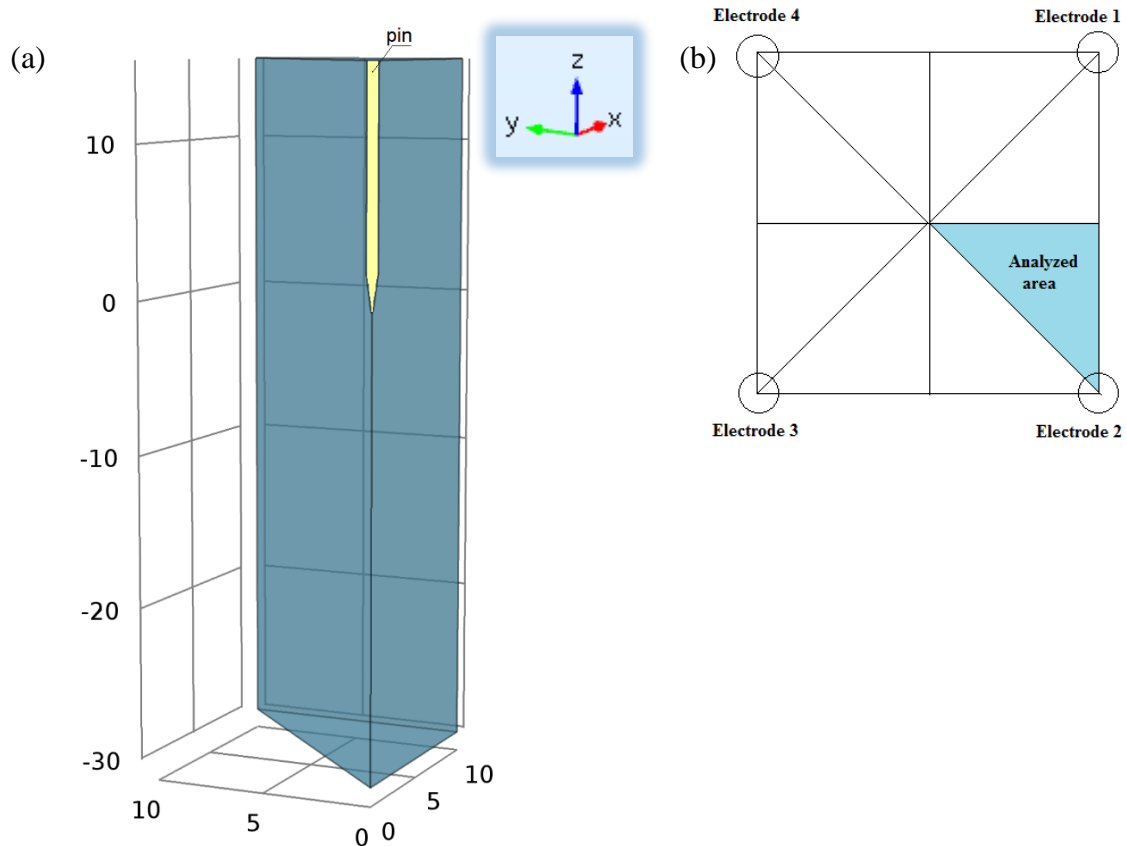


Figure 3.1 Geometry of the model (a) 3D view, (b) analyzed area (2D view).

3.2.2 Assumptions

Material:

- A. Moisture and temperature gradients within the material are negligible.
- B. Diffusion of liquid water within the material is negligible as compared to capillary flow.
- C. Free water evaporation takes place from the material surface.

Fluid:

- D. The difference in humidity of air, impinging and rebounding from the material, is constant.
- E. Laminar airflow conditions exist at the material surface.
- F. No aerodynamic interaction exists between neighboring convective airflows.
- G. Charge convection due to forced airflow does not exist.

Corona:

- H. Varying humidity and elevated temperature do not affect the corona discharge.
- I. Ionic reactions in ionization zone, leading to generation of numerous ions species, are neglected.

3.2.3 Numerical Algorithm

The complete numerical model of the EHD flow generated by corona discharge is highly complex [116]. However, a simplified model of this process, based on the so-called single-species approximation, is usually sufficiently accurate in engineering applications [114]. This simplified approach is based on the assumption that outside the ionization region, called the drift zone, there is just one ionic species having the same polarity as the polarity of voltage applied to the discharge electrode. In this case, the following charge transport equation governs the ion density distribution:

$$\nabla \cdot (\rho_c b \mathbf{E} - D \nabla \rho_c) = 0 \quad (3.1)$$

where ρ_c is the ionic space charge density, \mathbf{E} is the electric field intensity vector, b is the ion mobility, and D stands for the ion diffusion coefficient. Both k and D values can be determined experimentally as they represent not only dominant ionized O_2 molecule, but also other ions and even charged clusters of the water vapor. The effect of the charge diffusion is often neglected, and the ion mobility is typically assumed to be equal to $2.2 \times 10^{-4} \text{ m}^2/(\text{V} \cdot \text{s})$.

The electric field intensity can be given as a gradient of the electric potential, which satisfies the Poisson equation

$$\nabla^2 V = -\frac{\rho_c}{\varepsilon_o} \quad (3.2)$$

where V is the electric potential and ε_o is the gas permittivity equal to 8.85 nF/m.

Equations. (3) and (4) are mutually coupled, as the space charge density depends on the electric field intensity that is a function of the space charge. Both equations can be solved iteratively until convergence is reached.

The boundary conditions for the electric potential are trivial, as both electrodes (corona and ground) are equipotential. However, adopting certain boundary conditions for the space charge density is a major challenge. The so-called Kaptzov's hypothesis, that above the onset level the electric field on the surface of corona electrode remains constant, is commonly accepted. This value of electric field intensity can be calculated from Peek's formula

$$E_o = 3.1 \cdot 10^6 \cdot (1 + 0.308 / \sqrt{0.5R}) \quad (3.3)$$

where R is the radius of discharge electrode in cm.

Strictly speaking, this hypothesis is not exactly true [117], but its sufficient accuracy has been validated experimentally [114].

The flow pattern of ionic wind can be determined by solving the Navier-Stokes equation [62]

$$\nabla \cdot \mathbf{u} = 0 \quad (3.4)$$

$$\rho \left[\frac{\partial \mathbf{u}}{\partial t} + (\mathbf{u} \cdot \nabla) \mathbf{u} \right] = -\nabla P + \mu \nabla^2 \mathbf{u} + \mathbf{F} \quad (3.5)$$

where \mathbf{u} signifies the gas velocity vector, ρ is the gas density, μ is the gas viscosity, P stands for the pressure, and $\mathbf{F} = q\mathbf{E}$ represents the electric body force.

The walls of the triangular prism domain were set as the symmetry surfaces for an electric field, space charge density and laminar flow. Therefore, the computational model represents one unit of an infinite array of electrodes. As a result, the boundary conditions are: (1) zero normal derivative (Neumann) boundary condition for the electric potential and space charge density; and (2) zero normal velocity for the air flow.

3.3 Experimental Setup

Experimental study provided data for verification of the theoretical model, in particular volt-ampere characteristics and mass transfer as the function of electric current.

3.3.1 Experimental Setup

A lab-scale EHD convective dryer shown schematically in Figure 3.2 consists of the 40×20×20 cm drying chamber made from a transparent plastic housing, discharge and collecting (grounded) electrodes, computerized system for mass and current measurements, and high voltage power supply [41]. A multiple-pin discharge electrode was made from 1.5 cm long sharp stainless steel pins 1.35 mm in diameter, attached to the fiberglass plate 125×185×1.5 mm in the nodes of the square cells grid.

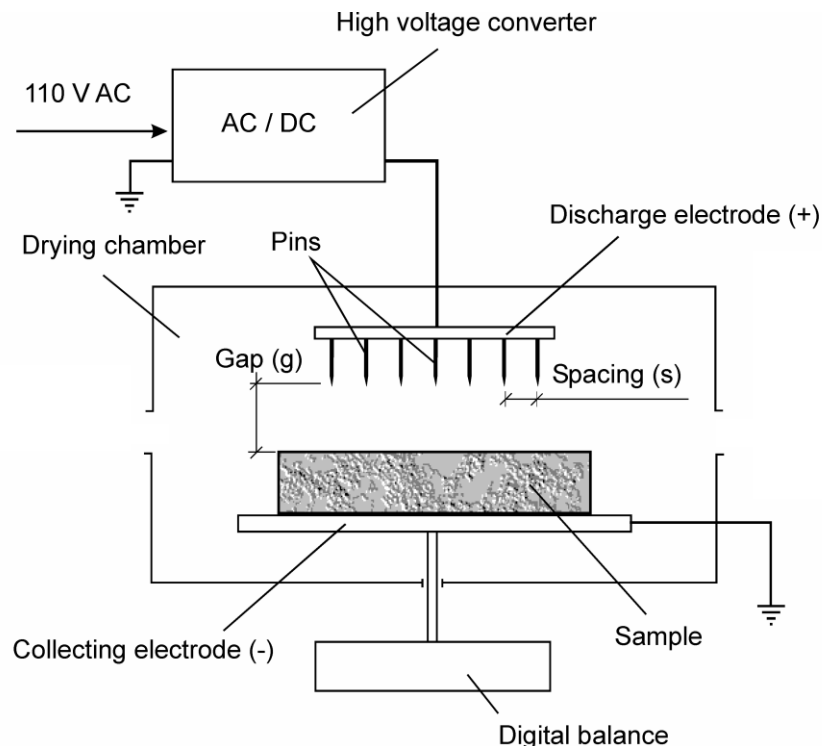


Figure 3.2 Schematics of experimental setup for EHD drying.

Two configurations of electrodes with different spacing between pins were investigated: one with 143 pins arranged in 10×12 rows with 1 cm square cells (1×1), and another with 42 pins arranged in 6×7 rows with 2 cm square cells (2×2). The gap between discharge and collecting electrodes was adjustable in the range from 2.0 to 4.0 cm. The discharge electrode was connected to the positive voltage, whereas the collecting solid aluminum plate electrode 125×200×1.5 mm was connected to the ground of the DC high voltage power supply (SPELLMAN, Model RHR20P10, USA). The instantaneous values of voltage and current were displayed on the control panel of a power supply and continuously recorded on the computer through a digital interface NI USB-6210 (National Instruments, USA). The experimental apparatus was located in the air-conditioned laboratory with temperature set at 20±°C and air humidity in the range 55-70%.

3.3.2 Volt-Ampere Characteristics

Volt-ampere characteristics of (1×1) and (2×2) electrodes with gaps in the range from 20 to 40 mm were studied by increasing the voltage in 1 kV increments and waiting about 3 min until current reached a constant value. Measurements started with inception voltage of 7 kV and ended

just before the electric breakdown. All measurements were done in triplicate with no material between electrodes, and results were then averaged for data processing.

3.3.3 Drying Experiments

The effect of EHD on the water evaporation rate was evaluated from drying experiments at the room temperature of $20\pm 1^\circ\text{C}$ and air humidity in the range 55-70%. The 25 g sample pack of 40 dry tissue paper $10\times 16\text{cm}$ were wetted with tap water to $50.0\pm 1.0\text{ g}$ and placed centrally on the surface of the collecting electrode. The surface area of wet sample was entirely exposed to ionic wind from the array of multi-pin electrode. Drying experiments were carried out for different combinations of voltages, configurations of discharge electrode (1×1) and (2×2), gaps (20, 25, 30, 35 and 40 mm). In this study both current and mass transfer were considered as output variables. Each experiment was carried out at constant voltage in the range of currents from 0 to 300 μA . Mass reduction of the wet material was determined with the top-loaded digital balance HCB1002 (Adam Equipment, Danbury, CT, USA) and continuously recorded through a USB interface to the computer. The duration of each drying experiment was set at one hour.

3.4 Results

3.4.1 Electric Field on the Pin Tip

For the pin tip radius of curvature $R=0.01\text{cm}$, the Peek's value of the onset electric field strength (Equation 3.3) is 167.0 kV/cm. Figure 3.3 shows the variation of the electric field intensity along the arc length as measured from the tip of the hemispherical electrode.

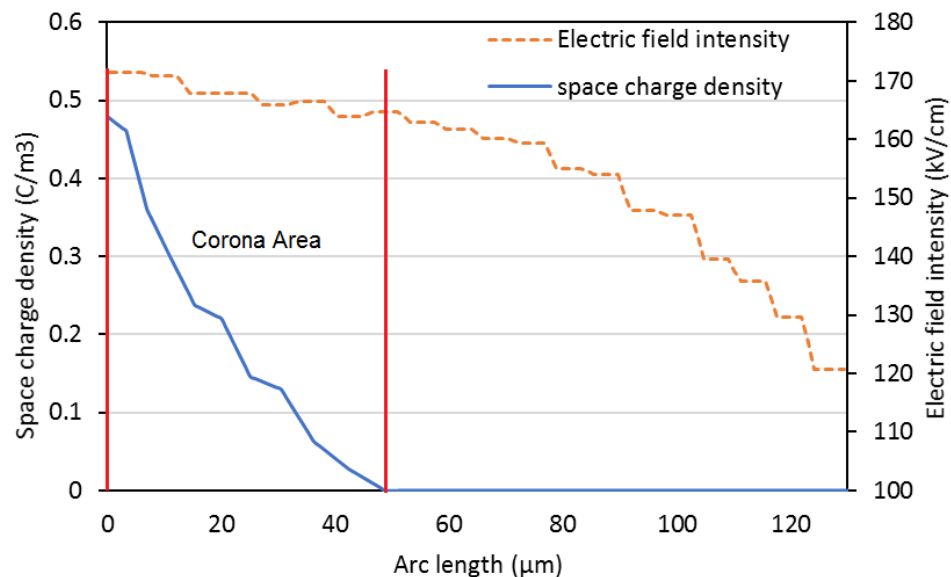


Figure 3.3 Distribution of electric field intensity (dashed line) and space charge density (solid line) on the pin tip.

It follows that electric field intensity decreases progressively with the distance from the tip of a single hemispherical pin of discharge electrode. The corona area (ionization region) is confined within $50 \mu\text{m}$ from the electrode tip. Simulation of the space charge density (dashed line) also shows that the ionic charges concentrate within $50 \mu\text{m}$ from the electrode tip. Graphical representation of the space charge density distribution along the z axis is shown in Figure 3.4. Charge density decreases smoothly in the volume surrounding the pin tip. In addition, the corona area will increase in volume as the voltage increases.

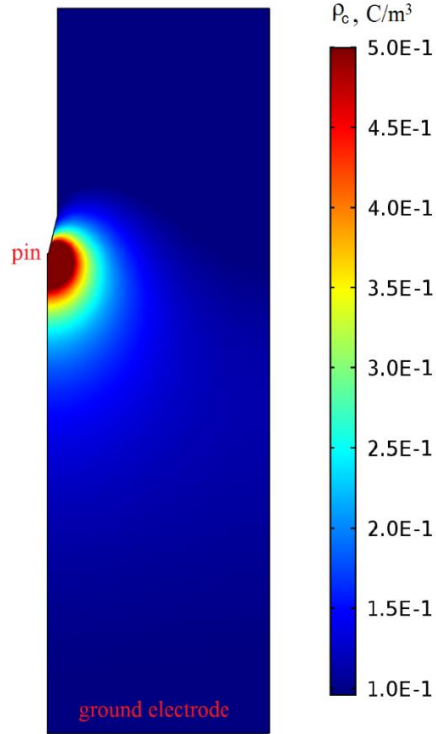


Figure 3.4 Distribution of the space charge density (C/m^3) in the area near the discharge electrode.

3.4.2 Volt-Ampere Characteristics

The current of a single-pin electrode has been computed using the Sato formula (Sato, 1980)

$$I = \iiint \frac{\rho_c b}{V_o} (E_x E_{x0} + E_y E_{y0}) dV \quad (3.6)$$

where ρ_c is the space charge density, b is the ion mobility, V_o is the electric potential applied to the pin, E_{x0}, E_{y0} represent the x and y components of Laplacian electric field intensity calculated without space charge, and E_x, E_y stand for the x and y components of the electric field intensity with consideration of the influence of the charged particles (Poissonian component).

The total current was determined by multiplying the single electrode current by the number of pins. Figure 3.5 shows the relationship between theoretically predicted and experimentally

measured values of total current as a parabolic function of voltage. Analysis of the volt-ampere characteristics for different geometric configurations resulted in the following conclusions:

- i. The simulation results show the trend similar to the experimental data thus confirming that when the gap increases, the current decreases for a given voltage.
- ii. The onset voltage increases with an increase of the gap between electrodes.
- iii. The onset voltage decreases with an increase of the spacing between the pins in discharge electrodes.
- iv. The simulation results also correspond to the experimental results showing that, at the same voltage level, the total current of the 2×2 cm configuration is higher than that of the 1×1 cm configuration. This means that when the distance between electrodes increases, the total current would increase despite the reduction of the number of pins in discharge electrode.
- v. The difference between experimental and simulation results for (1×1) electrode system could be due to a higher density of discharge pins. This elevates the corona onset level, which can generate additional discharge spots, not considered in the computational model.

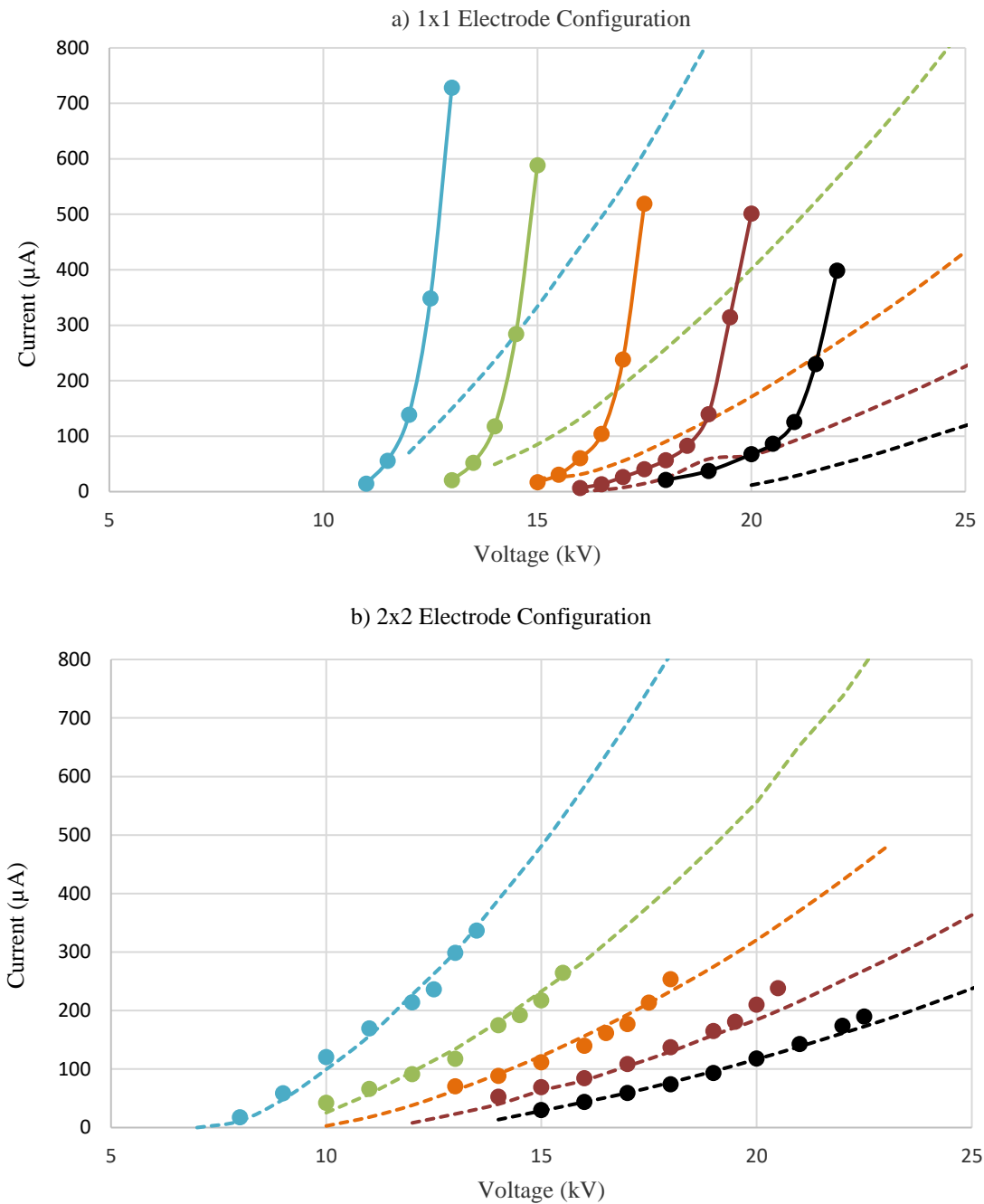


Figure 3.5 Volt-ampere characteristics in different electrode configurations (a) 1×1cm, (b) 2×2 cm. Experimental data (circles) are shown vs. simulation results (dotted lines). The gap is increasing from the left (20 mm) to the right (40 mm).

3.4.3 Voltage-Induced Total Air Mass Flow

In order to evaluate the mass transport, the air mass passing different cross sections close to the bottom plate was calculated. Equation (3.7) allows calculation of the air mass passing X-Y plane in one second

$$Q = \iint_A 0.5\rho \cdot |u_z| dA \quad (3.7)$$

To analyze the influence of voltage on airflow, one can compare the air mass flux Q , passing the channel cross-section plane 5 mm away from the material surface. For example, $z = -25$ mm plane was chosen for the 30 mm gap and $z = -35$ mm plane for the 40 mm gap.

Figure 3.6 shows the results of simulation, which demonstrate that the air mass flux is proportional to the voltage.

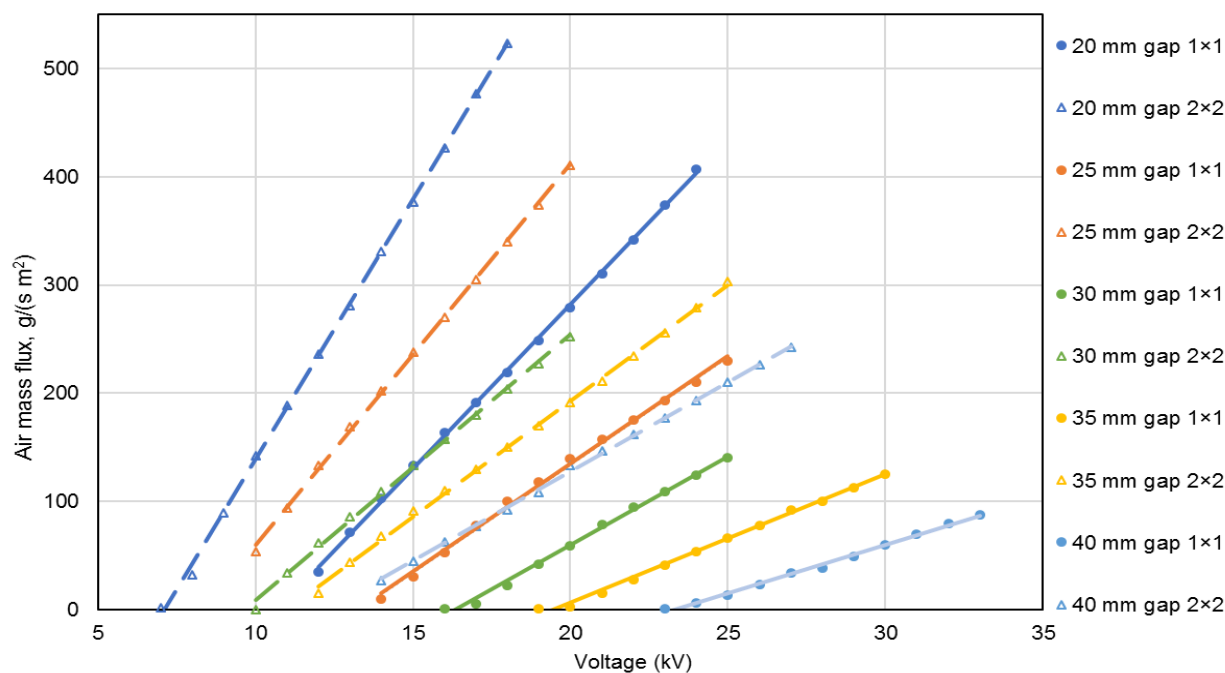


Figure 3.6 Air mass-voltage characteristics in different geometric configurations (simulation results).

Both the geometry of electrode and the gap significantly affected the slope of the voltage-air mass flux lines. According to Figure 3.6, larger gap reduced the slope, whereas larger pin spacing

increased the slope. The slope coefficients and onset voltages for different geometries are presented in Table 1.

Table 1: The slope coefficients of air mass transfer-voltage curves.

Configuration 1×1	20 mm gap	25 mm gap	30 mm gap	35 mm gap	40 mm gap
Slope, kV/cm	31.0	20.2	15.7	11.3	9.3
Onset voltage, kV	10	14	17	20	24
Configuration 2×2	20 mm gap	25 mm gap	30 mm gap	35 mm gap	40 mm gap
Slope, kV/cm	49.3	35.9	25.4	21.1	16.7
Onset voltage, kV	7	9	10	11	12.5

Larger slope means that the air mass flow increases steeper with the increased voltage. Hence, larger spacing between the electrodes and a small gap is preferred to provide higher drying rate.

3.4.4 Relationship Between Charge and Mass Transport

The air mass flux passing an unit area at the plane 5 mm above the material surface, deposited on the collecting electrode was compared with experimental dataset (Figure 3.7). It follows that both simulation and experimental results of air mass/water mass transport show parabolic relationship with current. Transformation of experimental dataset shows linear relationship between air mass transport and square root of electric current

$$u_z \propto \sqrt{I} \quad (3.8)$$

Considering that the air mass flux crossing unit area per second coincides with the drying rate, one can conclude that ionic wind is the major driving factor of mass transfer (Robinson, 1961). It is interesting to note that in the gap between electrodes had very limited influence on the drying rate at the same corona current.

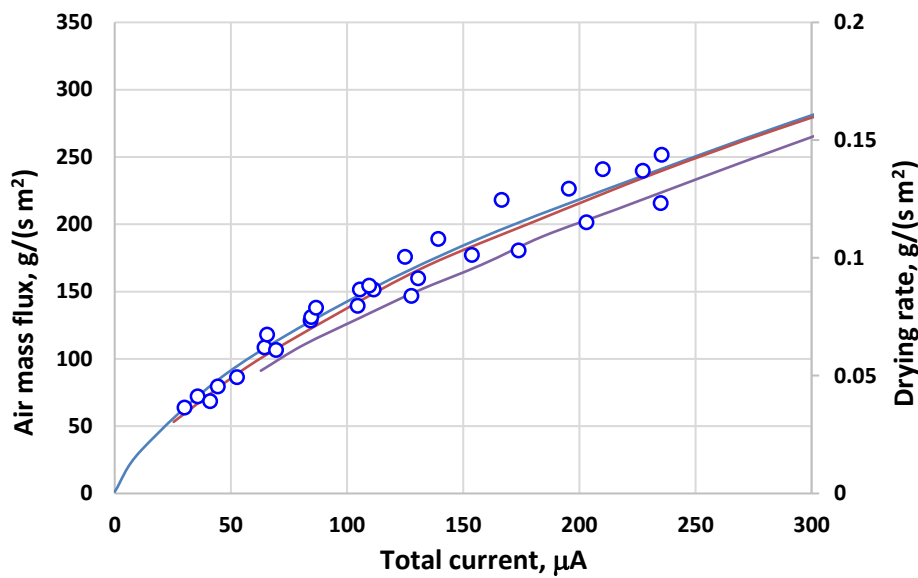


Figure 3.7 Current-induced air mass transport (lines, simulated for the gaps from 20 to 35 mm) and drying rate (circles, experimental data for the gaps from 20 to 40 mm) for 2×2 electrode.

3.4.5 Airflow Pattern for Different Geometric Configurations

Corona discharge produces non-uniform distribution of the electric body force: it has high value near the pin tip, but rapidly decreases at increasing distance. In this situation, the airflow pattern strongly depends on the flow channel geometry. The airflow pattern in an infinite channel (one pin in an open space) will have a shape of a large toroidal vortex occupying practically the entire air gap. For narrower channels, created by interactions with adjacent discharge electrodes, the air stream is not able to penetrate freely the entire air gap so its velocity near the solid collector electrode is reduced. The different investigated geometries resulted in quite distinct patterns of airflow in each computational cell. Four cases with different gap and electrode configurations were considered.

Case 1. (1×1 cm) electrode, 30 mm gap

In this case, the flow channel is narrow and the air gap is relatively short. The electric forces are sufficiently strong to push air molecules towards the grounded collector plate, even though the flow velocity is relatively small with the maximum values close to 0.5 m/s. Due to high flow resistance, only one flow vortex in the center of the channel was formed (Figure 3.8).

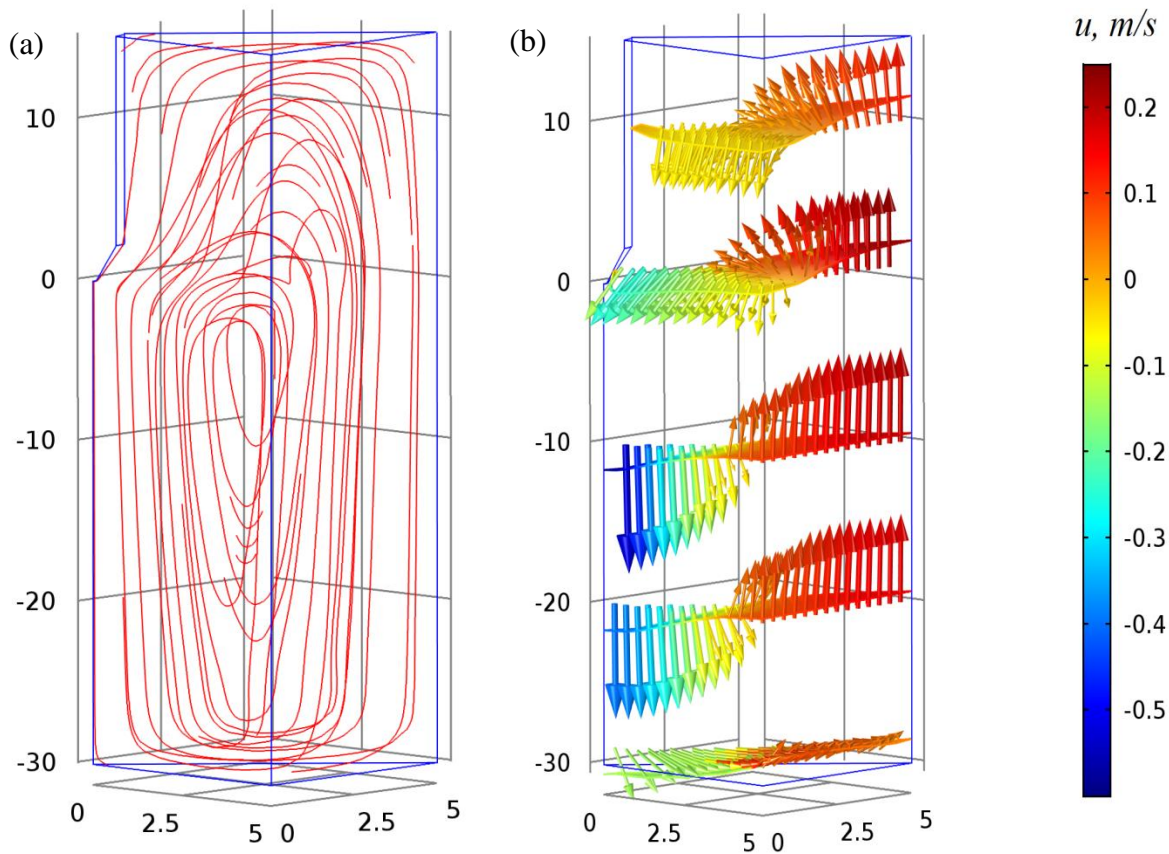


Figure 3.8 Airflow in the 30 mm gap and 1×1 electrode configurations at 20 kV: (a) streamlines of velocity field, (b) velocity field.

Case 2. (1×1 cm) electrode, 40 mm gap

The channel cross-section remains the same as in the previous case, but its length is increased. This significantly increases the flow resistance. The air steam is not able to penetrate the entire air gap, which results in very small air velocity near the grounded collector plate. Similarly, like in the previous case, only one vortex arises in the center of the channel (Figure 3.9).

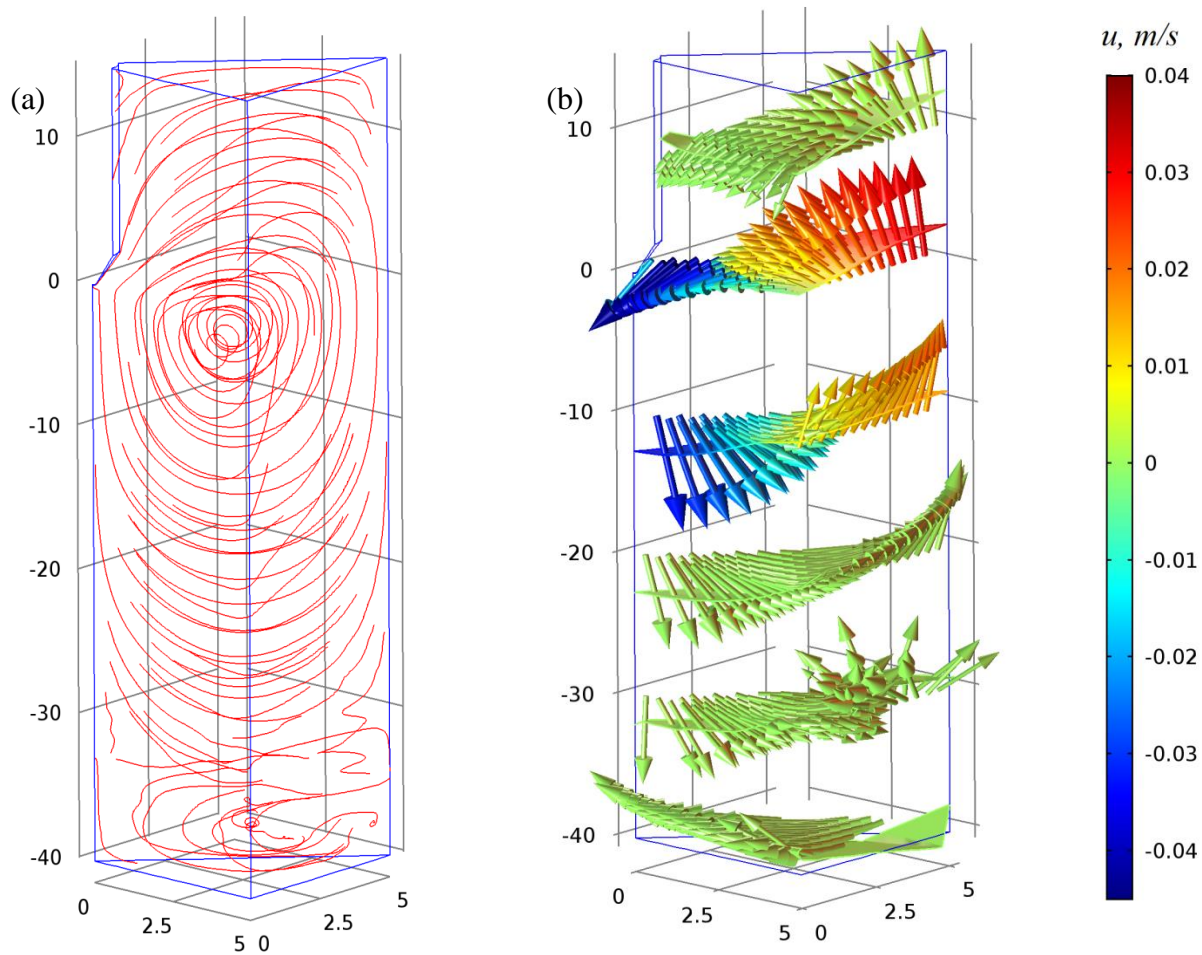


Figure 3.9 Airflow in the 40 mm gap and 1×1 electrode configurations at 20 kV: (a) streamlines of velocity field, (b) velocity field.

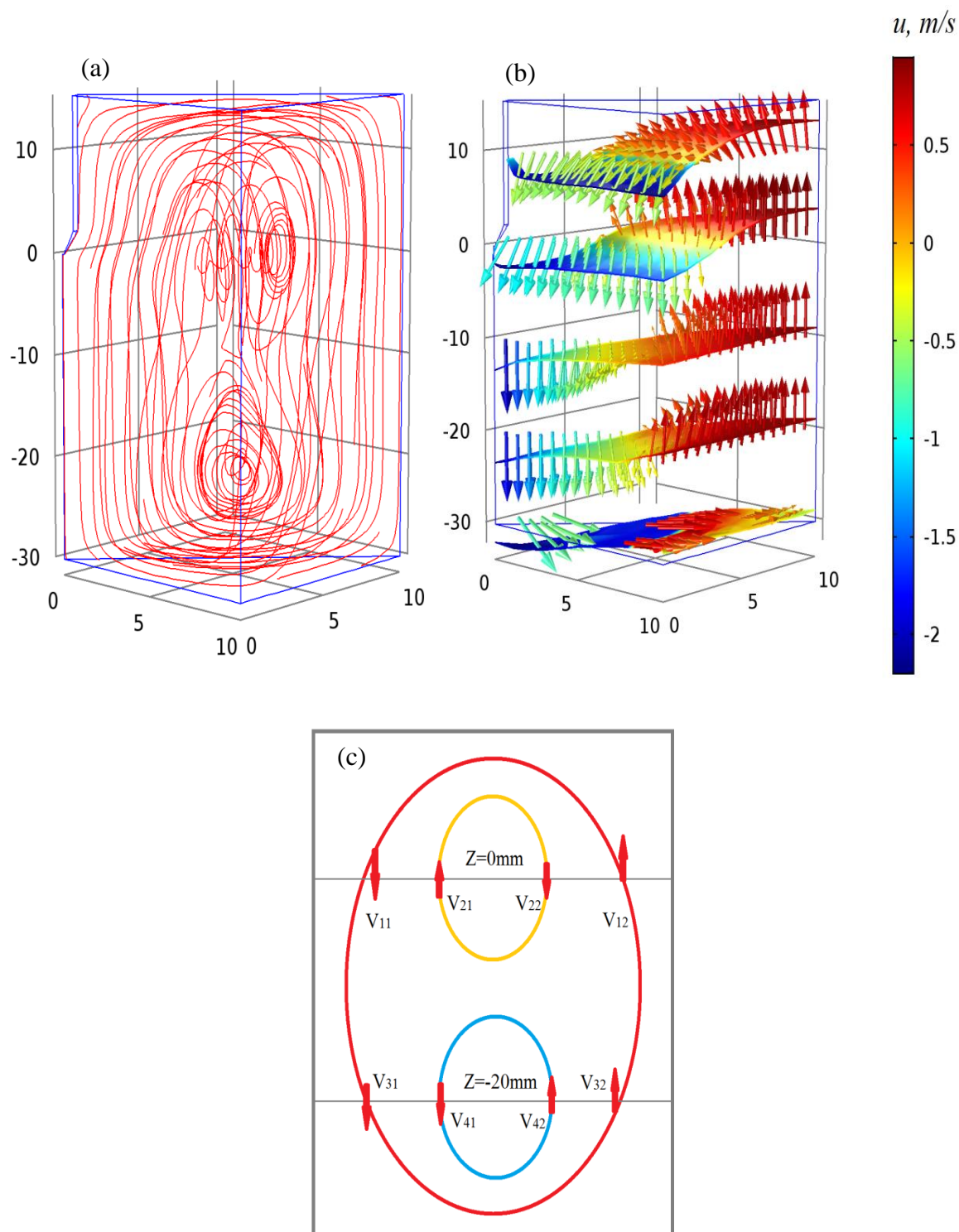


Figure 3.10 Airflow in the 30 mm gap and 2×2 electrode configurations at 20 kV: (a) streamlines of velocity field, (b) velocity field, (c) schematic representation of vortices structure.

Case 3. (2×2 cm) electrode, 30 mm gap.

Because the channel cross-section is four times larger in this case, the same electric body force produces much stronger flow. The maximum velocity close to the collector plate is around 2 m/s. Changed aerodynamic conditions resulted in a much more complicated volumetric flow structure. Three vortices appear in this case (Figure 3.10).

More schematic picture of vortices structure, presented in Figure 3.10c, shows one global vortex covering the entire air gap and two local vortices: one near the pin (marked in yellow) and another one close to grounded collector plate (marked as blue). Both local vortices are not coplanar. After careful examination, one can find a $60^\circ\sim 90^\circ$ angle between them.

Case 4. (2×2 cm) electrode, 40 mm gap

Even more complicated vortex structure can arise in the case of wider channels and larger air gap (Figure 3.11). The velocity magnitude decreases, but four vortices occur in this case due to the large gap and large distance between electrodes.

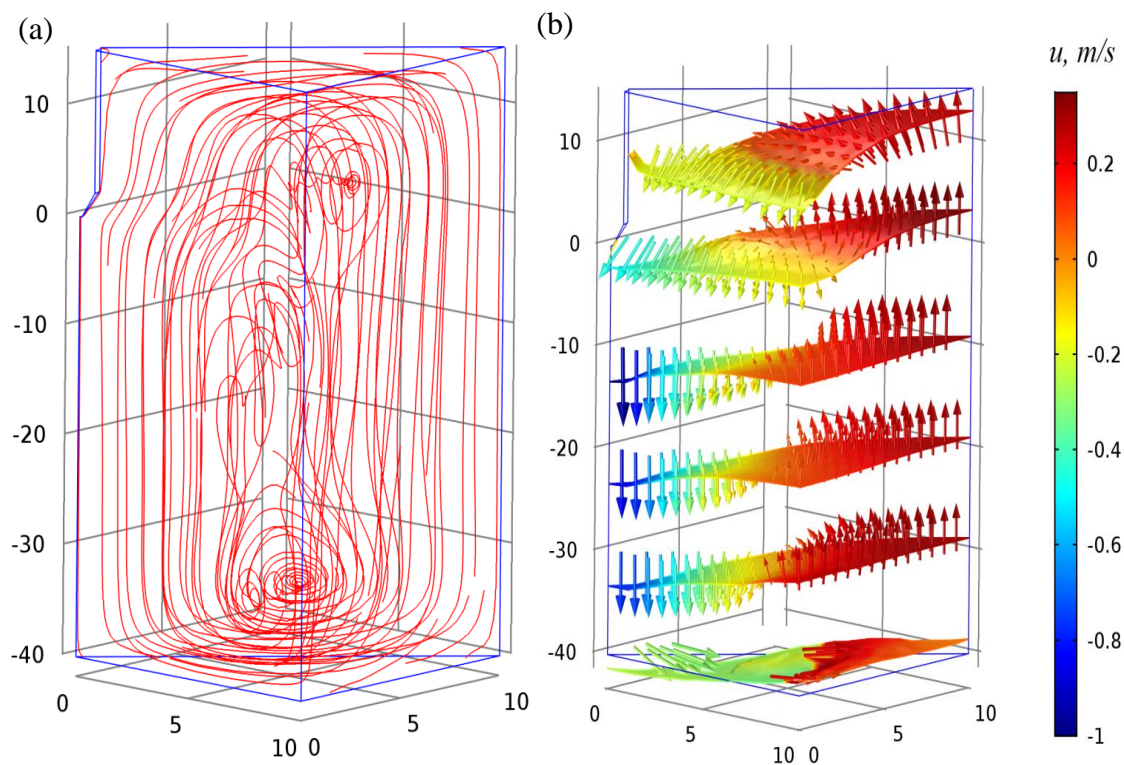


Figure 3.11 Airflow in the 40 mm gap and 2×2 electrode configurations at 20 kV: (a) streamlines of velocity field, (b) velocity field.

As one could see, the proposed numerical simulation approach is a powerful tool to visualize aerodynamic pattern and spatial distribution of velocity gradients in the drift region. All cases discussed previously in this section represent equilibrium conditions with established aerodynamic flow. Although this model did not take into account potential interference between neighboring channels, it gives an idea about the effect of geometry on the aerodynamic conditions in a single channel. This study predicts the occurrence of vortices in a multiple pin-plate electrohydrodynamic dryer. The refined model, which could consider interference effects, could be used for optimization of geometrical parameters of EHD dryers for industrial applications.

3.4.6 Total Air Mass Crossing Different Planes

Due to non-uniform distribution of velocity, the total air mass passing through the channel depends on the distance from discharge electrode. To analyze spatial distribution of total airflow in the channel, the air mass flux passing each X-Y cross-sectional area was calculated at different z-values with 1-mm increment. The 15-mm length of the pin was considered as positive z-value, whereas the gap length was considered as negative z-value. For example, when the gap length was 30 mm, the total model length is 45 mm; therefore 46 X-Y planes with 1-mm interval have been created to calculate the air mass crossing each plane. The air mass flow, calculated for each plane, is presented in Figure 3.12.

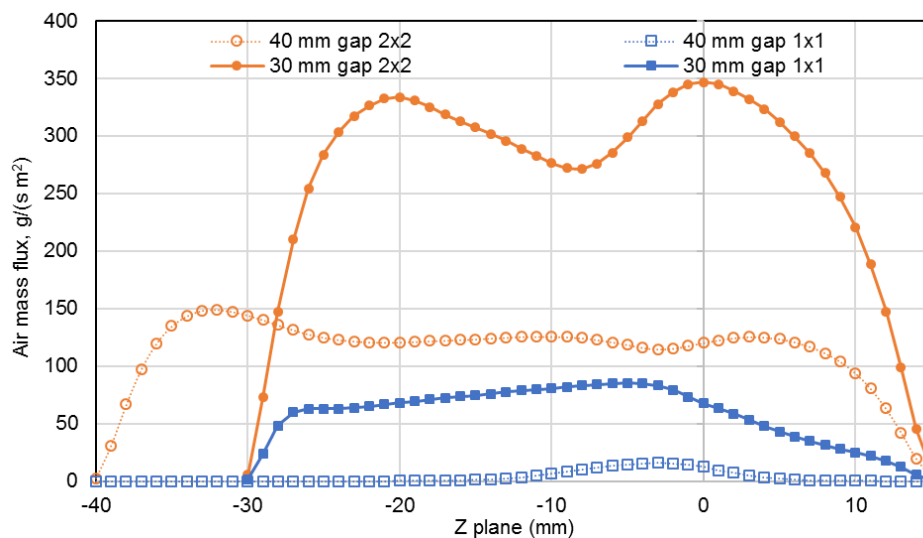


Figure 3.12 Air mass transport characteristics in different geometries and 20 kV voltage.

It follows that the maximal air mass flux was in case of (2×2) electrode and 30 mm gap, whereas minimal air mass flux was for (1×1) electrode and 40 mm gap. This knowledge is instrumental for understanding of airflow pattern in different locations, allowing practical design and optimization of air-assisted EHD dryers.

3.5 Conclusions

The corona discharge in the multiple pin-to-plate configuration was simulated numerically. It has been confirmed that the total corona current of multiple pin electrode is a parabolic function of voltage. The current decreased with an increase of the gap between the electrodes and increased with an increase of the spacing between the pins. Moreover, spacing between pins affected corona onset voltage. The geometric configuration of the discharge electrode had a significant influence on the aerodynamic conditions of charge and mass transport. Both simulated and experimental results show that total air mass flux is a parabolic function of total current and a linear function of voltage. Under the same voltage, the gap and geometry of multiple pin discharge electrode can be adjusted to allow a larger airflow, corresponding to higher drying rate.

Chapter 4

4 Numerical Study of the Characteristics of a Dielectric Barrier Discharge Plasma Actuator

4.1 Introduction

A dielectric barrier discharge (DBD) generated near a surface of an object in gases is accompanied by the electrohydrodynamic (EHD) gas flow. Ionic species drifting in the electric field collide with neutral molecules, which results in an ionic wind. This can be applied to design a plasma actuator to allow an increase or decrease of the flow boundary layer and modify the dynamic characteristics in that region.

This thesis investigates a DBD plasma actuator using a numerical model. In order to avoid large computing times, streamers, Trichel pulses and the ionic reactions involving photons and electrons are neglected. This numerical model assumes two types of generic ions, one positive and one negative, whose drift in the electric field produces the electrohydrodynamic flow. The simulation results provide insights into the physical mechanisms of DBD that include the electric field, space charge transport, surface charge accumulation and air flow.

This Chapter presents the V-I characteristics, distribution of charges, velocity profiles and estimated drag force. The effects of the voltage level, frequency and inlet air velocity on the actuator performance are also discussed and interpreted. It is expected, that these parametric studies will be beneficial for the optimization of DBD plasma actuator design.

In this chapter, only the simulation results are presented. Similar observations in the experiment can be found in the referred papers. In the comparison between the simulation results and experimental data, a close agreement was observed, which verifies the correctness of the proposed algorithm.

4.2 Methodology

4.2.1 Model of the Problem

The DBD actuator consists of two strip electrodes, one exposed and one buried in a dielectric plate. The high voltage exposed electrode is a 0.08-mm thick copper strip located at some distance downstream from the leading edge of the dielectric wall. The grounded electrode is a 0.2-mm thick strip placed 2 mm below and 4 mm downstream of the exposed electrode. The dielectric plate is made of PMMA having relative permittivity of 4.5. Its thickness is 5 mm and it is so long that the air molecule's collision effect on its leading edge would disappear before reaching to the discharge region. Numerical simulation is done for a 200 mm long section of the plate.

The discharge is generated by applying a sinusoidal voltage to the exposed electrode with

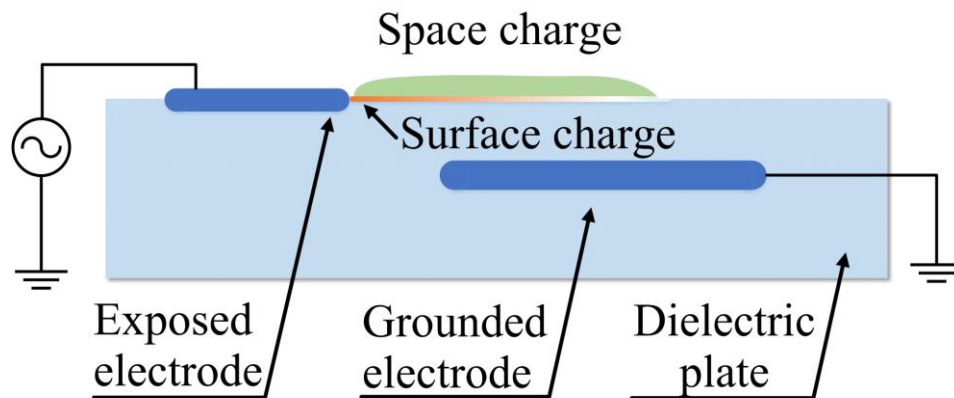


Figure 4.1 Unscaled sketch of a DBD actuator

amplitude ranging from 14 to 22 kV and frequency of 0.5, 1 and 2 kHz. The computational model completely ignores the ionization layer and assumes that positive or negative ions are injected from the discharge electrode surface. The drift dynamics of both ions is included, so that the surface charge accumulation can be correctly evaluated, but the dynamics of the ionic reactions, leading to the pulse formation, is neglected. This way, a longer time step can be used and the simulations converge much faster. Moreover, the surface charge accumulation actually plays a controlling role for limiting DBD in the corona regime instead of transitioning to the streamer regime.

The discharge produces large amounts of negative or positive ions and their movement in the electric field creates an ionic wind with the velocity of about 8 m/s [13]. Since we are only

interested in a quasi-stationary pattern of fluid flow, without much concern of small eddies changing over time, laminar flow is adopted in the numerical model. In addition, the presence of external airflow may affect the convection of ions and, therefore, increase the discharge current intensity, but this effect is ignored in our model.

The ionic wind significantly reduces the drag force on the dielectric plate. However, the drag force reduction not only depends on the discharge strength, but also on the air stream flowing over the plate. Thus, in order to closely examine the drag reduction, the proposed model was used to simulate different external airflow velocities: 0, 1, 3, 6, 9 and 12m/s. Although it only takes a few voltage cycles for the electric field to reach a quasi-stationary state, it was found that it is necessary to run the model for at least 30 cycles to allow the fluid flow reach a steady state.

In summary, the numerical model involves mutual interaction between the electric field, space charge distribution, surface charge accumulation and air flow. In order to simplify the model and reduce calculation time, a few assumptions were accepted as follows:

- The discharge is generated in the glow regime;
- The ionization layer can be replaced by the direct injection of ions from the area very near the active electrode;
- The ionic reactions and secondary electron emissions in the glow regime that lead to the pulse formation can be neglected;
- The DBD actuator operates in air at atmospheric pressure and room temperature.
- The ambient air is incompressible and its flow can be assumed to be laminar;
- Charge convection due to airflow is negligible;
- Varying humidity and elevated temperature do not affect the discharge or airflows.

4.2.2 Governing Equations

1) *Electric field*

The electric field is governed by the well-known Poisson equation:

$$\nabla^2 \Phi = -\frac{q}{\epsilon} \quad (4.1)$$

where Φ is the scalar electric potential, q is the space charge density and ϵ is the permittivity of the ambient gas.

In our model, since the ionization layer is neglected, and both positive and negative ions are injected from the area near the discharge electrode surface corresponding to the positive and negative phase of voltage, the major challenge is to determine the amount of injected charges at different times in the cycle. Therefore, we adopted the so-called Kaptzov's hypothesis, that above the onset level the electric field on the discharge region of the electrode remains constant. This constant value of electric field intensity in the air can be calculated using Peek's formula [118]:

$$E_0 = 3.1 \times 10^6 \cdot \left(1 + \frac{0.308}{\sqrt{R}}\right) \left[\frac{V}{cm}\right] \quad (4.2)$$

where R is the radius of discharge electrode in cm. In the studied case, Peek's value is equal to 182 kV/cm.

The ionic charges must satisfy the charge transport equation:

$$\frac{\partial \rho_c}{\partial t} + \nabla(\rho_c \mu_c \mathbf{E} - D \nabla \rho_c) = 0 \quad (4.3)$$

where ρ_c is the ionic space charge density, \mathbf{E} is the electric field intensity vector, μ_c is the ion mobility, and D stands for the ion diffusion coefficient. The constant μ_c can be determined experimentally, and in this case it is assumed to be equal to $1.5 \times 10^{-4} \text{ m}^2/(\text{V} \cdot \text{s})$. In reality, diffusion coefficient is $2.8 \times 10^{-6} \text{ m}^2/\text{s}$ for the positive ion and $4.3 \times 10^{-6} \text{ m}^2/\text{s}$ for the negative ion. However, these values are so small that would cause numerical divergence. An artificial diffusion coefficient is commonly added to prevent numerical instability. Thus, D is set as $1 \times 10^{-3} \text{ m}^2/\text{s}$ for both positive and negative ions.

A part of the space charge will eventually leave the computational domain, and the rest will be deposited on the dielectric surface. At the interface between the air and dielectric, the continuity equation must be satisfied:

$$\vec{n} \cdot (\mathbf{D}_d - \mathbf{D}_a) = \rho_s \quad (4.4)$$

where \vec{n} is the normal vector, ρ_s the surface charge density, \mathbf{D}_d and \mathbf{D}_a is the electrical displacement vector in dielectric and air, respectively.

The surface charge is created by the deposition of space charge on the dielectric surface and its rate of change can be calculated as:

$$\frac{\partial \rho_s}{\partial t} = \vec{n} \cdot \vec{J} = \mu_c E_{\perp} \rho_{\perp} \quad (4.5)$$

In the above equation, \mathbf{J} is the drift current density towards the dielectric surface, μ_c is the ion mobility, E_{\perp} is the electric field normal to the surface, ρ_{\perp} is the space charge density above the surface.

Equations (4.1)-(4.5) are mutually coupled. All of them need to be solved simultaneously until a convergence is reached. At the end, the distribution of electric field, space charge and surface charge can be obtained and all are affected by each other.

If the electric field produced by charges is ignored, the Poisson equation (4.1) can be replaced by the Laplace equation:

$$\nabla^2 \Phi = 0 \quad (4.6)$$

The electric field calculated from the Laplace equation can be used as a reference to compare with that from the Poisson equation, in order to reveal the effects of ions on the electric field.

2) Air flow

An external air stream flows into the simulated domain from the left boundary, retarded by the no-slip dielectric surface and accelerated by the discharge, and then flows out from the right boundary. A laminar flow model is assumed to study the flow pattern. It needs to satisfy the continuity equation:

$$\nabla \cdot \mathbf{v} = 0 \quad (4.7)$$

as well as the Navier-Stokes equation [119]:

$$\rho(\mathbf{v} \cdot \nabla)\mathbf{v} = -\nabla P \boldsymbol{\gamma} + \nabla \boldsymbol{\tau} + \mathbf{F} \quad (4.8)$$

where \mathbf{v} denotes the air velocity vector, ρ is the air density, P is the pressure, $\boldsymbol{\gamma}$ is the unit tensor, and $\mathbf{F} = q\mathbf{E}$ stands for the external body force. $\boldsymbol{\tau}$ as the stress tensor can be calculated as

$$\boldsymbol{\tau} = \mu(\nabla \mathbf{v} + \nabla \mathbf{v}^T) \quad (4.9)$$

where μ is the air viscosity.

Equations (4.7)-(4.9) are solved using the electric field calculated from (4.1)-(4.5). They are not fully coupled as the charge convection due to gas flow is neglected. This means that the airflow is produced by the electric field, but it doesn't affect the electric field and distribution of space charge.

In this study, all equations were solved by using the COMSOL (Comsol Inc, MA, USA) commercial software based on the Finite Element Method (FEM). This technique offers great flexibility in discretization of the computational domain. It is capable of dealing with complex geometries and the multi-physical processes involved in DBD.

4.3 Electrical results

4.3.1 Electric Field Intensity

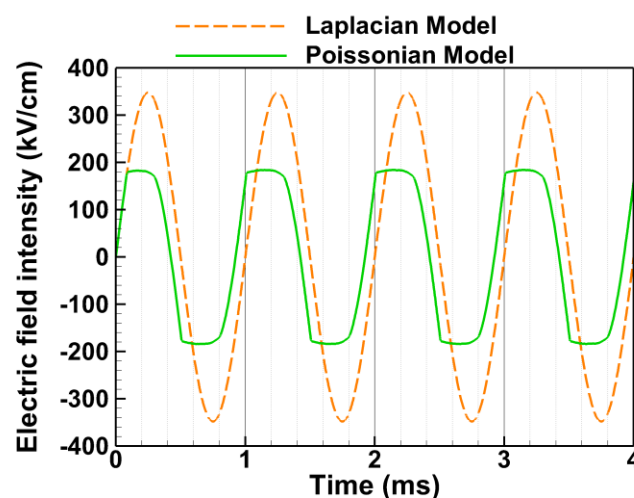


Figure 4.2 Electric field intensity on the electrode tip in the Laplacian and Poissonian models

Figure 4.2 shows the electric field intensity at the tip of the discharge electrode calculated from the Laplace and Poisson equations for 20 kV and 1 kHz. The Laplacian model does not consider the space charge or the surface charge accumulated on the dielectric surface, whereas the Poissonian model takes these factors into consideration. In the Poissonian model, the electric field intensity on the electrode tip remains constant when it reaches Peek's value, which is 182.0 kV/cm in this case. It proves the successful adoption of the Kaptzov's hypothesis in the model.

It can be seen that there is a phase difference between the electric fields in both models. This can be explained by the capacitive effect due to the ions accumulated around the electrode tip, both in space and on the dielectric surface.

4.3.2 Electric Current

The total discharge current in the DBD consists of two parts: drift current and displacement current. However, only the drift current due to the movement of charges in the electric field is considered here and the displacement current has been neglected. This is commonly reported in experiments [68, 69] where they present only the electric drift current, because the displacement current does not contribute to the power consumption or electro-mechanical conversion.

The drift current can be calculated using Sato's formula [120]:

$$I = \frac{w}{V_{ap}} \iint \rho_c \mu_c (E_x E_{x0} + E_y E_{y0}) ds \quad (4.10)$$

where w is the width of the system, V_{ap} is the electric potential applied on the electrode, ρ_c is the space charge density, μ_c is the ion mobility, E_{x0}, E_{y0} stand for the x and y components of the Laplacian electric field intensity, E_x, E_y represent the x and y components of the Poissonian electric field intensity, and ds refers to the integration over the whole calculation domain. 2D model includes the x and y axis only and w is an unknown value. Therefore, all global parameters should be treated as per unit length.

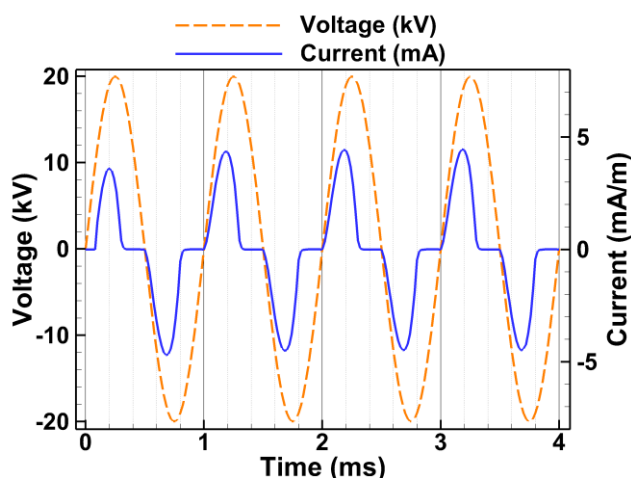


Figure 4.3 Electric current and voltage applied on the electrode as a function of time

Figure 4.3 shows the drift current waveform for the case of 20 kV and 1 kHz. The maximum current increases in the first two cycles and eventually reaches 4.8 mA in the following cycles. It confirms that the electric field needs at least three voltage cycles to reach a quasi-steady state. Since the discharge pulses are ignored, the current curve is very smooth, and virtually the same in the positive and negative half-cycles. We can also notice a phase difference between the voltage and current due to the distortion of electric field caused by the buildup of the released ions.

4.3.3 Effects of Voltage Level and Frequency

In order to investigate the effects of voltage level and frequency on the current, the discharge was simulated for sinusoidal voltages with amplitude from 18 to 22 kV and frequency of 0.5, 1 and 2 kHz. Since the current varies over the voltage cycle, the maximum value of current in different cases was compared (Figure 4.4).

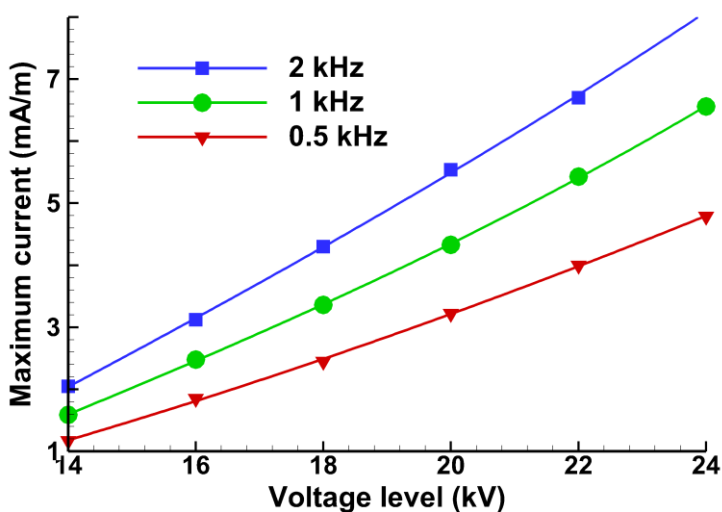


Figure 4.4 Maximum current versus voltage level and frequency.

Two trends can be observed regarding the characteristics of voltage level and frequency in DBD. On the one hand, current increases with a higher voltage level. This can be easily understood since a higher voltage would generate a more intense discharge resulting in a higher current. The graph indicates a parabolic relationship between the maximum current and the applied voltage amplitude. However, over some range of voltages this relationship can be considered as a linear one.

On the other hand, for a fixed voltage the maximum value of current increases as the frequency increases. This tendency matches the experimental results reported in [11, 13]. It can be explained

by the fact that at the higher frequencies, ions have less time to leave the region close to the discharge electrode, and, therefore, they create a stronger local electric field, which induces more opposite ions when the voltage changes polarity.

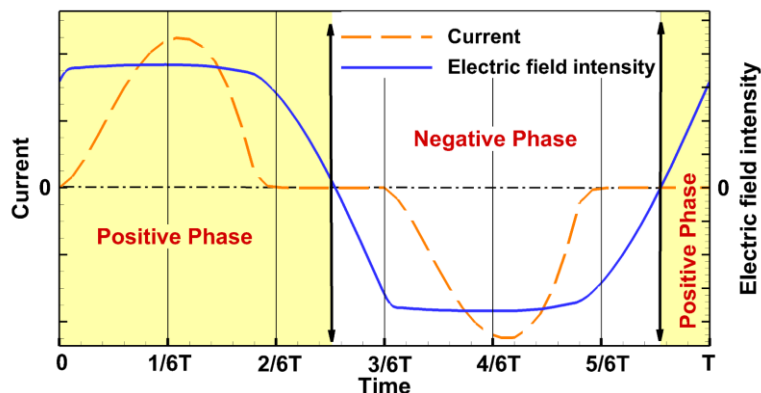


Figure 4.5 Definition of different phases in the electric field intensity and current on the tip of electrode in one voltage cycle.

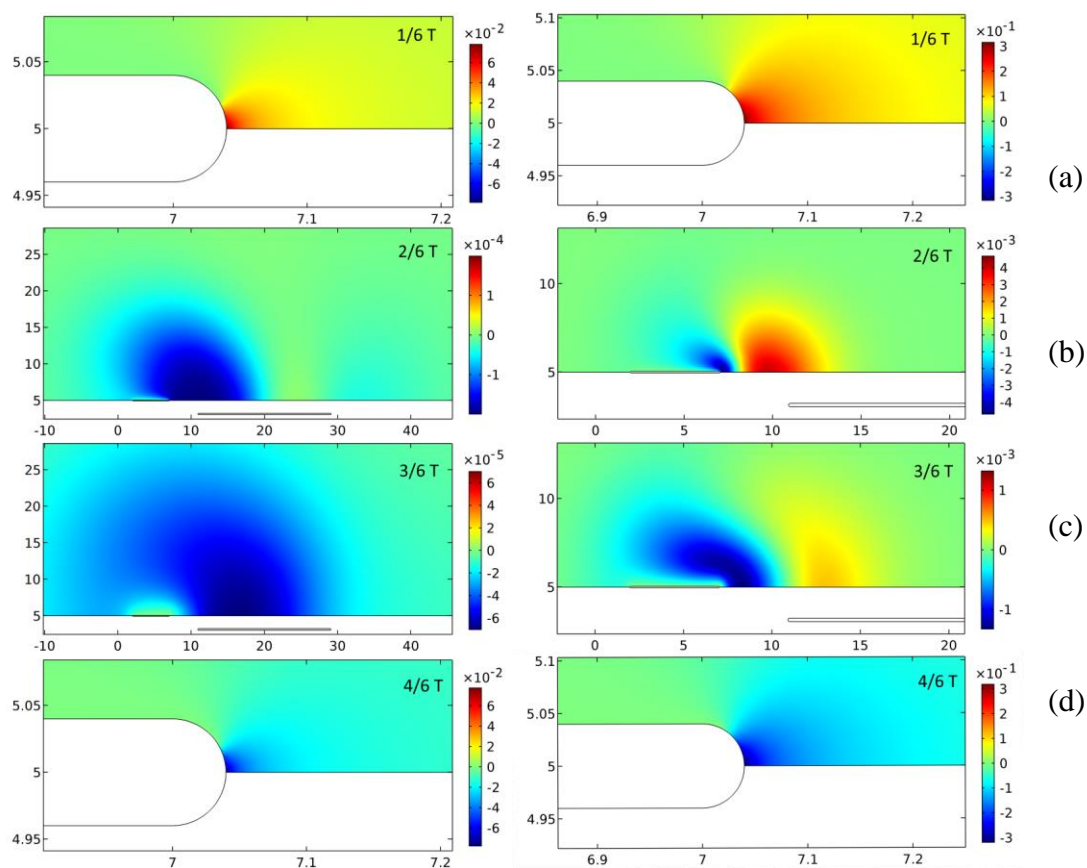


Figure 4.6 Distribution of space charge density [C/m^2] for $f=200$ Hz (left) and $f = 10$ kHz (right) with supplied voltage of 20 kV at the time of a) $1/6T$, b) $2/6T$, c) $3/6T$ and d) $4/6T$

4.3.4 Space Charge Density

Generally speaking, there are two ion transport mechanisms: diffusion and migration in the electric field. The latter dominates and produces the observed periodicity in the distribution of space charge density. Considering the symmetry of the discharge in positive and negative voltage cycles (Figure 4.5), it is sufficient to examine space charge density of one voltage half-cycle.

Figure 4.6 presents the distribution of space charge density from $1/6T$ to $4/6T$ for two cases with different frequencies. In order to have a better view, the geometric scale is purposely chosen at different instants of time and the color legend is symmetrized based on the highest value.

At $t=1/6T$ and $4/6T$, the graphs show an intense discharge around the exposed electrode. A large amount of ions is released from the area near the surface of electrode into space. It is obvious that the discharge strength increases with the frequency, by comparing the highest value of space charge density and discharge area for 200 Hz and 10 kHz (Figure 4.6a). In addition, the electric field intensity on the electrode tip remains same during discharge according to Kaptzov's hypothesis (Figure 4.5). At $t=2/6T$ and $3/6T$, a smaller scale is used to observe the overall transport of ions.

When $t=2/6T$, the positive-phase discharge stops and the discharge current is equal to zero (Figure 4.5). The positive value of electric field intensity means that it repels positive ions into space and attracts negative ions towards the electrode. In the case of a low frequency, positive ions migrated in electric field have enough time to move away from the electrode and then dilute into the space. However, if the frequency is higher, such as 10 kHz, positive ions have less time to move away and will still be around the electrode at $t=2/6T$ (Figure 4.6b). Those positive ions induce more negative ions to be released from the electrode surface in the negative discharge phase, and this explains why the current is higher in a case of a higher frequency.

Particularly, it may look strange that at $2/6T$ there is an obvious accumulation of negative charges near the discharge electrode, while the electric field is still positive. These negative charges are attracted to the electrode. If the recombination of positive and negative ions was taken into consideration in the numerical model, this phenomenon would be less visible because some negative ions will disappear. However, the ion recombination has minor effects on the discharge.

In addition, ion density at $2/6T$ is at least two orders of magnitude smaller than that at the discharge maximum, so that the recombination with opposite polarity ions is negligible.

At the time of $3/6T$, the negative phase of voltage does not start yet, but the electric field intensity is already negative, which means that negative ions are generated and repelled away from the electrode. This is the reason why the cloud of negative ions is distorted (Figure 4.6c).

As discussed above, the frequency has a significant influence on the dynamics of space charge transport. The dispersion and accumulation of space charges changes the electric field around the discharge electrode, and under Kaptzov's hypothesis, the electric field on the electrode tip dominates the discharge current. This gives us a deeper understanding of the relationship between frequency and current which can be verified in experiments [73].

Since in this model all ionic charges are assumed to be injected from the area very near the electrode surface, it is worthwhile to have a close look at that area. Figure 4.7 shows the electric field intensity and space charge density along the arc of electrode tip for different applied voltages. Since the discharge strength changes over time in one voltage cycle, only the results of the most intensive discharge in the positive phase are presented. For the electrode tip radius of curvature $R=0.04$ mm, the arc length of the electrode tip is 0.0628 mm, as shown as the x-axis below. The discharge is confined in the "discharge area" where space charge density is not equal to zero (Figure 4.7). The size of this area increases with the voltage. In addition, a higher voltage also results in a larger value of space charge density on the electrode tip.

Figure 4.7 shows that the electric field intensity decreases progressively with the distance from the electrode tip. It is also noticeable that the average electric field intensity in the region of discharge area is close to the Peek's value (182 kV/cm in this model). Theoretically, Kaptzov's hypothesis requires that the electric field intensity at each point in the discharge area should be equal to the Peek's value. However, given the complexity of the geometry and physical processes of DBD, it is almost unachievable in the numerical model.

Figure 4.8 shows the time evolution of total space charge in the calculation domain. In each half-cycle, ions are injected from the surface of discharge electrode. Some of them will be deposited on the dielectric surface and recombined with charges of different polarity, whereas, the rest

eventually leave the computational domain. As a result, the total value of space charge reaches a quasi-stationary state. Figure 4.8 also shows the symmetric properties between positive and negative phase. The symmetry might be broken in real situations considering the difference between the streamer discharge in positive phase and Trichel pulses in negative phase.

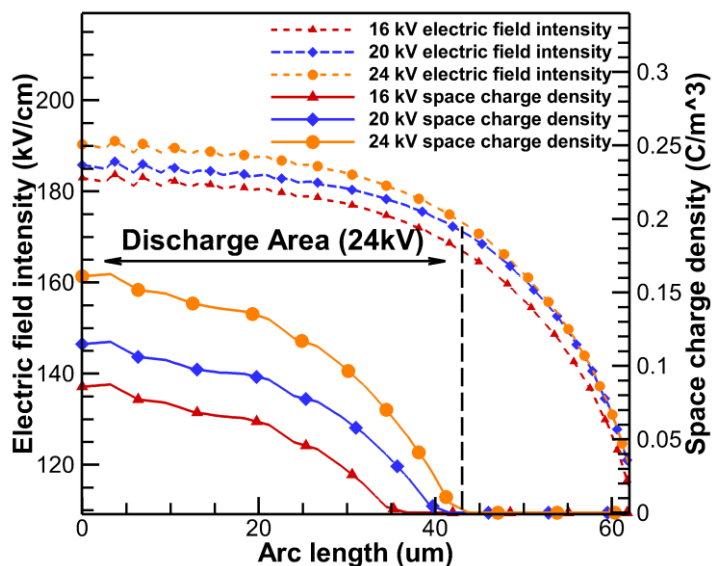


Figure 4.7 Electric field intensity and space charge density along the arc of electrode tip at the time of most intensive discharge for $V=16$ kV, 20 kV and 24 kV.

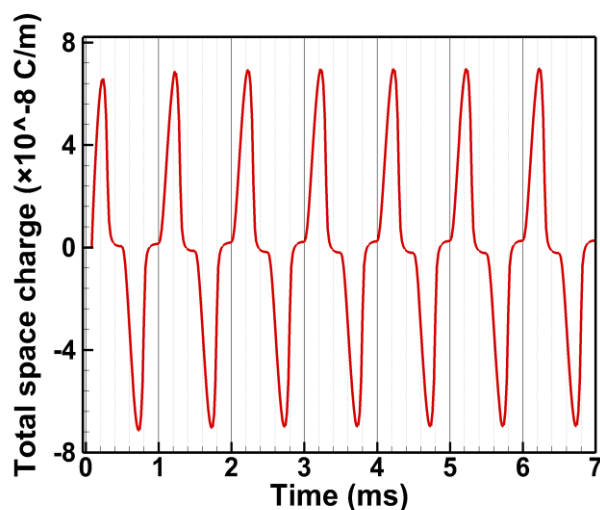


Figure 4.8 The evolution of total space charge in the calculation domain for the case of 20 kV, 1 kHz.

4.3.5 Surface Charge Density

The most fundamental phenomenon in DBD is the accumulation of surface charge on the dielectric plate. A time-dependent plot is particularly suitable for the analysis of the surface charge density due to its clear and intuitive presentation (Figure 4.9). In this graph, the horizontal axis is the arc length of the dielectric boundary (only the part close to the electrode is shown), the vertical axis shows different time steps, and the color represents the surface charge density. It can be observed that the polarity of surface charge reverses every half-cycle of voltage and that the highest surface charge density appears at the location about 4 mm away from the discharge electrode. In addition, the patterns of surface charge density incline towards the upper-right corner of the graph showing that it takes some time for space charges to move away from the discharge electrode and eventually be deposited on the dielectric surface. The space charge deposits faster near the discharge electrode and needs more time to travel to farther locations.

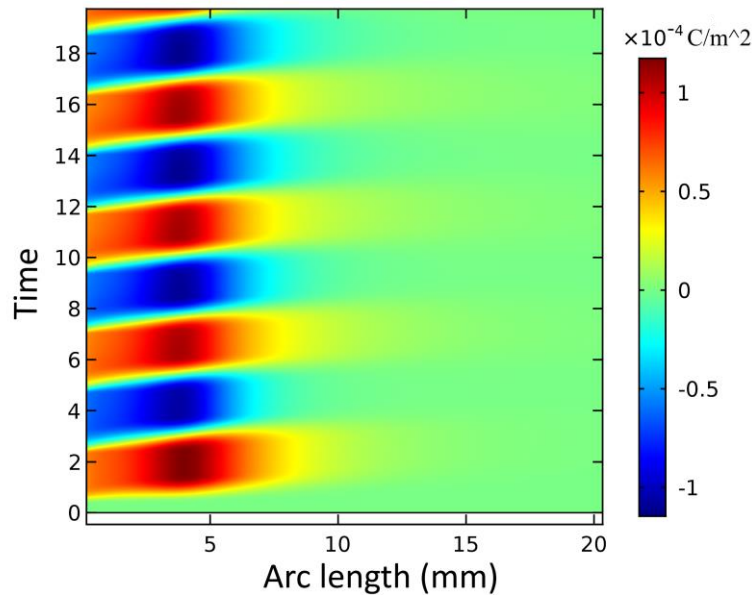


Figure 4.9 Time-dependent plot of charge density accumulated on dielectric wall.

4.3.6 Power Consumption

The electrical power consumed by the DBD actuator can be calculated from

$$P_e = V_{ap} \times I = w \iint \rho_c \mu_c (E_x E_{x0} + E_y E_{y0}) ds \quad (4.11)$$

where I comes from the Sato's formula (10). As explained by Pons [121], the electric power versus voltage in experiment obeys the following equation:

$$P_e = K \times f_{AC} \times (V - V_0)^n, \quad n = 2 \quad (4.12)$$

where K is a geometry-dependent constant, f_{AC} is the frequency of the applied voltage, and V_0 is the onset voltage. Several other authors, such as Roth et al. [75] and Enloe et al. [122, 123], use a different fitting function

$$P_e \propto V^n, \quad 2 < n < 3.5 \quad (4.13)$$

Note that current is a linear/parabolic function of the voltage (Figure 4.4). Therefore, it is reasonable that electric power consumption is a parabolic/cubic function of the voltage. Figure 4.10 presents the simulated results of average electric power consumption versus the voltage level for different frequencies. The data can be fitted very well either in a parabolic or a cubic function.

In addition, the linear relationship between power consumption and frequency, as observed in experiments, indicates that the current increases with the frequency. It has been confirmed in our previous discussion.

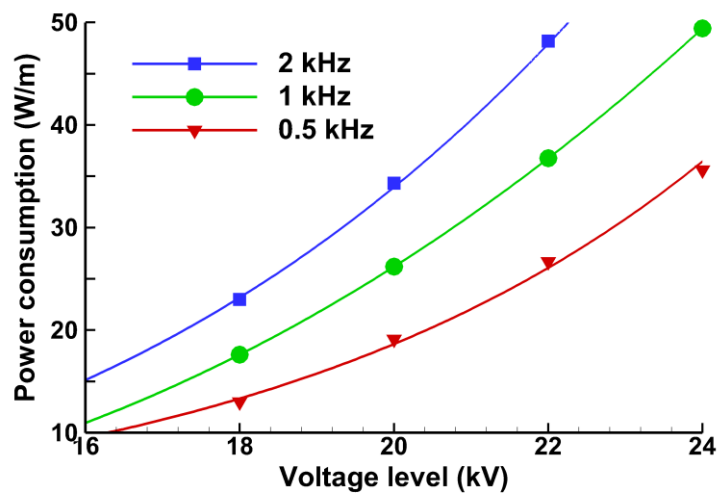


Figure 4.10 Electrical power consumption versus voltage for different frequencies.

4.4 Fluid Flow Results

4.4.1 Evolution of Velocity Field

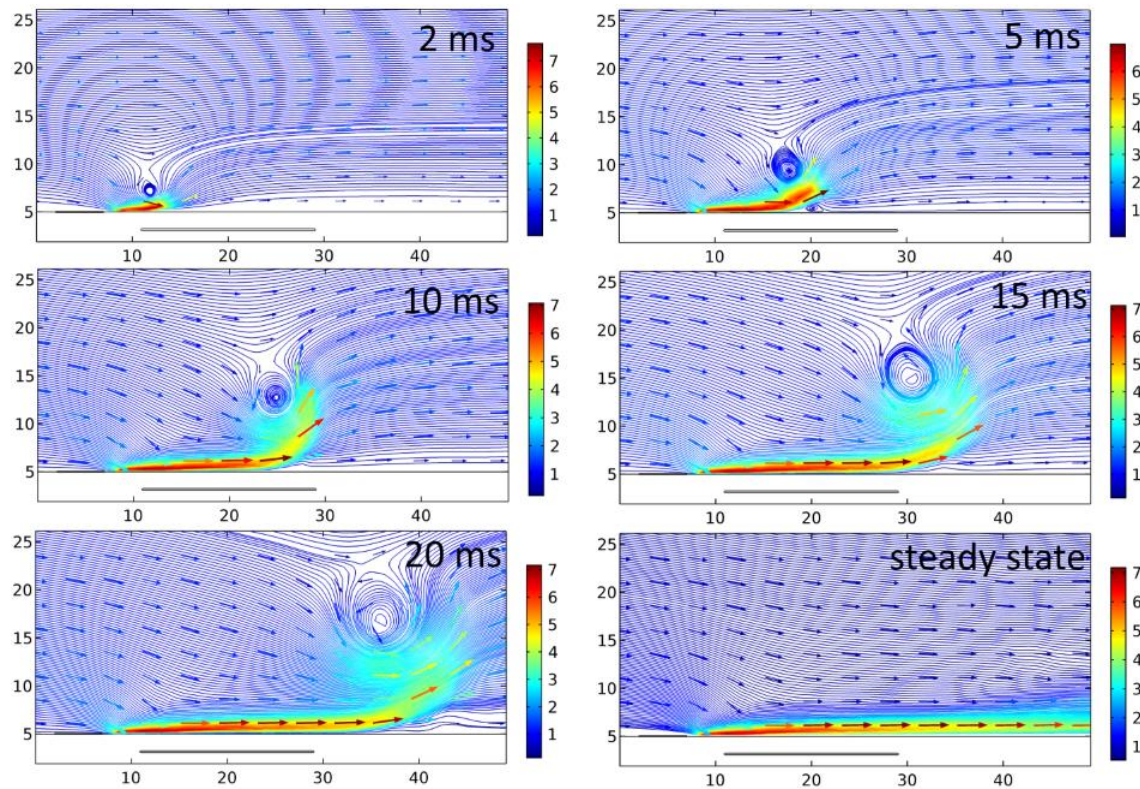


Figure 4.11 Evolution of velocity field at 2 ms, 5 ms, 10 ms, 15 ms, 20 ms and a steady state.

External velocity equal to 1 m/s.

According to the experiment presented in [69], the EHD wind generated by a plasma actuator reaches a steady state after 30 ms. This time can be roughly calculated by dividing the length of plasma region with the average velocity of air flow. In the presented calculations, the model for the voltage of 20 kV and the frequency of 1 kHz was run for 50 ms. It allowed the airflow to evolve to a quasi-steady state, where no significant difference exists between two consecutive cycles.

Figure 4.11 shows the evolution of velocity field at different time instants until it reaches a steady-state. The initial generation of EHD wind is accompanied by a vortex around the discharge electrode. As the EHD wind develops, the vortex moves away from the electrode and eventually disappears in the steady-state. The formation of the vortex can be explained by the fact that some air molecules accelerated by the discharge collide with other air molecules ahead of them, and they are bumped back. The vortex region also corresponds to a high negative pressure area that pulls

air molecules [124]. It can be predicted that the vortex, if it is properly generated, can be utilized to mix neutral molecules and ions, and then enhance the performance of an electrostatic mixer/separator.

4.4.2 Effect of DBD

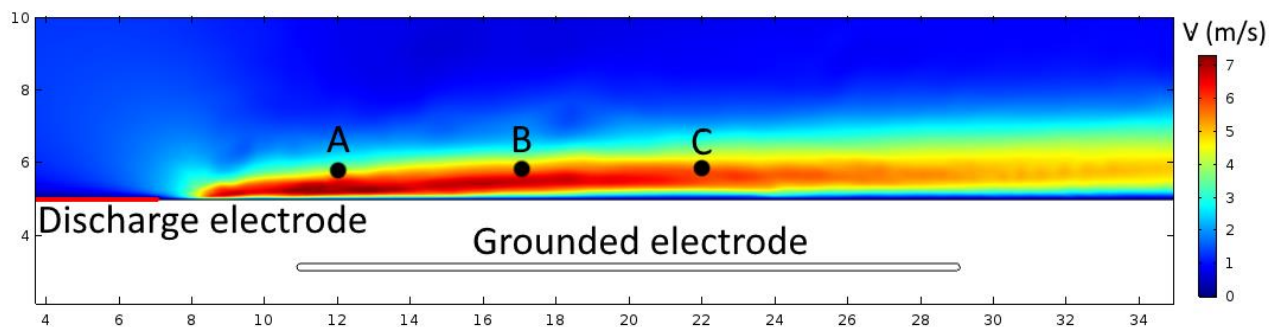


Figure 4.12 Velocity field in the wall boundary layer produced by DBD at 50 ms. External velocity equal to 1 m/s.

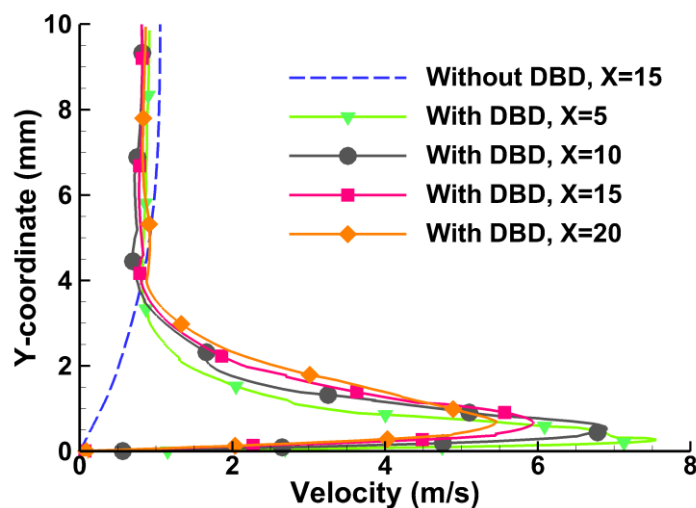


Figure 4.13 Velocity profiles along the lines perpendicular to the dielectric wall and downstream the discharge electrode.

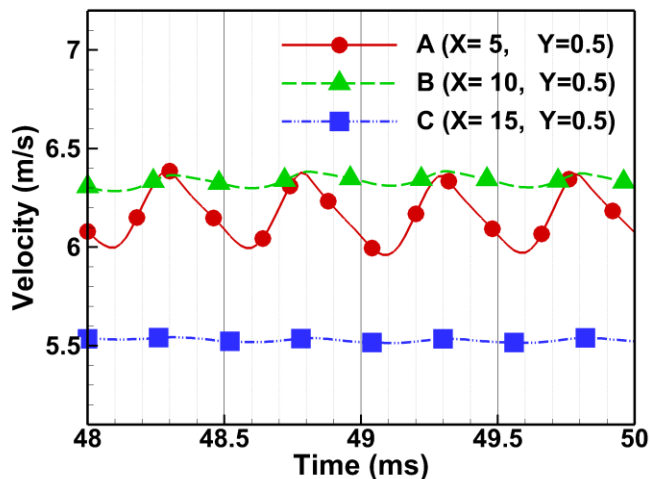


Figure 4.14 Time variation of the velocity at different positions.

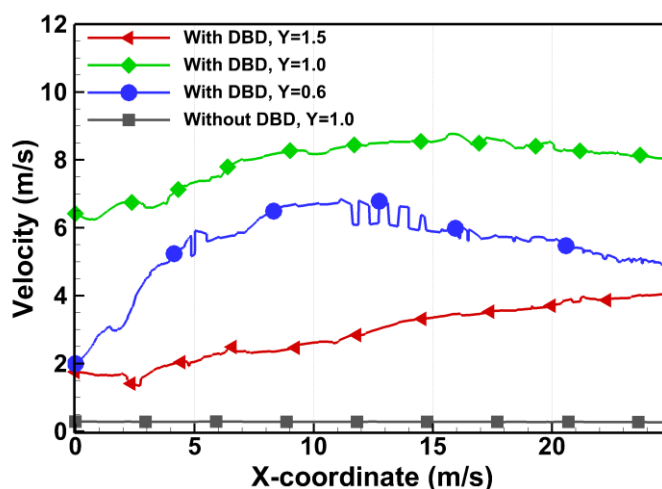


Figure 4.15 Velocity profiles along the lines parallel to the dielectric wall.

The velocity profile in the boundary layer is significantly affected by the discharge. Figure 4.12 shows the EHD wind generated by DBD with an external flow of 1 m/s. The ions injected from the discharge electrode drift in the electric field and transfer their momentum to the neutral molecules. This increases the velocity of the airflow in the wall boundary layer. In order to investigate the influence of DBD, the velocity profile along different lines perpendicular to the dielectric wall downstream the edge of the discharge electrode has been examined in the case of 20 kV and 1 kHz, assuming an external airflow of 1 m/s (Figure 4.13). The maximum velocity is about 6 m/s, which matches the experimental results reported in [13, 68, 69]. It can also be noticed that the point of maximum velocity is located at a few mm way from the discharge electrode.

Without the DBD, the flow velocity is zero on the wall and gradually increases until it reaches 1 m/s at some distance from the wall. For the case with DBD, the flow velocity on the wall is still zero, which results from the non-slip boundary conditions. However, this velocity sharply increases reaching about 6 m/s at the distance approximately 1 mm from the wall (Figure 4.13). From this point, the velocity starts to decrease eventually approaching 1 m/s far from the wall. Figure 4.15 shows that the EHD wall jet is a few millimeters thick and its length is larger than 30 mm.

Since DBD is created by an alternating voltage, the velocity field fluctuates with time. Figure 4.14 shows these fluctuations for three different spatial positions. It is obvious that the airflow fluctuates with a frequency equal to twice of the voltage frequency. This is caused by the two discharge regimes in one cycle, one dominated by negative ion and one by positive ion. However, in experiments where the asymmetric properties of DBD in positive and negative half-cycles are observed, the frequency of airflow fluctuation is the same to the voltage frequency. Velocity fluctuations are most pronounced near the discharge electrode, whereas variations are almost unnoticeable at a large distance from the electrode. The existing velocity fluctuations indicate the existence of small eddies around the electrode. These eddies significantly change the dynamic properties, such as drag force, in the boundary layer. They are also a major source of energy loss in DBD [125], and by reducing eddies and vortices with an optimal voltage waveform, the efficiency of DBD can be improved as shown in [126, 127].

4.4.3 Effect of External Flow

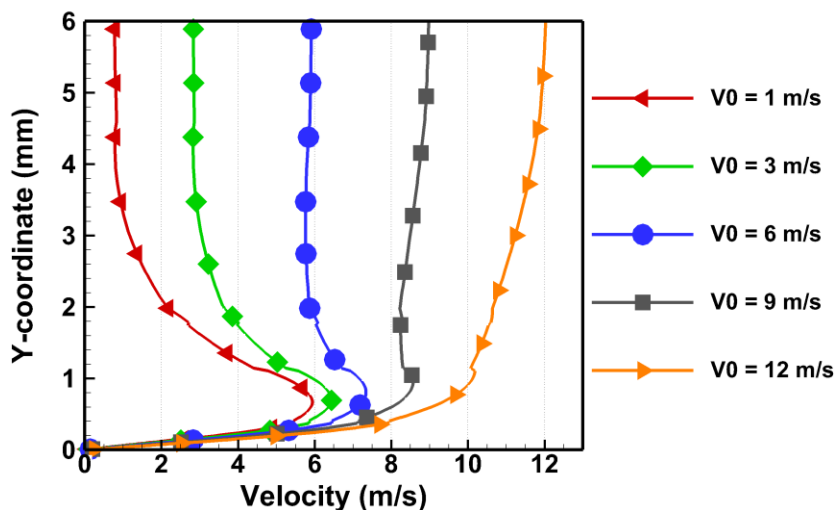


Figure 4.16 Velocity profiles along the line perpendicular to the dielectric wall 15 mm downstream from the discharge electrode.

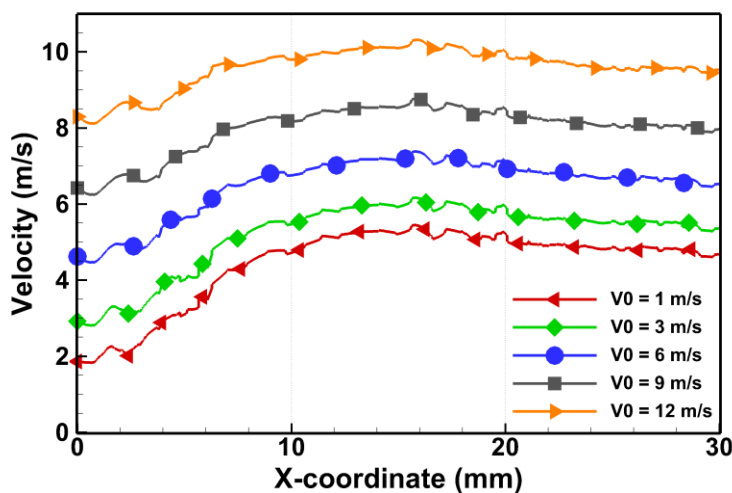


Figure 4.17 Velocity profiles along the line 1 mm above the dielectric wall with different external flows for the 20 kV, 1 kHz case.

Figure 4.16 shows the effects of external flows on the velocity profiles measured along the line perpendicular to the dielectric wall 15 mm downstream from the discharge electrode for the case of 20 kV and 1 kHz. Although the presence of the DBD accelerates the air flow in the boundary layer when the external flow is up to 6 m/s, for the case of a larger external flow velocities the contribution of DBD is significantly reduced. It can be explained by the fact that the discharge

energy is almost the same for different external flows, whereas the energy of different external flows increases with its velocity.

As shown in Figure 4.17, only in the case of a small external flow velocity, the presence of DBD can significantly change the velocity profile. It means that DBD actuators are presently limited for the applications with low external flow velocities. Many researches have been conducted to explore the possibility to enhance the velocity of EHD flow, so that DBD can be utilized in fields with high external velocity such as aerodynamic lifting [119], propellers [128], and plasma gun [129].

4.4.4 Effect of Voltage Level

The intensity of the discharge depends on the voltage magnitude. A higher voltage would result in a larger discharge current, which eventually generates a stronger EHD flow in the boundary layer.

In order to estimate the effect of voltage level, the enhancement velocity factor, which is equal to the velocity produced by the DBD minus the velocity in the case without DBD has been investigated. This factor was calculated in the whole domain at different times in the cycle. The maximum enhancement factor presented in Figure 4.18 demonstrates the influence of voltage on the EHD generated flow. It shows that EHD flow becomes stronger as voltage increases. Moreover, as the velocity of external flow increases, the significance of voltage decreases.

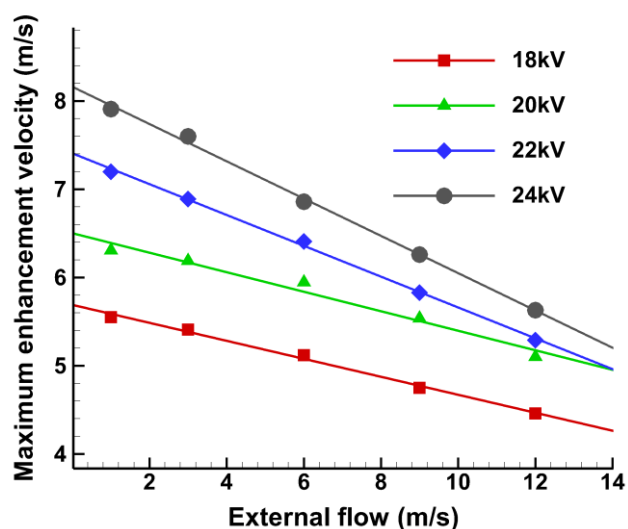


Figure 4.18 The effects of voltage level on the maximum value of enhancement velocity with different external flows (1 kHz).

4.4.5 Effect of Frequency

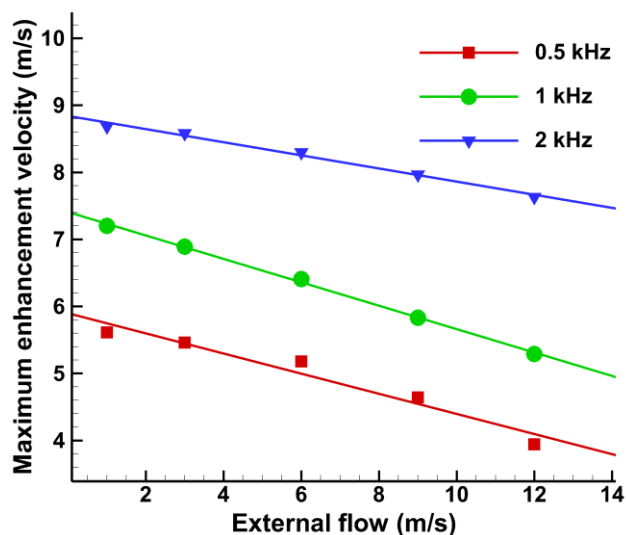


Figure 4.19 The effects of frequency on the maximum value of enhancement velocity with different external flows (22 kV)

The intensity of the discharge also depends on the frequency of the voltage signal. It has been proven [73], and it also can be verified in our model, that the discharge is stronger when a higher frequency is applied: a higher frequency induces a higher velocity in the dielectric boundary. As shown in Figure 4.19, the enhancement velocity factor tends to increase as frequency increases.

4.4.6 Drag Reduction

The drag force on the dielectric surface is composed of a combination of the pressure, viscous and electric forces [119]. Since these forces change over time, the average values for all components were calculated. The pressure force is very small compared with other two forces (~2%), and, therefore, it is a negligible component of the total drag force. The viscous force acts in the direction of the airflow and it increases as the velocity increases that might result from either a stronger external flow or a higher discharge voltage. However, the electric force is in the opposite direction to the viscous force because the surface charge on the dielectric plate repels ions released from the electrode, and this produces an electric counterforce along the dielectric surface.

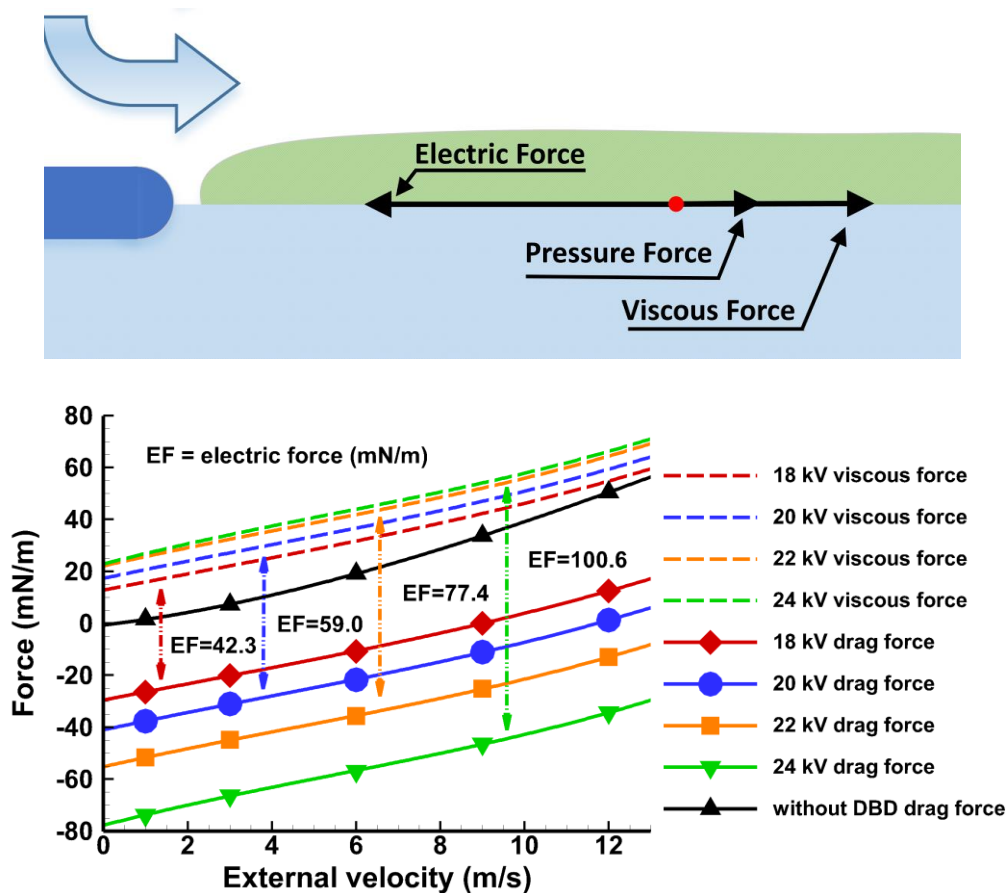


Figure 4.20 a) Forces acting on the dielectric surface and b) total drag force for different conditions calculated at 1 kHz.

Figure 4.20 shows the viscous force, electric force and their sum, the total drag force, under different conditions. On one hand, when the voltage level increases, the viscous force increases a little, while the magnitude of electric force significantly increases, but in the opposite direction,

which leads to the decrease of total drag force. On the other hand, by increasing the velocity of external airflow, the viscous force becomes larger whereas the electric force remains the same, therefore the total drag force increases. Specifically, in the case without DBD, no electric force exists and, therefore, the viscous force is equal to the total drag force. The results of this drag force calculation are reasonable when compared with the experimental data published in [130]. In that paper, the reduction of drag force is about 0.2 mN when 10 kV is applied, where razor blades are used as electrodes whose length is 28 mm.

It is also noticeable that for the external velocity up to some critical values, 9 m/s in this case, the direction of drag force is changed. It indicates the great potential of DBD to modify the characteristics of flow in the boundary layer.

4.4.7 Efficiency

In order to estimate the electromechanical energy conversion efficiency, the mechanical energy can be calculated using

$$P_m = \iint f \cdot v \, ds = \iint (f_x v_x + f_y v_y) \, ds \quad (4.14)$$

where f is the volume force density on the air, which is equal to the Coulomb force of space charge and v is the velocity of air flow. In this study, only the time average mechanical power was investigated, although the time evolution of the mechanical power can also be obtained. Using this along with the results from Equation (4.11) allows the efficiency to be calculated as

$$\eta = P_m/P_e \quad (4.15)$$

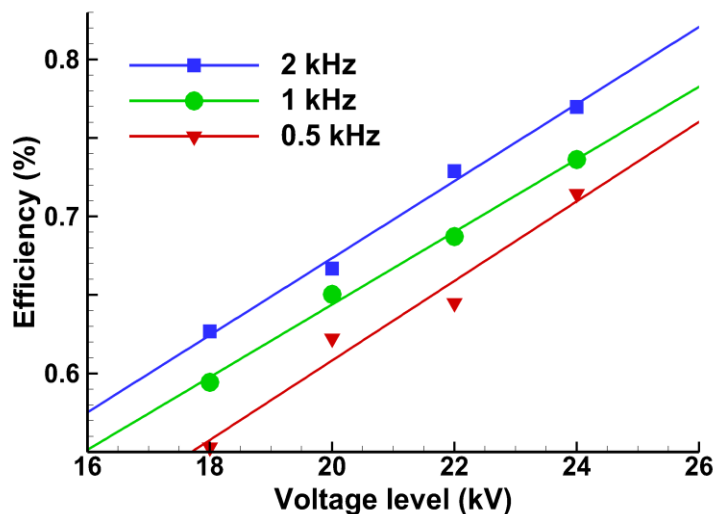


Figure 4.21 Efficiency of a DBD actuator when the external flow is 1 m/s.

Figure 4.21 shows the efficiency when the external flow is equal to 1 m/s. The efficiency increase as the voltage level or frequency increases. It matches the experimental result that the efficiency increases with the discharge current [131]. In experiments [76], the typical efficiency values are in the order of 0.1%, with a maximum value of 0.2%. The simulation value of efficiency is around 0.7%, which is a few times larger than the experimental results. However, it might still be reasonable because of the difficulty to detect force distribution in experiments, as well as the time evolution of the mechanical power.

The DBD actuator efficiency is very low. A large portion of electrical energy is lost in the process of ionization and heating. However, the DBD actuator is effective for flow control, because the induced EHD flow may significantly modify the targeted boundary layer, and it can be easily controlled by the applied voltage, frequency, and geometrical configurations.

4.5 Conclusions

This paper presents the results of a numerical investigation of a model of the DBD using the COMSOL commercial software. In this model, in order to reduce computational time, only two ionic species were assumed, and Kaptzov's hypothesis was adopted to correctly predict the amount of ions produced by discharge. The ions move in the electric field and their collision with neutral air molecules produces an EHD flow. The surface charge on the dielectric wall is produced from the deposition of ions existing above the dielectric plate. Both surface charge and space charge

significantly influence the process of DBD, so that all equations are mutually coupled and have to be solved simultaneously.

The process of DBD was simulated in the time domain, including the effects of the electric field distribution, space charge movement, surface charge accumulation and air flow. The electric field intensity on the electrode was examined, and the current-voltage profile was calculated and compared with experimental results to confirm the correctness of the model. A parametric study shows that either a higher voltage or frequency results in a higher discharge current. Therefore, the intensity of DBD can be easily controlled using electrical parameters. In addition, the time-resolved distribution of space charge and the time-dependent plot of surface charge density are presented.

In addition to the electrostatic characteristics, the mechanical properties of DBD have also been discussed. The discharge induces an EHD flow in the boundary layer with a velocity in the order of a few meters per second. This significantly reduces the drag force on the dielectric wall and can even change its direction under a weak external flow. The actuator mechanical properties can be controlled by the applied voltage level and frequency. A higher voltage or frequency results in a more intense discharge, and, therefore, a faster airflow in the boundary layer. The numerical model reveals details of the DBD characteristics not easily measurable in experiments, and improves our understanding of the physics in the DBD plasma actuator.

Chapter 5

5 Numerical Investigation of Extended DBD for Flow Control

5.1 Introduction

The extended DBD has been experimentally investigated to find a way of enhancing the EHD flow, which is limited up to 8 m/s in the conventional DBD. The extended DBD has a third electrode that is connected to a positive DC voltage. It provides a DC bias that intensifies the negative phase of the plasma discharge and depresses the positive one. According to Moreau, the negative half-cycle contributes more than the positive half-cycle to the airflow acceleration [107]. Therefore, it is probable, that the extended DBD has the capability to strengthen the EHD flow.

However, the experimental results show that the extended DBD can accelerate the EHD flow but only very slightly. Moreover, different research groups used different configurations in their experiments [105, 106, 108]. These studies generate results which seem not to agree with each other. In order to investigate the reason for this, a numerical model of the extended DBD is proposed and the simulation results are discussed in this Chapter.

5.2 Numerical Model

The numerical model of the extended DBD is developed based on that for the conventional DBD whose correctness has already been proved in Chapter 4. The modification mainly lies in the geometry and boundary condition on the third electrode that is connected to the positive DC voltage.

5.2.1 Geometry

The extended DBD actuator consists of three strip electrodes, two exposed and one buried in a dielectric plate. The two exposed electrodes are 0.08-mm thick copper strips with a gap of 40 mm. The grounded electrode is a 0.2-mm thick strip placed 2 mm below and 4 mm away from each exposed electrode. The dielectric plate is made of PMMA having relative permittivity of 4.5. Its thickness is 5 mm and width is 80 mm.

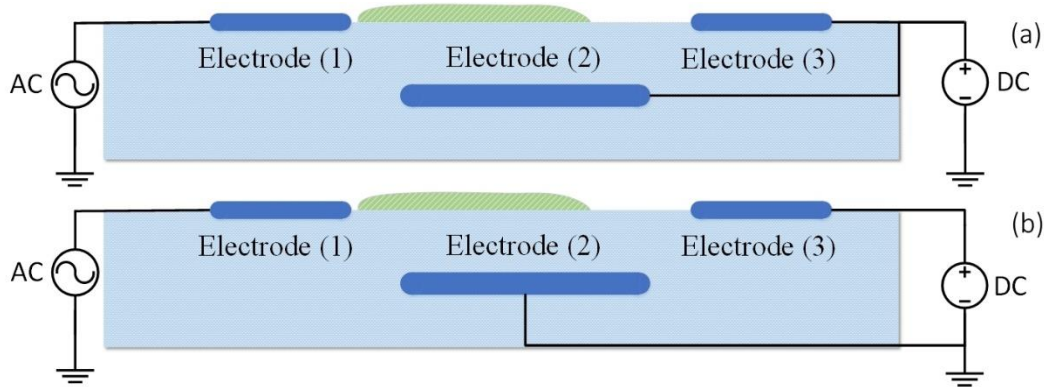


Figure 5.1 Unscaled sketch of the extended DBD actuator in two configurations.

The electrode (1) is supplied with a sinusoidal voltage with amplitude of 20 kV and frequency of 1 kHz. In the configuration experimentally studied by Moreau (Figure 5.1a) [108], the electrode (2) is supplied with a high DC voltage, the same as supplied to the electrode (3). However, the electrode (2) is grounded in Nishida and Debien's experiments (Figure 5.1b) [105, 106]. This relatively minor difference in the power connection has significant effects on the characteristics of the extended DBD. The reason for that will be revealed in this Chapter.

5.2.2 Numerical Algorithm

Similarly as in the simple DBD model, the ionization layer in the extended DBD model is ignored and positive or negative ions are injected from the area near the electrode surface. The drift dynamics of both ions are included to evaluate the surface charge accumulation. However, the dynamics of the ionic reactions is neglected to save computing time. As a result, the streamer discharges and Trichel pulses are ignored in the numerical model. The details of the numerical algorithms including Poisson equation, Peek's formula, charge transport equation and Navier-Stokes equation can be found in Chapter 4.2.

5.2.3 Boundary Conditions

There is no discharge on the tip of electrode (3) in the Moreau's model (Figure 5.1a), whereas a positive discharge would occur on the electrode (3) in the Nishida's model (Figure 5.1b) once the applied DC voltage reaches a threshold value. Therefore, the boundary conditions on the electrode (3) should be modified according to the model configuration.

In the case without discharge on the electrode (3), the concentration of species on the electrode (3) is equal to zero. Any ions reaching the electrode will be absorbed or neutralized. However, in the case with the presence of discharges on the electrode (3), the concentration of species on its tip varies according to the applied voltage. The value of the concentration is determined by the Peek's formula, which is calculated by a MATLAB routine coupled to COMSOL.

5.3 Simulation Results for the Model Studied by Moreau

Moreau studied the extended DBD in the configuration shown in Figure 5.1a. The numerical model reveals that the applied DC voltage can slightly modify the velocity of EHD flow. It also proves that the absence of the electrode (3) does not change the properties of the extended DBD, when the electrode (2) is connected to the positive DC voltage.

5.3.1 Three-electrode Configuration

Figure 5.2 shows the current waveform in the extended DBD (Figure 5.1a) when $V_{dc}=0$ kV and 4 kV. When the DC voltage is equal to zero, the configuration is very similar to a simple DBD. The current is symmetric in the positive and negative half cycles. However, when the voltage is equal to 4 kV, the negative current is higher than the positive one. This means that the positive DC voltage can suppress the positive discharge and enhance the negative discharge. This can be confirmed by the time-dependent plot of the space charge density on the tip of the electrode (1), as shown in Figure 5.3. The x-axis is the arc length of the tip of the electrode (1), the y-axis is proportional to time (arbitrary units) and the color graph represents the space charge density near the electrode tip. The highest value of the negative charge density in space is 0.19 C/m^3 , which is slightly larger than the maximum positive charge density of 0.17 C/m^3 . It can also be predicted that the negative discharge intensity will increase with the positive DC voltage.

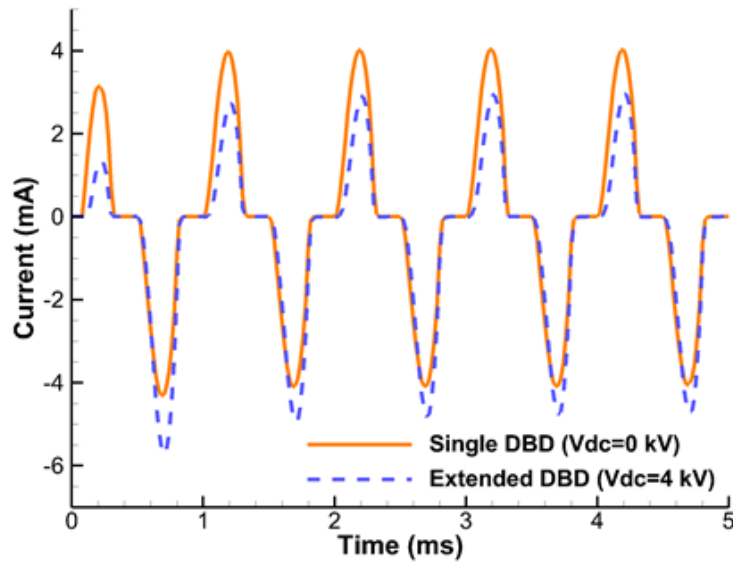


Figure 5.2 Current waveform in the first five voltage cycles when the DC voltage equal to 0 kV and 4 kV.

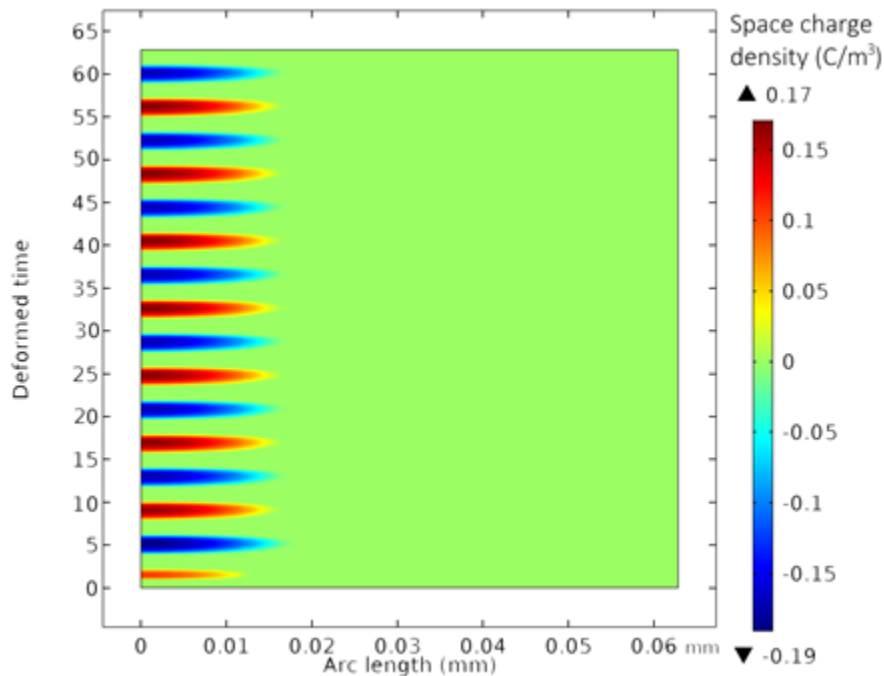


Figure 5.3 Time-dependent plot of the space charge density on the electrode (1).

Since the electrodes (2) and (3) are applied with the same DC voltage, the electric field intensity on the electrode (3) is very low. The simulation predicts that its maximum value is 4 kV/cm, which is far below Peek's value equal to 182 kV/cm in this model. As a result, there is no discharge or positive ions created on the electrode (3).

Although it was reported in [13] that the extended DBD can slightly increase the maximum velocity in the order of 0.1 m/s, Moreau presented the contradicting results that the time-averaged velocity in the extended DBD might be smaller than that in the simple DBD [108]. In the presented numerical model, the velocity enhancement is not obvious. Figure 5.4 shows the velocity profiles of the extended DBD and the simple DBD along a vertical line $X=5$ mm from the active electrode tip. The presence of 4 kV DC voltage does not make a significant difference. This can be explained by the fact that the velocity enhancement in the negative half cycle is compensated by the velocity reduction in the positive half cycle. Therefore, the extended DBD does not enhance the EHD flow. However, this influence depends on the value of the AC and DC voltages, as well as the geometry.

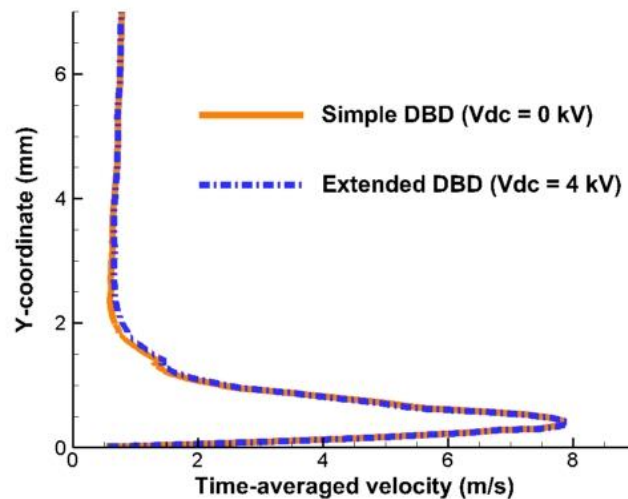


Figure 5.4 Time-averaged velocity of the EHD wind along the vertical line $X=5$ mm from the edge of the active electrode for the DC voltage equal to 0 kV and 4 kV.

5.3.2 The Role of the Third Electrode

The electrodes (2) and (3) play the same role of providing DC bias for the plasma discharge on the electrode (1). In order to figure out the role of the electrode (3), a new model without the electrode (3) has been investigated when $V_{dc}=4$ kV (Figure 5.5).

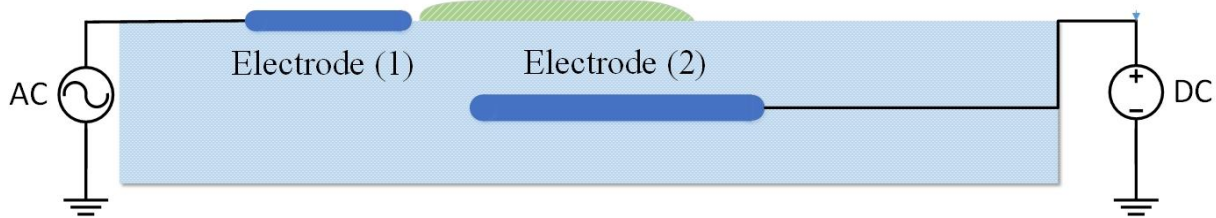


Figure 5.5 Unscaled sketch of the two-electrode actuator. The electrode (2) is connected to a DC voltage of 4 kV.

The two-electrode model yields the same current waveform as the extended DBD shown in Figure 5.2. It means that the absence of the electrode (3) would not affect the properties of the extended DBD actuator.

To conclude, the DC voltage can slightly change the mechanical performances of the DBD, but it does not bring better values than an optimized simple DBD. In addition, the geometric configuration in Figure 5.1a can be simplified into the structure in Figure 5.5, where the third electrode is not needed.

5.4 Simulation Results for the Model Studied by Nishida

The extended DBD model studied by Nishida, with the electrode (1) supplied with an AC voltage, the electrode (2) grounded and the electrode (3) connected to a positive DC voltage source, has also been simulated. The experimental observations indicate that this positive DC voltage can significantly affect the plasma discharge and the coexisting EHD flow.

5.4.1 Low DC Voltage

In order to understand the role of the DC voltage, its contribution to the electric field on electrodes (1) and (3) has been investigated. Figure 5.6 shows that the electric field intensity on the electrode (3) increases with the applied DC voltage. When the positive DC voltage is less than 10.4 kV, the maximum electric field intensity on the DC electrode is below Peek's value. In this case, there is no discharge on the DC electrode.

According to the principle of superposition, each electrode creates its own electric field independent of the other electrodes. Without considering the drifting ions, the resultant electric field on the electrode (1) is a vector sum of the electric field contributed by each electrode. Figure

5.7 shows the electric field component E' that is contributed by the DC electrode to the electrode (1). The x-axis is the arc length of the tip of the electrode (1), the y-axis is the value of applied DC voltage and the color represents the magnitude of the contributed electric field. Although the electric field contributed by the DC electrode increases with the DC voltage, it is two orders of magnitude smaller than Peek's value. This means the DC electrode has negligible influence on either the plasma discharge or the EHD flow.

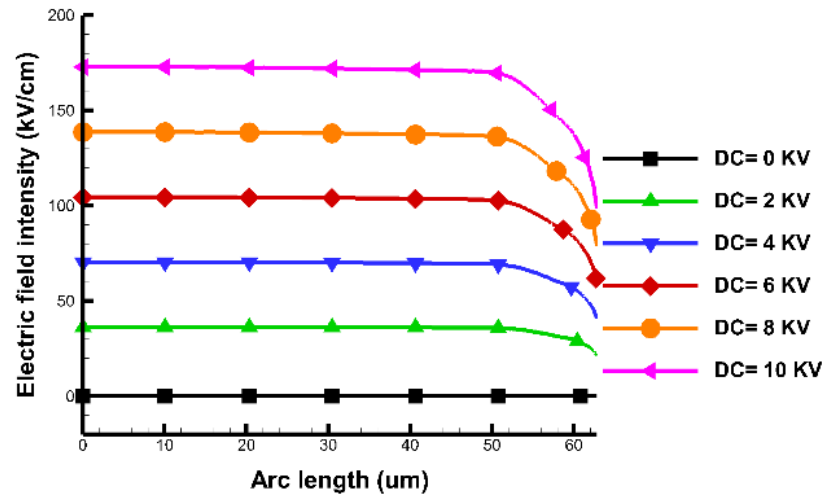


Figure 5.6 Electric field intensity on the tip of the electrode (3).

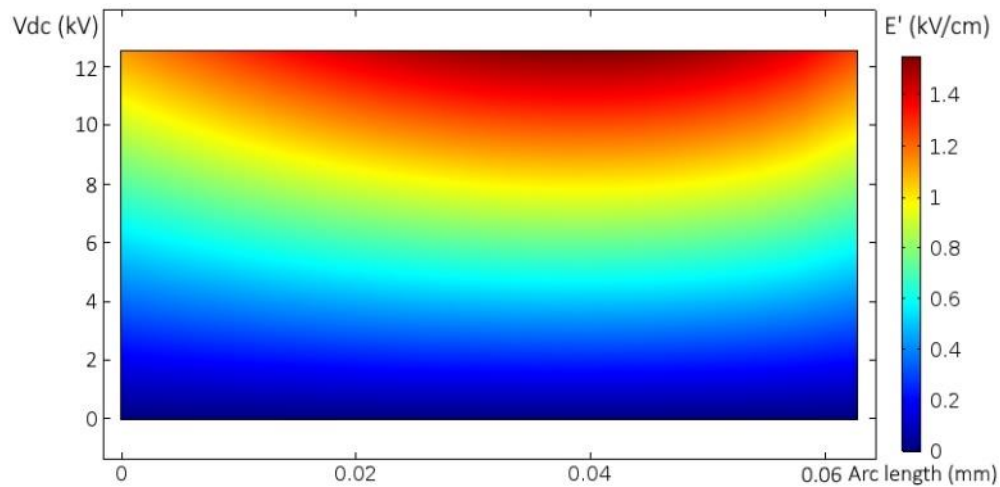


Figure 5.7 The electric field contributed by the DC electrode on the electrode (1) tip.

The simulation results also reveal that the current waveform and velocity field remain the same when the DC voltage ranges from 0 kV to 10 kV, as shown in Figure 5.8 and Figure 5.9. The presence of the positive DC electrode (3) does not significantly change the properties of the

actuator. This can be explained by the electromagnetic shielding effect generated by the electrode (2), which restrains the influence of the DC electrode on the discharge.

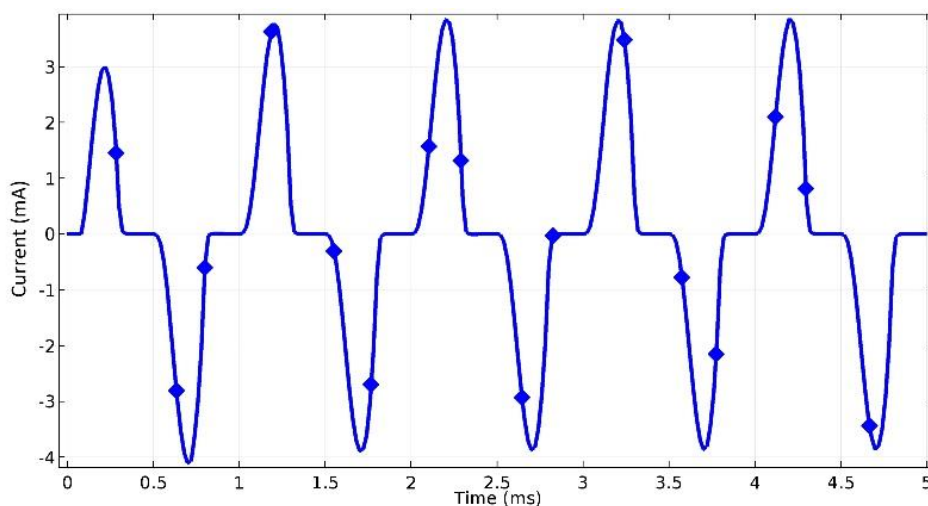


Figure 5.8 The current waveform in the first 5 cycles regardless of the DC voltage ranging from 0 kV to 10 kV.

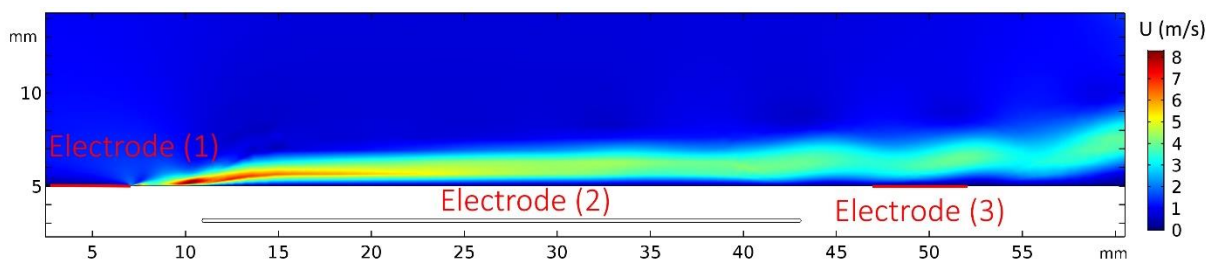


Figure 5.9 Time-averaged velocity field regardless of the DC voltage ranging from 0 kV to 10 kV.

Figure 5.10 shows that most of the electric lines of force originated from the DC electrode terminate on the grounded electrode (2). As a result, when the applied DC voltage is not too large, the DC electrode has modest influence on the plasma discharge and the associated EHD flow. This was proven in the experiment conducted by Nishida, where the generated thrust remains the same before the DC voltage amplitude exceeds a threshold value [105].

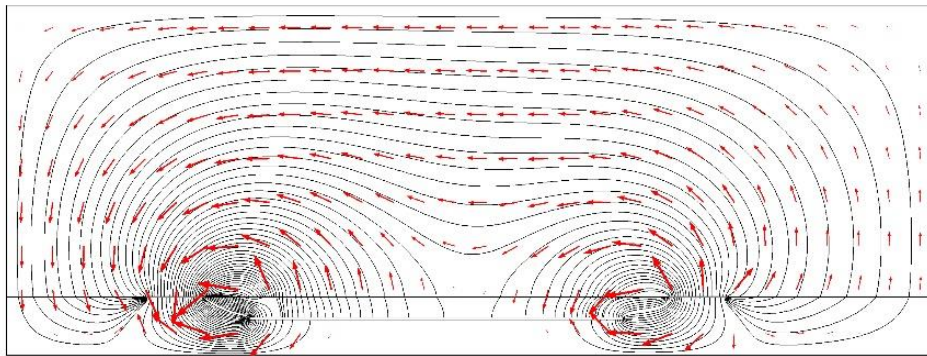


Figure 5.10 Electric lines of force over the domain at one time point.

5.4.2 High DC Voltage

Once the DC voltage is larger than a threshold value of 10.4 kV in this model, the maximum electric field intensity on the DC electrode will exceed Peek's value. Then, a positive corona discharge occurs and generates an EHD wind flowing from the DC electrode (3) to the grounded electrode (2). This will produce a counter flow as experimentally observed in [105].

Figure 5.11 shows the current waveform when the DC voltage is 20 kV. The initial positive current peak is caused by the corona discharge on the DC electrode. After the first voltage cycle, the maximum value of the positive current is roughly equal to that of the negative current. There is no obvious evidence for the existence of the positive corona discharge. In other words, the corona discharge on the DC electrode only appears in the first voltage cycle and then disappears in the following cycles.

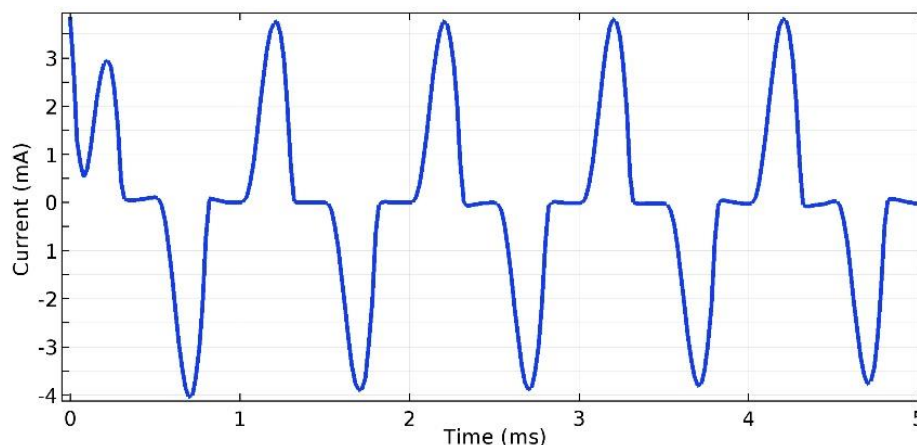


Figure 5.11 Current waveform in the first 5 cycles when $V_{dc}=20$ kV.

In order to determine the reason, the surface charge density on the dielectric plate was been taken into consideration, as shown in Figure 5.12. The x-axis is the arc length of the dielectric plate between the electrodes (1) and (3), the y-axis is proportional to time and the color graph represents the surface charge density. It shows the time-varying distribution of the surface charge on the dielectric plate. On the left side, the polarity of the surface charge changes according to the phase of the AC voltage applied on the electrode (1). On the right side, the value is always positive because only positive ions can be injected from the positive DC electrode (3) and be deposited on the dielectric surface. These positive surface charges create a reverse electric field that suppresses and eventually stops the discharge on the DC electrode.

It should be noted that the discharge patterns could be different in the real world. The highly concentrated positive surface charge near the DC electrode might cause micro-discharges and secondary electron emissions through which positive ions might be released or neutralized. After that, another positive corona discharge would occur and generate an EHD flow at the same time. In addition, the numerical model neglects the drift dynamics of the surface charge, but in reality it might play an important role when the surface charge concentration is sufficiently high.

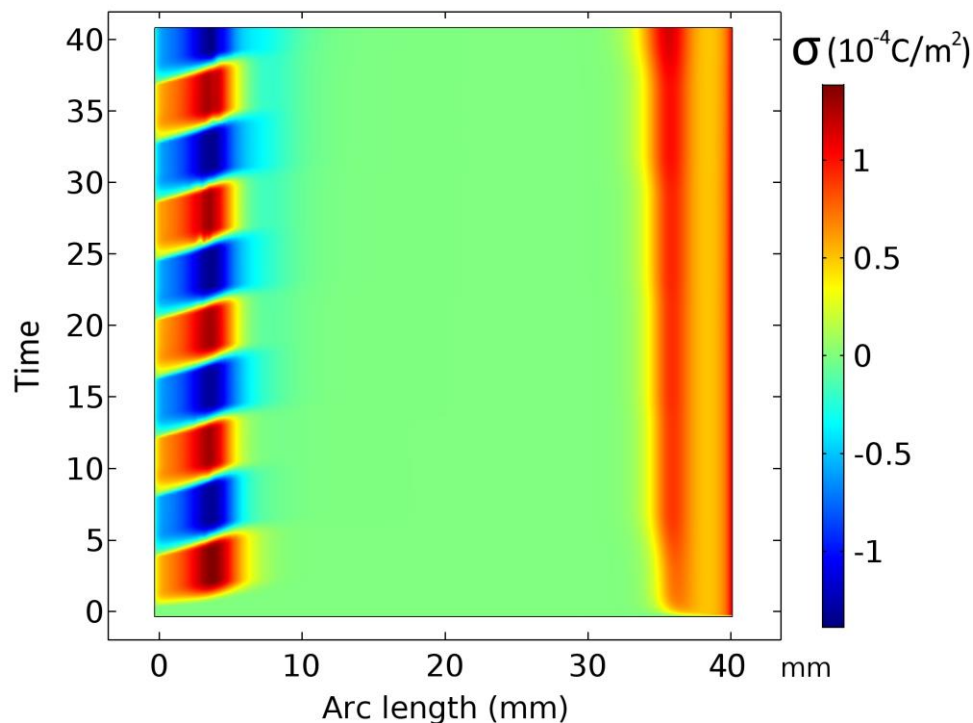


Figure 5.12 Time-dependent plot of the surface charge density on the dielectric plate.

The corona discharge on the DC electrode not only affects the electrical properties, but also changes the dynamic properties of the plasma actuator. Figure 12 shows the EHD flows generated by the electrodes (1) and (3). The maximum value of time-averaged velocity is about 8 m/s, which is the same to the maximum value in the case without the DC electrode. It means the DC electrode does not increase the EHD flow velocity.

However, compared with the conventional DBD actuator that induces an EHD flow parallel to the dielectric surface, two EHD flows are induced in this configuration of the extended DBD, one is from the AC electrode and the other is from the DC electrode. The interaction of the opposed flows creates a jet perpendicular to the dielectric surface. Its strength and direction can be modified by changing the AC voltage as well as the DC voltage. This concept of controlling the jet vector direction can be used in the application called “plasma synthetic actuator” [132, 133].

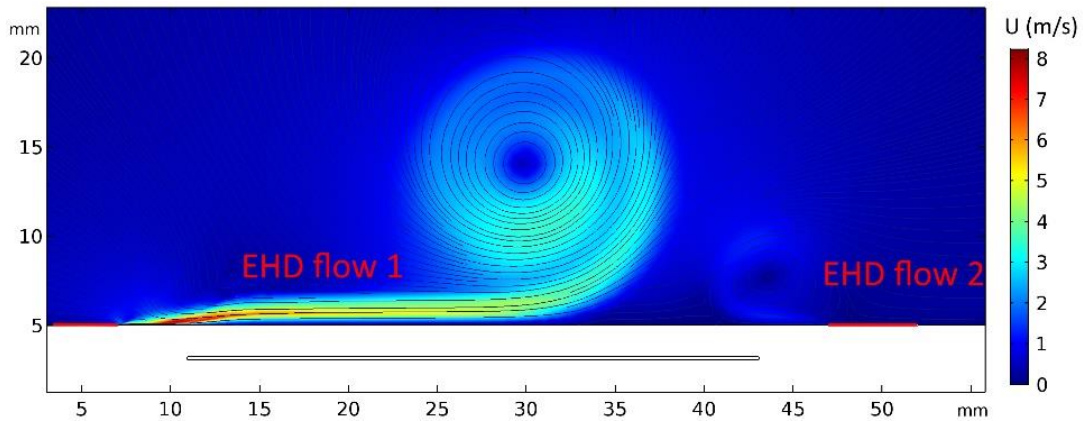


Figure 5.13 Time-averaged velocity field when $V_{dc}=20$ kV.

Experiments reveal that the extended DBD allows the increase of the EHD force, by 10% ~ 45 % as reported by Debien [106]. The EHD force can be calculated with the following equation:

$$f_{EHD} = \iint \sqrt{(E_x \times \rho_c)^2 + (E_y \times \rho_c)^2} ds \quad (5.1)$$

where the E_x , E_y is the x component and y component of the electric field intensity, respectively, ρ_c is the space charge density, and ds denotes the surface integration. As shown in Figure 5.14, the extended DBD increases the EHD force by about 12% when $V_{dc} = 20$ kV. This simulated improvement of EHD force is in the range as observed in experiments.

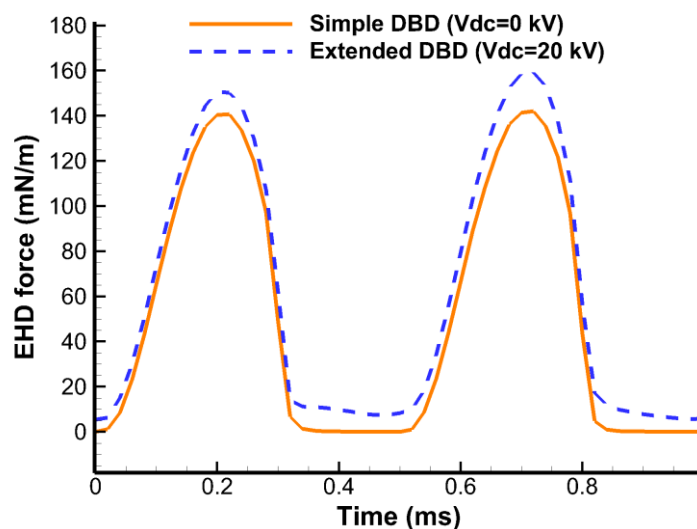


Figure 5.14 EHD force induced by the simple DBD and the extended DBD in one typical cycle.

In summary, when the electrode (2) is grounded, the DC electrode does not contribute to enhancing the EHD flow generated by the electrode (1). However, when the DC voltage is larger than a threshold value, a positive corona discharge occurs on the DC electrode. This will generate a counter flow whose strength and direction can be modified by the applied voltage.

5.5 Conclusions

In this Chapter, two configurations of the extended DBD have been numerically investigated; the electrical and mechanical properties including the current waveform, space charge density, surface charge density, velocity profiles and the EHD force have been simulated. The results show that the embedded electrode (2) plays an important role in the extended DBD. When it is supplied with a high positive DC voltage, it strengthens the negative discharge and suppresses the positive discharge on the AC electrode, but has little influence on the EHD wind. In this case, there is no need for a third electrode to create the DC biased dielectric barrier discharge. On the other hand, when the embedded electrode is grounded, it generates the electric shielding that eliminates the influence of the DC voltage on the discharge. Once the DC voltage exceeds the threshold value, a corona discharge occurs between the DC electrode and the embedded electrode. As a result, a reflected jet perpendicular to the dielectric wall appears.

Generally speaking, the extended DBD can hardly enhance the EHD flow regardless of its various forms. It cannot satisfy the needs of the large EHD flow impractical applications, especially in aerodynamics. One promising application of the extended DBD is the plasma synthetic actuator that can modify the direction of the EHD flow by changing the applied DC voltage.

Chapter 6

6 Conclusions and Future Work

6.1 Summary

This thesis presents the results of a series of numerical investigations of the EHD flow generated by the corona discharge, the dielectric barrier discharge, and the extended DBD.

6.1.1 Corona Discharge

A numerical model to determine the electric field intensity, space charge density and mass transport in a multiple pin-plate electrohydrodynamic dryer has been developed. The discharge process was modeled by adopting Kaptzov's hypothesis, which neglects the ionization layer and assumes that the charges are injected from the surface of the discharge electrode. The electric force on the drifting ions provides the volume force for the formation of the EHD flow. It was found that:

- i. The corona onset voltage depends largely on the electrode geometry, decreasing for smaller gaps between electrodes and larger spacing between pins.
- ii. The corona current depends on voltage, gap and electrode geometry.
- iii. Airflow mass flux generated by the multiple-pin electrode is proportional to the voltage and square root of electric current.
- iv. The existence of aerodynamic vortices with different geometric configurations is predicted by the numerical model.

The model has been experimentally validated in drying experiments using wet paper tissue. The model-predicted voltage-current characteristics matched the experimental data. The results of the drying experiments also support the initial hypothesis that mass transport from wet material is proportional to air mass flow approaching its surface. Comparison between the drying with the electrode with 2×2 cm spacing between pins and that with 1×1 spacing shows that the geometry configuration significantly affected charge distribution, aerodynamics of airflow and mass transfer.

6.1.2 Dielectric Barrier Discharge

A numerical model for simulation of the dielectric barrier discharge (DBD) generated by a sinusoidal voltage has been presented. In this model, the ionization layer is neglected and two species (positive ions and negative ions) are injected from the discharge electrode surface according to Kaptzov's hypothesis. The movement of the ions' creates corona current and EHD flow. Some ions are also deposited on the dielectric plate resulting in surface charge accumulation. These phenomena are coupled with each other and solved simultaneously. It was found that:

- i. DBD eventually evolves into a quasi-steady state phenomenon with the same frequency as the applied voltage.
- ii. The electric field needs a few voltage cycles to reach a quasi-steady state, but the velocity field needs more than 30 voltage cycles.
- iii. There is a phase difference between the voltage and current caused by the capacitive effect.
- iv. The current depends on the voltage magnitude, frequency and geometry.
- v. The distribution of space charge and surface charge has been predicted by the numerical model.
- vi. An EHD jet flow with a velocity up to 8 m/s and the thickness of about 4 mm can be generated above the dielectric plate.
- vii. The presence of an external flow decreases the contribution of DBD on the velocity of EHD flow.
- viii. The drag force in the boundary layer can be significantly modified by the EHD flow generated by DBD.
- ix. The efficiency of the electromechanical energy conversion is around 1% and it increases with the voltage level as well as with the frequency.

Most of the characteristics mentioned above have been verified by experiments available in the literature. This numerical investigations not only reveal the results that can be experimentally observed, but also explain these phenomena in detail. It improves the understanding of the physics of the DBD as well as the associated EHD flow.

6.1.3 Extended DBD

Two numerical models of the extended DBD have been developed and examined in this thesis. This study is based on the previous model of DBD, but after including an additional electrode connected to a high DC voltage. It was found that:

- i. When the embedded electrode is connected with the DC electrode, the applied DC voltage has limited influence on the EHD flow as well as the discharge.
- ii. When the embedded electrode is grounded, the DC electrode cannot affect the EHD flow if its voltage is below the threshold.
- iii. When the embedded electrode is grounded, the DC electrode generates an EHD flow against that from the AC electrode, which eventually forms a jet perpendicular to the dielectric wall.

This study attempted to combine the results of previous experiments reported in the literature with different geometric configurations conducted by different research groups, in order to find out the reason for the difference between their results. It clears the road for the further exploration on the extended DBD.

6.2 Conclusions

All the work done in this thesis can be concluded in a few points as following:

- i. Several models of plasma discharges have been successfully developed, and the correctness have been confirmed by comparison with experiments.
- ii. A more intense plasma discharge usually corresponds to a larger EHD flow.
- iii. The velocity patterns of EHD flows are subjected to many parameters, such as the applied voltage magnitude, frequency, external flow and geometric configurations.
- iv. The EHD flow can be applied to enhance the drying rate and reduce the drag force in the boundary layer.
- v. Plasma actuators are presently limited for applications with low external flow velocities.
- vi. Plasma discharges have the advantage of low power consumption, but also the disadvantage of low efficiency of electromechanical energy conversion.

- vii. The presence of an additional electrode applied with high positive DC voltage has little influence on the dielectric barrier discharge and the EHD flow.

6.3 Reflections on the Numerical Simulation

A major challenge in developing the numerical simulation described in this thesis was not only how to model the multi-physical process of the discharges, but also how to simplify the model and make the calculation time affordable. In addition, the results of the simulation need to be thoughtfully compared with the experimental data in order to validate the numerical model. Otherwise, the simulation brings out nothing, but fictitious results and further misunderstanding.

Many problems, such as the unknown boundary condition, model simplification, algorithm divergence and others, need to be addressed properly in the numerical modeling. The solutions for these problems usually come from a wider point of view and the knowledge gained from conducting experiments or studying the results available in literature.

The goal of a numerical investigations is not only to replicate the data coming from the experiment, but also to dig deeper into the physical phenomena and provide their more comprehensive understanding. A good numerical model would bring vivid and reliable results that could not be generated in experiments. These results can even give the direction for the future experiments or industrial designs. This will provoke the interests of the new researchers and push the research forward. Moreover, some experiments cannot be easily conducted due to its complexity and high financial cost, where numerical simulation provides an alternative way to continue the research in a more accessible and productive way.

In this following section, the author gives some reflections on the general ideas as well as the practical strategies to deal with issues in the simulation of the plasma discharges.

6.3.1 Modeling

From the numerical point of view, the physical world is a function of lots of variables such as time, space, temperature, pressure, voltage, energy and others. Therefore, physical phenomena can be modeled using a set of partial differential equations (PDEs) of multiple variables. By correctly solving these PDEs, the numerical results can theoretically replicate the reality.

The major challenge in modeling the plasma discharge lies in the complexity of different physical mechanisms. The plasma discharge includes hundreds of ion reactions as well as many other complicated mechanisms, which are beyond the computing capability of modern computers. It is not possible to reveal the behavior of every ion in reality through simulation, but the general characteristics can be obtained. The numerical model should be progressively developed from a simple form to a complex, but more accurate one. For instance, in the initial study of the corona discharge, the space charge density on the electrode was manually set and adjusted. Then, a MATLAB routine was developed to automatically inject the space charge density on the electrode in a more accurate way. The previous experience from a simple model would help to generate the idea of a more realistic model and how to modify it if some errors occur.

The numerical model should also be developed with proper simplifications based on the research goal. By wisely simplifying the problem according to this goal, physical phenomena can be modeled without too much complexity or unnecessary detail. For example, in the positive corona discharge, the EHD wind is generated mainly due to the positive ions, and thus the presence of electrons and negative ions could be neglected. This one-species model would provide sufficient information for the research on the corona-related EHD wind and drying effects, while more species and their reactions should be included in the model studying the streamer discharge in the positive corona discharge.

Not only the partial differential equations, but also the boundary conditions matter in the numerical modeling. The boundary conditions are vulnerable to the change of any parameters. Even a small modification on the model would result in the change of the boundary conditions. For example, in the extended DBD, the additional DC electrode would release the space charge into space once the DC voltage exceeds a critical value. It shows that even for the model with a fixed geometry and well-known physical mechanisms, the boundary conditions can be different according to the numerical parameters, such as voltage. In COMSOL, each boundary condition corresponds to one or a few realistic situations and they should be carefully chosen with a deep understanding of the physics of the plasma discharge.

6.3.2 Reducing the Calculation Time

The numerical investigations of the plasma discharge not only require a well-developed model, but also proper solution techniques. Some models are abandoned due to excessive computational requirements. To have a productive model, the calculation should be sped up.

The calculation domain and mesh play an important role in reducing the computing time. In COMSOL, Finite Element Method is applied over the calculation domain, which is discretized into a set of sub-domains, usually called elements. By minimizing the calculation domain and optimizing the mesh, the number of elements can be decreased and the calculations can be accelerated. However, a coarse mesh does not necessarily mean faster calculations. In the geometry of the plasma discharge system, the mesh in the region around the hemi-spherical electrode should be extremely fine and the transition to the coarse mesh in the region away from the electrode should be very smooth. Otherwise, an improper mesh would result in divergence or increased number of iterations to reach convergence.

The computations of the numerical model can also be sped up at the cost of the accuracy of the results. The calculation time can be reduced by adopting problem simplifications. For example, the EHD flow generated by the plasma discharge can be modeled either as a laminar or a turbulent flow. The former is simpler and requires less computing time, whereas the latter is more accurate, but it increases the computing requirements more than three times. It is probably wise to choose a laminar flow model to simulate the EHD flow, if the research interest is the overall pattern of EHD flow instead of the local vortices. In addition, the solution over one element in COMSOL can be interpolated by functions with different orders ranging from one to seven. A higher order usually provides more accurate results, but it increases the number of the degrees of freedom and computing time.

Moreover, the numerical solver can be customized to the problem in order to save the computing time. First of all, we can choose a solver that can either be a direct solver or an iterative solver with different options for handling the problem nonlinearity. The problem can be solved using segregated or a fully coupled approach. Secondly, many parameters in the setting of the solver, such as the recovery damping factor and the tolerance factor, have impacts on the calculation time as well as the accuracy. Last, but not least, the scaling of dependent variables is very important.

By manually setting proper values of the dependent variables, instead of using automatic scaling that needs to be calculated in every interaction, the calculation time can be reduced to one fourth according to the author's experiences.

A few other methods for reducing computation time have been applied in this thesis. In the DBD plasma actuator, the electrical field and charge distribution can reach a quasi-steady state after 5 voltage cycles, but the EHD flow probably needs more than 30 voltage cycles, so that the flow is fully developed in the whole domain. In other words, the mechanical time constant is much longer than the electrical one. In this case, we do not need to simulate both parts together for 50 voltage cycles, because the last 45 cycles of the electric part only repeat and do not provide any additional information. We can simulate the electrical part for a few voltage cycles and then use the results of the last voltage cycle (in a quasi-steady state) to repeatedly simulate the EHD wind. This not only saves the computing time, but also lowers the memory allocation and reduces the size of the model file.

Another practical way for improving the work efficiency is to remotely control the simulation process. The numerical calculation usually takes hours or days for each run. There is no need to wait in front of the computer for the outcome. The author used remote controlling provided by TeamViewer (GmbH, Germany) so that the models can be run or modified anytime when the author has access to the internet. In addition, running multiple models at the same time on the same computer is not a good option, as they would compete for resources (RAM, in particular) and, therefore, take longer to run simultaneously than they would do sequentially. The author also found a way to run the simulations in the batch mode from the command line, which automatically launches the numerical models one after the other. It allows the models to be continuously running day and night. Other techniques, such as cluster study, can also be applied to distribute the calculation among a group of computers and reduce the computing time, but it has never been tried due to the lack of software license and computers.

6.3.3 Divergence

A working model must have a converged solution, although sometimes the solution might not be accurate. The hardest part in the numerical investigation might not be to build a model, but to make it work and generate a reasonable solution. It took the author a long time to modify the model,

especially for the DBD plasma actuator, because it is hard to find the reason of the divergence due to the complexity of the physical mechanisms involved. To the author's best knowledge, the following aspects should first be considered when having the divergence problem.

a) Boundary conditions

Many problems of divergence come from the incorrect setting of boundary conditions. As mentioned above, boundary conditions are vulnerable to the change of some parameters. For example, in the DBD model with the external flow of 6 m/s, the left domain boundary should be set as "V=6 m/s". However, when the external flow is 0 m/s, the left domain boundary should be set as "open boundary" where the normal stress is equal to 0 N/m², instead of "V=0 m/s". The latter one would easily induce divergence because of the absence of inlet air molecules and the presence of the outlet EHD flow. In addition, the boundary conditions on the interfaces of different materials might be extremely complicated. In the DBD model, some space charges are deposited on the dielectric plate as the surface charge where the negative ion recombines with the positive ion. On the dielectric boundary, the disappearance of the space charge and the appearance of the surface charge should be taken into consideration simultaneously. Any inaccurate setting of the dielectric boundary would easily cause divergence since the discharge electrode mounted on the dielectric plate creates a strong electric field and large flux of space charge in that region.

b) Physical mechanisms

The divergence may also result from the oversimplification or the over-complexity of a model. On one hand, if some important mechanisms are neglected, the model might not be able to solve the problem for given boundary conditions. For example, if the recombination of positive ion and negative ion is not considered, there will be more and more charges kept in the domain, which eventually results in the divergence. On the other hand, if the DBD model involves many other effects, such as the electron temperature, pressure and humidity, it might be too complex to be solved and a divergence in iterations can occur very easily.

c) Mesh

Divergence can also be caused by an improper mesh. In a complex geometry, the mesh is usually non-uniform. An unsmooth transition of the mesh density from one region to another can produce large residual error as well as large flux. If the residual error can be accumulated to a critical value,

a divergence would occur at that time. Therefore, a proper mesh should be generated according to the geometry and physical mechanisms involved in the model.

d) Accuracy of the calculation

Sometimes, the divergence can be handled by simply enhancing the accuracy of the calculation. Although more accurate calculations take more time, they can help to get converged results. For example, by replacing the linear interpolation with the quadratic, the residual error could be small enough to avoid the divergence. There is no theoretical guideline about which level of accuracy should be applied in which problem; it can be used according to the user's experiences.

e) Coupled functions

COMSOL can be linked to other software such as MATLAB to input and output intermediate results. In this thesis, a MATLAB routine is applied to automatically inject space charges to the surface of the discharge electrode according to Kaptsov's hypothesis. Since COMSOL is not an open-source software, the process of utilizing the data from MATLAB is unknown, just like a black box. Therefore, even if the algorithm using the MATLAB routine seems to be correct, it may create divergence with some reasons cannot be identified. The author had this problem once in building the DBD model, and had to closely examine the intermediate data and use the trial and error method to solve the problem.

f) Embedded symbols

There are some embedded mathematical functions and operators in COMSOL. Not all of them are clearly defined in the documentation, especially the information about direction of vectors. The author has collected some experience about using "up" function to refer the electric field on the upper boundary of the interface between the dielectric and the air. However, when the geometry was modified later on, this had to be changed to "down" function to refer to the same boundary. This surprising change brings some confusion but needs to be handled well to have a reliable numerical model.

g) Finding a solution

A problem needs to be defined before it can be solved. In order to solve the occurred divergence, it is first necessary to figure out the reason. The situation might be very complex when there is more than one reason. The most practical strategy is to stop the calculation before the divergence and investigate the intermediate results. Then trying to find out what is abnormal and then trace it

back to the original reason. The strategy emphasizes the analysis of the existing results in order to find out the reason for the divergence. Although it is still very hard to apply the strategy in a practical case, it provokes the awareness of analyzing the problem instead of just using the trial-and-error method.

6.3.4 Validation of the Numerical Model

Sometimes, even though the numerical model yields a converged solution, it is not necessarily correct because it could be a “fake solution”. Like an equation having multiple solutions, a numerical model can also be converged at a solution different from the reality. In order to prove the correctness of the model, the numerical results need to be compared with the experimental data available in the literature.

On one hand, a good numerical model would produce the results very close to the experimental data. For example, in the Chapter 4 on the DBD plasma actuator, the simulated results of the velocity-current characteristics and the velocity profiles match those in the experiment pretty well.

On the other hand, no numerical model is perfectly accurate and there is always a difference between the simulated and the experimental results. Therefore, the comparison should not only concentrate on the values, but also on the exhibited trends. The correctness of a model can also be verified by showing the same trend observed in experiments despite of the inaccuracy of the specific values. For example, in Figure 4.20, the simulated value of drag force is not the same as that recorded in experiment, but the result shows the same trend that the drag force is reduced by the presence of the DBD and coexisting EHD flow.

There are different types of results that can be compared, such as the average value, the local value and the time-resolved results. In this thesis, the model of the DBD plasma actuator has been validated with more than 10 experimental papers, which are focused on different characteristics of the DBD actuator. An experiment can reveal a part of the characteristics of the studied phenomenon because it is always limited by the availability of experimental tools. A well-developed numerical model can be viewed as a tool that connects many experiments together and push forward the development of the theory.

6.3.5 Prediction

The benefits of a validated numerical model lie in its ability of prediction. The numerical model can reveal some results that might never be seen or detected in any experiments. For example, the DBD model presents the variation of surface charge density versus time, which is impossible to be recorded in experiments. These results could bring a valuable insight into the physics of the discharge and some new ideas of how to improve the performance of a DBD actuator.

In addition, the results of a numerical model can be vividly presented. It is very common to produce animation to show the simulated results such as the process of plasma discharge. All the data at any instant of time and any spatial location can be easily accessed and presented in the numerical solution. This abundance of data allows more accurate prediction of some characteristics such as the drag force.

6.4 Future Study

6.4.1 Corona Discharge for Drying

The drying mechanism can be developed further in a future model. As shown before, the model-predicted airflow mass flux is proportional to the drying rate recorded in the experiment. It is still not a direct agreement between simulation and experiment. A layer of water in the porous material should be introduced to the future model. It can also include other factors possibly affecting the drying in addition the airflow, such as heat, disturbance of ions, external flow and others. The new model should be able to calculate the drying rate with the presence of humidity in the model. In addition, the contributions of different factors and their relationship can be further examined and explained.

The efficiency of the EHD dryer could be examined. The previous work shows that the efficiency of electromechanical energy conversion is quite low. In order to find out whether the EHD dryer is efficient compared to a conventional air drying system, we can analyze the energy consumed by the EHD dryer and by the air drying system under the same drying rate. It would provide very convincing evidence to prove the advantage/disadvantage of the EHD dryer, which would cover a deficiency in previous researches.

In addition, the production of ozone should be taken into consideration especially for the industrial design of the EHD dryer. Corona discharge produces ozone that can oxidize the organic material in the environment. If the EHD dryer is going to be applied in the preservation of food, the presence of ozone should be carefully studied in the future model.

6.4.2 DBD Plasma Actuator

The electrons and the reactions of some species can be included in the future models. In the present model, only the positive and negative ions are included and all reactions are neglected. Therefore, the asymmetric properties of DBD are not revealed, and that is also the reason of the absence of streamer discharges and Trichel pulses in the simulation results. Although the present model is deemed sufficient for industrial applications, a more advanced model with three species would be better to understand the physical mechanisms of DBD. Moreover, in order to model the streamer discharges, the photoemission needs to be included. However, this might be beyond the state-of-art computing capability.

A parametric study of the geometric configurations could be done to optimize the design of the DBD actuator. Although the effects of voltage and frequency on the EHD flow have been investigated, the geometry of the DBD device can be optimized including the radius and length of the electrodes, the gap between electrodes and the thickness of the dielectric plate.

In practical applications, such as in aerodynamics, the environment might be very different from that in the laboratory. For example, the performance of the DBD actuator will be different when it is to be used on the wings of airplane where the pressure is very low. Therefore, the investigation of the low-pressure performance could be done in the future. In addition, according to the literature, the plasma discharge on the plane wings can absorb electromagnetic waves and makes the plane invisible on the radar [134-136]. A new study could be done in this field to enhance the understanding of the potential of DBD actuators.

6.4.3 Extended DBD

The study of the extended DBD in this thesis is only preliminary. More mechanisms could be added to the model, such as the existence of electrons, the surface charge drift and the micro

discharges on the dielectric surface. These features would make the simulation results closer to reality.

In one model, there is an angle between the EHD flow generated by the extended DBD and the dielectric wall. The angle can be adjusted by changing the value of DC voltage on the third electrode. This phenomenon might have the potential to be used for sweeping, coating or material separation.

6.4.4 Enhancing of the EHD flow

The velocity of the EHD flow limits the applications of plasma discharges, especially in aerodynamics. Many methods have been proposed to enhance the EHD flow, such as using multiple-electrode arrangements, arranging DBD actuators in series and optimizing the voltage waveform. The former two methods try to sequentially accelerate the airflow by using multiple electrodes. The general idea behind optimizing the voltage waveform is to strengthen the asymmetric properties of DBD in the positive phase and the negative phase, and then reduce the energy consumed by the fluctuation of air molecules in the transition between two phases. Results show that the EHD flows are still limited to a few m/s, which are far away from the requirements of the practical applications. However, considering the velocity of ionic particles and mass flow can reach 400 km/s in the solar wind, there is room to improve the EHD flow velocity, but probably with another technology.

References

- [1] J. R. Perkins, "Some general remarks on corona discharges," in *Engineering Dielectrics Volume I Corona Measurement and Interpretation*. ASTM International, pp. 3-20, **1979**
- [2] V. Hippel and R. Arthur, "Dielectrics and waves," *Journal of The Electrochemical Society* 102, vol.3, pp.68C-68C, **1954**.
- [3] T. W. Dakin and J. Lim, "Corona measurement and interpretation," *Transactions of the American Institute of Electrical Engineers. Part III: Power Apparatus and Systems*, vol. 76, pp. 1059-1065, **1957**.
- [4] V. Nikonov, R. Bartnikas and M. R. Wertheimer, "Surface charge and photoionization effects in short air gaps undergoing discharges at atmospheric pressure," *Journal of Physics D: Applied Physics*, vol. 34, p. 2979, **2001**.
- [5] J. M. Meek and J. D. Craggs, "Electrical breakdown of gases," **1978**.
- [6] H. Raether, "Surface plasmons on smooth surfaces," in *Surface plasmons on smooth and rough surfaces and on gratings*: Springer, pp. 4-39, **1988**.
- [7] J. C. Devins, "Current pulse shapes of discharges in air gaps limited by series dielectrics," in *Electrical Insulation, 1957 Conference*. IEEE, pp. 6-11, **1957**.
- [8] J. H. Mason, "The deterioration and breakdown of dielectrics resulting from internal discharges," *Proceedings of the IEE-Part I: General*, vol. 98, pp. 44-59, **1951**.
- [9] E. Friedlander and J. R. Reed, "Electric discharges in air-gaps facing solid insulation in high-voltage equipment," *Proceedings of the IEE-Part IIA: Insulating Materials*, vol. 100, pp. 121-131, **1953**.
- [10] T. Abe, Y. Takizawa, S. Sato, and N. Kimura, "A parametric experimental study for momentum transfer by plasma actuator," *AIAA paper*, vol. 187, p. 2007, **2007**.
- [11] R. Van Dyken, T. E. McLaughlin and C. L. Enloe, "Parametric investigations of a single dielectric barrier plasma actuator," *AIAA paper*, vol. 846, p. 2004, **2004**.
- [12] A. M. Thomas, "'Heat developed" and "powder" Lichtenberg figures and the ionization of dielectric surfaces produced by electrical impulses," *British Journal of Applied Physics*, vol. 2, p. 98, **1951**.
- [13] N. Benard and E. Moreau, "Electrical and mechanical characteristics of surface AC dielectric barrier discharge plasma actuators applied to airflow control," *Experiments in Fluids*, vol. 55, p. 1846, **2014**.
- [14] S. Guo, T. Simon, D. Ernie, and U. Kortshagen, "Separation control using DBD plasma actuators: thrust enhancement studies," in *48th AIAA Aerospace Sciences Meeting*, vol. 1090, **2010**.
- [15] A. S. Mujumdar, "*Handbook of industrial drying*: CRC press", **2014**.
- [16] C. Bonazzi and E. Dumoulin, "Quality changes in food materials as influenced by drying processes," *Modern Drying Technology, Volume 3: Product Quality and Formulation*, pp. 1-20, **2011**.
- [17] P. Talbot, M. Lhote, C. Heilporn, A. Schubert, F. Willaert, and B. Haut, "Ventilated tunnel solar dryers for small-scale farmers communities: Theoretical and practical aspects," *Drying Technology*, vol. 34, pp. 1162-1174, **2016**.
- [18] J. Chang, A. J. Kelly and J. M. Crowley, *Handbook of electrostatic processes*: CRC Press, **1995**.
- [19] A. A. Alemrajabi, F. Rezaee, M. Mirhosseini, and A. Esehaghbeygi, "Comparative evaluation of the effects of electrohydrodynamic, oven, and ambient air on carrot cylindrical slices during drying process," *Drying Technology*, vol. 30, pp. 88-96, **2012**.
- [20] T. R. Bajgai and F. Hashinaga, "High electric field drying of Japanese radish," *Drying Technology*, vol. 19, pp. 2291-2302, **2001**.
- [21] A. Esehaghbeygi and M. Basiry, "Electrohydrodynamic (EHD) drying of tomato slices (*Lycopersicon esculentum*)," *Journal of Food Engineering*, vol. 104, pp. 628-631, **2011**.
- [22] M. Yang and C. Ding, "Electrohydrodynamic (EHD) drying of the Chinese wolfberry fruits," *SpringerPlus*, vol. 5, p. 909, **2016**.
- [23] A. Wolny and R. Kaniuk, "The effect of electric field on heat and mass transfer," *Drying technology*, vol. 14, pp. 195-216, **1996**.
- [24] M. R. Ramachandran and F. C. Lai, "Effects of porosity on the performance of EHD-enhanced drying," *Drying Technology*, vol. 28, pp. 1477-1483, **2010**.
- [25] F. Hashinaga, T. R. Bajgai, S. Isobe, and N. N. Barthakur, "Electrohydrodynamic (EHD) drying of apple slices," *Drying Technology*, vol. 17, pp. 479-495, **1999**.
- [26] A. Esehaghbeygi and M. Basiry, "Electrohydrodynamic (EHD) drying of tomato slices (*Lycopersicon esculentum*)," *Journal of Food Engineering*, vol. 104, pp. 628-631, **2011**.

- [27] M. Pogorzelski, Z. Zander, L. Zander, and M. Wrotniak, "Drying kinetics of plant material using the electrohydrodynamic (EHD) method," *Chemical Engineering and Equipment*, vol. 44, pp. 552-553, **2013**.
- [28] J. Filkenstein-Cukier, "On discharge from pointed rods," *Annalen der Physik*, vol. 376, pp. 509-536, **1923**.
- [29] J. Precht, "Absolute measurements of electric discharge from pointed rods," *Annalen der Physik*, vol. 285, pp. 150-183, **1893**.
- [30] E. Warburg, "Ueber das Verhalten sogenannter unpolarisierbarer Elektroden gegen Wechselstrom," *Annalen der Physik*, vol. 303, pp. 493-499, **1899**.
- [31] M. J. Dalvand, S. S. Mohtasebi and S. Rafiee, "Effect of needle number on drying rate of kiwi fruit in EHD drying process," *Agricultural Sciences*, vol. 4, p. 1, **2013**.
- [32] F. C. Lai and R. K. Sharma, "EHD-enhanced drying with multiple needle electrode," *Journal of Electrostatics*, vol. 63, pp. 223-237, **2005**.
- [33] T. Kudra and A. Martynenko, "Energy aspects in electrohydrodynamic drying," *Drying technology*, vol. 33, pp. 1534-1540, **2015**.
- [34] Y. X. Bai and B. Sun, "Study of electrohydrodynamic (EHD) drying technique for shrimps," *Journal of Food Processing and Preservation*, vol. 35, pp. 891-897, **2011**.
- [35] C. Strumillo and T. Kudra, "Drying: principles, science and design," *Gordon and Breach Science Publishers, New York*, vol. 42, **1986**.
- [36] F. C. Lai and K. Lai, "EHD-enhanced drying with wire electrode," *Drying technology*, vol. 20, pp. 1393-1405, **2002**.
- [37] F. C. Lai and D. S. Wong, "EHD-enhanced drying with needle electrode," *Drying Technology*, vol. 21, pp. 1291-1306, **2003**.
- [38] S. T. Dinani, N. Hamdami, M. Shahedi, and M. Havet, "Mathematical modeling of hot air/electrohydrodynamic (EHD) drying kinetics of mushroom slices," *Energy Conversion and Management*, vol. 86, pp. 70-80, **2014**.
- [39] A. S. Mujumdar and S. Devahastin, "Fluidized bed drying technology", Exergex Corporation Montreal,, Canada, p. pp-75, **2000**.
- [40] Y. Su, M. Zhang and A. S. Mujumdar, "Recent developments in smart drying technology," *Drying Technology*, vol. 33, pp. 260-276, **2015**.
- [41] A. Martynenko and W. Zheng, "Electrohydrodynamic drying of apple slices: energy and quality aspects," *Journal of Food Engineering*, vol. 168, pp. 215-222, **2016**.
- [42] M. Goldman, A. Goldman and R. S. Sigmond, "The corona discharge, its properties and specific uses," *Pure and Applied Chemistry*, vol. 57, pp. 1353-1362, **1985**.
- [43] A. Martynenko, T. Kudra and J. Yue, "Multi-Pin EHD Dryer: Effect of Electrode Geometry on Charge and Mass Transfer," *Drying Technology*, vol. 35 (16), pp. 1970-1980, **2017**.
- [44] Y. Chen, N. N. Barthakur and N. P. Arnold, "Electrohydrodynamic (EHD) drying of potato slabs," *Journal of Food Engineering*, vol. 23, pp. 107-119, **1994**.
- [45] F. HASHINAGA, G. P. KHAREL and R. SHINTANI, "Effect of ordinary frequency high electric fields on evaporation and drying," *Food Science and Technology International, Tokyo*, vol. 1, pp. 77-81, **1995**.
- [46] O. E. Ramadan and S. L. Soo, "Electrohydrodynamic secondary flow," *The Physics of Fluids*, vol. 12, pp. 1943-1945, **1969**.
- [47] A. Yabe, Y. Mori and K. Hijikata, "EHD study of the corona wind between wire and plate electrodes," *AIAA journal*, vol. 16, pp. 340-345, **1978**.
- [48] W. Egli, U. Kogelschatz, E. A. Gerteisen, and R. Gruber, "3D computation of corona, ion induced secondary flows and particle motion in technical ESP configurations," *Journal of electrostatics*, vol. 40, pp. 425-430, **1997**.
- [49] G. A. Kallio and D. E. Stock, "Interaction of electrostatic and fluid dynamic fields in wire — plate electrostatic precipitators," *Journal of Fluid Mechanics*, vol. 240, pp. 133-166, **1992**.
- [50] T. Yamamoto and H. R. Velkoff, "Electrohydrodynamics in an electrostatic precipitator," *Journal of Fluid Mechanics*, vol. 108, pp. 1-18, **1981**.
- [51] L. Zhao and K. Adamiak, "Numerical simulation of the electrohydrodynamic flow in a single wire-plate electrostatic precipitator," *IEEE Transactions on Industry applications*, vol. 44, pp. 683-691, **2008**.
- [52] F. Cotton, C. Berge, F. Lemeille, A. Pitarka, B. Lebrun, and M. Vallon, "Three-dimensional simulation of earthquakes in the Grenoble' s basin," *The Effects of Surface Geology on Seismic Motion*, vol. 2, pp. 873-878, **1998**.
- [53] J. S. Cotton, D. Brocilo, J. Chang, M. Shoukri, and T. Smith-Pollard, "Numerical simulation of electric field distributions in electrohydrodynamic two-phase flow regimes," *IEEE transactions on dielectrics and electrical insulation*, vol. 10, pp. 37-51, **2003**.

- [54] P. Béquin, K. Castor and J. Scholten, "Electric wind characterisation in negative point-to-plane corona discharges in air," *The European Physical Journal-Applied Physics*, vol. 22, pp. 41-49, **2003**.
- [55] G. A. Kallio and D. E. Stock, "Flow visualization inside a wire-plate electrostatic precipitator," *IEEE transactions on industry applications*, vol. 26, pp. 503-514, **1990**.
- [56] T. Makita, R. Ohyama and M. Fukumoto, "A computerized visualization of gas-phase EHD flow field for needle-plane electrodes system", *Electrical Insulation and Dielectric Phenomena, Annual Report Conference on IEEE*, pp. 192-195, **2002**.
- [57] N. Kasayananand and T. Kiatsiriroat, "EHD enhanced heat transfer in wavy channel," *International communications in heat and mass transfer*, vol. 32, pp. 809-821, **2005**.
- [58] O. Rouaud and M. Havet, "Assessment of the electrohydrodynamic drying process," *Food and Bioprocess Technology*, vol. 2, pp. 240-247, **2009**.
- [59] F. X. Hart and J. S. Massey, "Ion wind enhancement of evaporation into a laminar air stream," *International Journal of Heat and Mass Transfer*, vol. 23, pp. 363-371, **1980**.
- [60] S. R. Mahmoudi, K. Adamiak and G. Castle, "Electrohydrodynamic single-phase convection heat transfer enhancement techniques: Direct ionic wind and vortex induction," *Proc. of ESA Annual Meeting*, pp. 1-13, **2011**.
- [61] M. Huang and F. C. Lai, "Numerical study of EHD-enhanced water evaporation," *Journal of Electrostatics*, vol. 68, pp. 364-370, **2010**.
- [62] L. Zhao and K. Adamiak, "EHD flow in air produced by electric corona discharge in pin - plate configuration," *Journal of electrostatics*, vol. 63, pp. 337-350, **2005**.
- [63] M. Belan and F. Messanelli, "Compared ionic wind measurements on multi-tip corona and DBD plasma actuators," *Journal of Electrostatics*, vol. 76, pp. 278-287, **2015**.
- [64] J. P. Boeuf, Y. Lagmich, T. Unfer, T. Callegari, and L. C. Pitchford, "Electrohydrodynamic force in dielectric barrier discharge plasma actuators," *Journal of Physics D: Applied Physics*, vol. 40, p. 652, **2007**.
- [65] R. Valdivia-Barrientos, J. Pacheco-Sotelo, M. Pacheco-Pacheco, J. S. Benítez-Read, and R. López-Callejas, "Analysis and electrical modelling of a cylindrical DBD configuration at different operating frequencies," *Plasma sources science and technology*, vol. 15, p. 237, **2006**.
- [66] N. Jiang, A. Ji and Z. Cao, "Atmospheric pressure plasma jet: Effect of electrode configuration, discharge behavior, and its formation mechanism," *Journal of Applied Physics*, vol. 106, p. 013308, **2009**.
- [67] K. G. Kostov, R. Y. Honda, L. Alves, and M. E. Kayama, "Characteristics of dielectric barrier discharge reactor for material treatment," *Brazilian Journal of Physics*, vol. 39, pp. 322-325, **2009**.
- [68] A. Debien, N. Benard and E. Moreau, "Streamer inhibition for improving force and electric wind produced by DBD actuators," *Journal of Physics D: Applied Physics*, vol. 45, p. 215201, **2012**.
- [69] C. Borghi, A. Cristofolini, G. Neretti, and F. Roveda, "Experimental and Numerical Investigation on a DBD Actuator for Airflow Control," in *42nd AIAA Plasmadynamics and Lasers Conference in conjunction with the 18th International Conference on MHD Energy Conversion (ICMHD)*, p. 3912, **2011**.
- [70] G. Moreau and C. J. Lucarotti, "A brief review of the past use of baculoviruses for the management of eruptive forest defoliators and recent developments on a sawfly virus in Canada," *The Forestry Chronicle*, vol. 83, pp. 105-112, **2007**.
- [71] N. Benard and E. Moreau, "Role of the electric waveform supplying a dielectric barrier discharge plasma actuator," *Applied Physics Letters*, vol. 100, p. 193503, **2012**.
- [72] J. Pons, E. Moreau and G. Touchard, "Electrical and aerodynamic characteristics of atmospheric pressure barrier discharges in ambient air," pp. 307-310, **2004**.
- [73] M. Forte, J. Jolibois, J. Pons, E. Moreau, G. Touchard, and M. Cazalens, "Optimization of a dielectric barrier discharge actuator by stationary and non-stationary measurements of the induced flow velocity: application to airflow control," *Experiments in Fluids*, vol. 43, pp. 917-928, **2007**.
- [74] Roth, J. R., Dai, X., Rahel, J., & Sherman, D., "The physics and phenomenology of paraelectric one atmosphere uniform glow discharge plasma (OAUGDP™) actuators for aerodynamic flow control," in *43rd AIAA Aerospace Sciences Meeting and Exhibit*, p. 781, **2005**.
- [75] R. J. Dai X, "Optimization of the aerodynamic plasma actuator as an EHD electrical device," in *44th AIAA Aerospace Sciences Meeting and Exhibit*, p.1203, **2006**.
- [76] J. Jolibois and E. Moreau, "Enhancement of the electromechanical performances of a single dielectric barrier discharge actuator," *IEEE Transactions on Dielectrics and Electrical Insulation*, vol. 16, pp. 758-767, **2009**.
- [77] N. Balcon, N. Benard and E. Moreau, "Formation process of the electric wind produced by a plasma actuator," *IEEE Transactions on Dielectrics and Electrical Insulation*, vol. 16, pp. 463-469, **2009**.
- [78] M. Forte, J. Jolibois, E. Moreau, and G. Touchard, "Optimization of a Dielectric Barrier Discharge actuator application to airflow control," *Experiments in Fluids*, vol. 43(6), pp. 917-928, **2006**.

- [79] N. Benard, A. Debien and E. Moreau, "Time-dependent volume force produced by a non-thermal plasma actuator from experimental velocity field," *Journal of Physics D: Applied Physics*, vol. 46, p. 245201, **2013**.
- [80] C. L. Enloe, M. G. McHarg, G. I. Font, and T. E. McLaughlin, "Plasma-induced force and self-induced drag in the dielectric barrier discharge aerodynamic plasma actuator," in *47th AIAA Aerospace Sciences Meeting including The New Horizons Forum and Aerospace Exposition*, p. 1622, **2009**.
- [81] J. Kriegseis, C. Schwarz, A. Duchmann, S. Grundmann, and C. Tropea, "PIV-based estimation of DBD plasma-actuator force terms," in *50th AIAA Aerospace Sciences Meeting including the New Horizons Forum and Aerospace Exposition*, p. 411, **2012**.
- [82] I. V. Adamovich, J. Little, M. Nishihara, K. Takashima, and M. Samimy, "Nanosecond pulse surface discharges for high-speed flow control," in *6th AIAA Flow Control Conference*, p. 3137, **2012**.
- [83] B. Eliasson and U. Kogelschatz, "Nonequilibrium volume plasma chemical processing," *IEEE transactions on plasma science*, vol. 19, pp. 1063-1077, **1991**.
- [84] T. Unfer and J. P. Boeuf, "Modelling of a nanosecond surface discharge actuator," *Applied Physics*, vol. 42, p. 194017, **2009**.
- [85] A. V. Likhanskii, M. N. Shneider, S. O. Macheret, and R. B. Miles, "Modeling of dielectric barrier discharge plasma actuator in air," *Journal of Applied Physics*, vol. 103, p. 053305, **2008**.
- [86] H. Nishida and T. Abe, "Validation study of numerical simulation of discharge plasma on DBD plasma actuator," in *42nd AIAA Plasmadynamics and Lasers Conference in conjunction with the 18th International Conference on MHD Energy Conversion (ICMHD)*, p. 3913, **2011**.
- [87] J. Teunissen, A. Sun and U. Ebert, "A time scale for electrical screening in pulsed gas discharges," *Journal of Physics D: Applied Physics*, vol. 47, p. 365203, **2014**.
- [88] A. Sun, C. Huo and J. Zhuang, "Formation mechanism of streamer discharges in liquids: a review," *High Voltage*, vol. 1, pp. 74-80, **2016**.
- [89] P. Dordzadeh, K. Adamiak and G. P. Castle, "Parametric study of the characteristics of Trichel pulses in the needle-plane negative corona discharge in atmospheric air," *Journal of Electrostatics*, vol. 84, pp. 73-80, **2016**.
- [90] J. S. Shang and P. G. Huang, "Modeling of ac dielectric barrier discharge," *Journal of Applied Physics*, vol. 107, p. 113302, **2010**.
- [91] S. Roy and D. V. Gaitonde, "Modeling surface discharge effects of atmospheric RF on gas flow control," in *43rd AIAA Aerospace Sciences Meeting and Exhibit*, p. 160, **2005**.
- [92] J. P. Boeuf and L. C. Pitchford, "Electrohydrodynamic force and aerodynamic flow acceleration in surface dielectric barrier discharge," *Journal of Applied Physics*, vol. 97, p. 103307, **2005**.
- [93] D. M. Orlov and T. C. Corke, "Numerical simulation of aerodynamic plasma actuator effects," in *43rd AIAA Aerospace Sciences Meeting and Exhibit*, p. 1083, **2005**.
- [94] S. Roy, "Flow actuation using radio frequency in partially ionized collisional plasmas," *Applied Physics Letters*, vol. 86, p. 101502, **2005**.
- [95] M. Ghazanchaei, K. Adamiak and G. P. Castle, "Quasi-stationary numerical model of the dielectric barrier discharge," *Journal of Electrostatics*, vol. 72, pp. 261-269, **2014**.
- [96] Y. P. Raizer, "Gas discharge physics". Springer, New York 1991.
- [97] E. A. Bogdanov, A. A. Kudryavtsev, A. L. Kuranov, I. E. Kozlov, and T. L. Tkchenko, "2D Simulation of DBD plasma actuator in air," *AIAA*, p.1377, **2008**.
- [98] Y. B. Golubovskii, V. A. Maiorov, J. Behnke, and J. F. Behnke, "Modelling of the homogeneous barrier discharge in helium at atmospheric pressure," *Journal of Physics D: Applied Physics*, vol. 36, p. 39, **2002**.
- [99] S. Pancheshnyi, M. Nudnova and A. Starikovskii, "Development of a cathode-directed streamer discharge in air at different pressures: experiment and comparison with direct numerical simulation," *Physical Review E*, vol. 71, p. 016407, **2005**.
- [100] A. V. Likhanskii, V. V. Semak, M. N. Shneider, D. F. Opaitis, R. B. Miles, and S. O. Macheret, "The role of the photoionization in the numerical modeling of the DBD plasma actuator," in *47th AIAA Aerospace Sciences Meeting including The New Horizons Forum and Aerospace Exposition*, p. 841, **2009**.
- [101] B. Arad, Y. Gazit and A. Ludmirsky, "A sliding discharge device for producing cylindrical shock waves," *Journal of Physics D: Applied Physics*, vol. 20, p. 360, **1987**.
- [102] V. Y. Baranov, V. M. Borisov and O. B. Khristoforov, "Excimer electric-discharge laser with plasma electrodes," *Soviet Journal of Quantum Electronics*, vol. 11, p. 93, **1981**.
- [103] G. N. Tsirikas and A. A. Serafetinides, "The effect of voltage pulse polarity on the performance of a sliding discharge pumped HF laser," *Journal of Physics D: Applied Physics*, vol. 29, p. 2806, **1996**.

- [104] H. N. T. M. K. Nakai, "Effect of AC Voltage Waveform on Tri-Electrode Plasma Actuator Utilizing Interaction Between AC and DC Discharge," *proceedings of International Symposium on Electrohydrodynamics Ottawa*, **2017**.
- [105] H. Nishida, K. Nakai and T. Matsuno, "Physical Mechanism of Tri-Electrode Plasma Actuator with Direct-Current High Voltage," *AIAA Journal*, pp. 1-10, **2017**.
- [106] A. Debien, N. Benard and E. Moreau, "Electric wind produced by sliding discharges," *Proceeding of 2nd ISNPEDADM new electrical technologies for environment, Nouméa*, **2011**.
- [107] E. Moreau, C. Louste and G. Touchard, "Electric wind induced by sliding discharge in air at atmospheric pressure," *Journal of Electrostatics*, vol. 66, pp. 107-114, **2008**.
- [108] E. Moreau, R. Sosa and G. Artana, "Electric wind produced by surface plasma actuators: a new dielectric barrier discharge based on a three-electrode geometry," *Journal of Physics D: Applied Physics*, vol. 41, p. 115204, **2008**.
- [109] R. Sosa, E. Arnaud, E. Memin, and G. Artana, "Study of the flow induced by a sliding discharge," *IEEE Transactions on Dielectrics and Electrical Insulation*, vol. 16, p. 2, **2009**.
- [110] S. Huimin, L. Yinghong, Z. Qiaogen, J. Min, and W. Yun, "Experimental investigation on the characteristics of sliding discharge plasma aerodynamic actuation," *Plasma Science and Technology*, vol. 13, p. 608, **2011**.
- [111] S. Guo, D. Burman, D. Poon, M. Mamunuru, T. Simon, D. Ernie, and U. Kortshagen, "Separation control using DBD plasma actuators: designs for thrust enhancement," in *39th AIAA Fluid Dynamics Conference*, p. 4184, **2009**.
- [112] T. Matsuno, M. Sugahara, H. Kawazoe, and H. Nishida, "Development of Serrated Multi-Electrode Plasma Actuators for Enhanced Force Production," in *54th AIAA Aerospace Sciences Meeting*, p. 1691, **2016**.
- [113] J. P. Boeuf, Y. Lagmich and L. C. Pitchford, "Contribution of positive and negative ions to the electrohydrodynamic force in a dielectric barrier discharge plasma actuator operating in air," *Journal of applied physics*, vol. 106, p. 023115, **2009**.
- [114] K. Adamiak and P. Atten, "Simulation of corona discharge in point - plane configuration," *Journal of electrostatics*, vol. 61, pp. 85-98, **2004**.
- [115] N. Toljic, K. Adamiak, G. Castle, H. H. Kuo, and H. C. Fan, "A full 3D numerical model of the industrial electrostatic coating process for moving targets," *Journal of Electrostatics*, vol. 71, pp. 299-304, **2013**.
- [116] P. Sattari, G. P. Castle and K. Adamiak, "FEM - FCT-based dynamic simulation of corona discharge in point - plane configuration," *IEEE Transactions on Industry Applications*, vol. 46, pp. 1699-1706, **2010**.
- [117] K. Adamiak, V. Atrazhev and P. Atten, "Corona discharge in the hyperbolic point-plane configuration: direct ionization criterion versus an approximate formulations," *IEEE Transactions on dielectrics and electrical insulation*, vol. 12, pp. 1015-1024, **2005**.
- [118] C. H. Gary, J. P. SCHMITT and B. P. HUTZLER, "Peeks Law Generalization Application To Various Field Configurations," in *IEEE transactions on power apparatus and systems*, no. 6, p. 2262, **1972**.
- [119] L. Zhao and K. Adamiak, "EHD gas flow in electrostatic levitation unit," *Journal of electrostatics*, vol. 64, pp. 639-645, **2006**.
- [120] N. Sato, "Discharge current induced by the motion of charged particles," *Journal of Physics D: Applied Physics*, vol. 13, p. L3, **1980**.
- [121] J. Pons, E. Moreau and G. Touchard, "Asymmetric surface dielectric barrier discharge in air at atmospheric pressure: electrical properties and induced airflow characteristics," *Journal of physics D: applied physics*, vol. 38, p. 3635, **2005**.
- [122] C. L. Enloe, T. E. McLaughlin, R. D. VanDyken, K. D. Kachner, E. J. Jumper, and T. C. Corke, "Mechanisms and responses of a single dielectric barrier plasma actuator: plasma morphology," *AIAA journal*, vol. 42, pp. 589-594, **2004**.
- [123] C. L. Enloe, T. E. McLaughlin, R. D. VanDyken, K. D. Kachner, E. J. Jumper, T. C. Corke, M. Post, and O. Haddad, "Mechanisms and responses of a single dielectric barrier plasma actuator: geometric effects," *AIAA journal*, vol. 42, pp. 595-604, **2004**.
- [124] P. F. Kurunczi, "Atmospheric pressure non-thermal plasma device to clean and sterilize the surfaces of probes, cannulas, pin tools, pipettes and spray heads," U.S. Patent No. 7,094,314, **2006**.
- [125] A. V. Likhanskii, M. N. Shneider, S. O. Macheret, and R. B. Miles, "Modeling of interaction between weakly ionized near-surface plasmas and gas flow," in *44th AIAA Aerospace Sciences Meeting and Exhibit*, p. 1204, **2006**.
- [126] E. Moreau, "Airflow control by non-thermal plasma actuators," *Journal of physics D: applied physics*, vol. 40, p. 605, **2007**.

- [127] A. Nakano and H. Nishida, "Basic Study on the Voltage Characteristic of Dual-Grounded Tri - Electrode Plasma Actuator by Plasma Simulation," in *47th AIAA Plasmadynamics and Lasers Conference*, p. 4014, **2016**.
- [128] N. Monrolin, F. Plouraboué and O. Praud, "Electrohydrodynamic Thrust for In-Atmosphere Propulsion," *AIAA Journal*, pp. 1-10, **2017**.
- [129] X. Lu, M. Laroussi and V. Puech, "On atmospheric-pressure non-equilibrium plasma jets and plasma bullets," *Plasma Sources Science and Technology*, vol. 21, p. 034005, **2012**.
- [130] F. Soetomo, G. M. Colver and K. Fourraghi, "Micro-force measurement of drag on a small flat plate in the presence of a corona discharge," *Journal of electrostatics*, vol. 64, pp. 525-530, **2006**.
- [131] E. Moreau and G. Touchard, "About the kinetic power induced by AC and DC discharges," in *Electrical Insulation and Dielectric Phenomena, 2005. CEIDP'05. 2005 Annual Report Conference on*. IEEE, pp. 469-473, **2005**.
- [132] A. Santhanakrishnan and J. D. Jacob, "Flow control with plasma synthetic jet actuators," *Journal of Physics D: Applied Physics*, vol. 40, p. 637, **2007**.
- [133] C. Porter, A. Abbas, K. Cohen, T. McLaughlin, and C. L. Enloe, "Spatially distributed forcing and jet vectoring with a plasma actuator," *AIAA J*, vol. 47, pp. 1368-1378, **2009**.
- [134] L. Chaohui, H. Xiwei and J. Zhonghe, "Interaction of electromagnetic waves with two-dimensional metal covered with radar absorbing material and plasma," *Plasma Science and Technology*, vol. 10, p. 717, **2008**.
- [135] B. Chaudhury and S. Chaturvedi, "Study and optimization of plasma-based radar cross section reduction using three-dimensional computations," *IEEE Transactions on Plasma Science*, vol. 37, pp. 2116-2127, **2009**.
- [136] C. Yuan, Z. Zhou, J. W. Zhang, X. Xiang, Y. Feng, and H. Sun, "Properties of propagation of electromagnetic wave in a multilayer radar-absorbing structure with plasma-and radar-absorbing material," *IEEE Transactions on Plasma Science*, vol. 39, pp. 1768-1775, **2011**.

Appendices

The details of all numerical models investigated in this thesis have been demonstrated here including the physics equations, boundary conditions, discretization, solvers and so on.

1. EHD Dryer

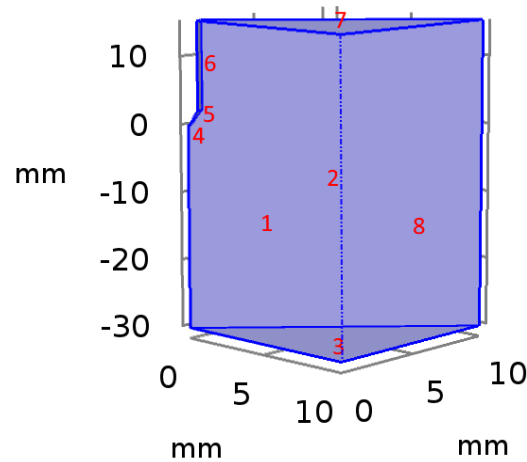


Figure A. 1 The calculation domain of the EHD dryer model.

The EHD dryer model is investigated in the one and only one domain. Given the symmetry of the geometry of pin matrix, only a triangular prism zone of a single pin electrode was analyzed, which has eight surface boundaries labeled in Figure A.1. The boundaries 1, 2, 8 are the left, back and right surface, respectively. The boundary 3 and 7 denotes the grounded electrode and top plate, respectively. The boundaries 4, 5, 6 correspond to three parts of a single pin electrode that is composed of a cylinder, cone and sphere.

Table 2: Physics and equations in the EHD dryer model

Physics	Poissonian electric field	Laplacian electric field	Charge transport	Laminar flow
Equations	$\nabla \cdot \mathbf{D} = \rho_v$ $\mathbf{E} = -\nabla V$	$\nabla \cdot \mathbf{D} = \rho_v$ $= 0$ $\mathbf{E} = -\nabla V$	$\nabla \cdot (-D_i \nabla c_i - z_i \mu_{m,i} F c_i \nabla V) = R_i$ $\mathbf{N}_i = -D_i \nabla c_i - z_i \mu_{m,i} F c_i \nabla V$	$\rho(\mathbf{u} \cdot \nabla) \mathbf{u} =$ $\nabla \cdot [-p \mathbf{I} + \mu(\nabla \mathbf{u} + (\nabla \mathbf{u})^T)] + \mathbf{F}$ $\rho \nabla \cdot (\mathbf{u}) = 0$ $\mathbf{F} = \rho_v \cdot \mathbf{E}_p$

Initial value	$V=0$	$V=0$	$\rho_v=0$	$P = 0$ (relative) $u = 0$
Features	E_P V_P Poissonian Electric field & Potential	E_L V_L Laplacian Electric field & Potential	ρ_v Space charge density	P u Pressure & Velocity

This numerical model takes 4 physical processes into consideration. They are coupled with each other and solved together.

Table 3 Boundary conditions in EHD dryer model

Boundaries	Poissonian electric field	Laplacian electric field	Charge transport	Laminar flow
1	$\mathbf{n} \cdot \mathbf{D} = 0$ Zero charge	$\mathbf{n} \cdot \mathbf{D} = 0$ Zero charge	$-\mathbf{n} \cdot \mathbf{N}_i = 0$ No flux	$\mathbf{u} \cdot \mathbf{n} = 0$ $\kappa \cdot (\kappa \cdot \mathbf{n}) \mathbf{n} = 0$, $\kappa = [\mu(\nabla \mathbf{u} + (\nabla \mathbf{u})^T)] \mathbf{n}$ Symmetry
2	$\mathbf{n} \cdot \mathbf{D} = 0$ Zero charge	$\mathbf{n} \cdot \mathbf{D} = 0$ Zero charge	$-\mathbf{n} \cdot \mathbf{N}_i = 0$ No flux	$\mathbf{u} \cdot \mathbf{n} = 0$ $\kappa \cdot (\kappa \cdot \mathbf{n}) \mathbf{n} = 0$, $\kappa = [\mu(\nabla \mathbf{u} + (\nabla \mathbf{u})^T)] \mathbf{n}$ Symmetry
3	$V = 0$ Ground	$V = 0$ Ground	$-\mathbf{n} \cdot D_i \nabla c_i = 0$ Outflow	$\mathbf{u} = 0$ No slip wall
4	$V = V_0$ Electric Potential	$V = V_0$ Electric Potential	$c_i = c_{0j}$ Concentration	$\mathbf{u} = 0$ No slip wall
5	$V = V_0$ Electric Potential	$V = V_0$ Electric Potential	$-\mathbf{n} \cdot \mathbf{N}_i = 0$ No flux	$\mathbf{u} = 0$ No slip wall
6	$V = V_0$ Electric Potential	$V = V_0$ Electric Potential	$-\mathbf{n} \cdot \mathbf{N}_i = 0$ No flux	$\mathbf{u} = 0$ No slip wall
7	$V = V_0$ Electric Potential	$V = V_0$ Electric Potential	$-\mathbf{n} \cdot \mathbf{N}_i = 0$ No flux	$\mathbf{u} = 0$ No slip wall
8	$\mathbf{n} \cdot \mathbf{D} = 0$ Zero charge	$\mathbf{n} \cdot \mathbf{D} = 0$ Zero charge	$-\mathbf{n} \cdot \mathbf{N}_i = 0$ No flux	$\mathbf{u} \cdot \mathbf{n} = 0$ $\kappa \cdot (\kappa \cdot \mathbf{n}) \mathbf{n} = 0$, $\kappa = [\mu(\nabla \mathbf{u} + (\nabla \mathbf{u})^T)] \mathbf{n}$

The boundary conditions in different physical models are summarized in Table 3. Please note that the value of C_i in the “concentration” boundary condition of charge transport is determined by a MATLAB routine, where the Peek’s formula and Kaptzov’s hypothesis are adopted.

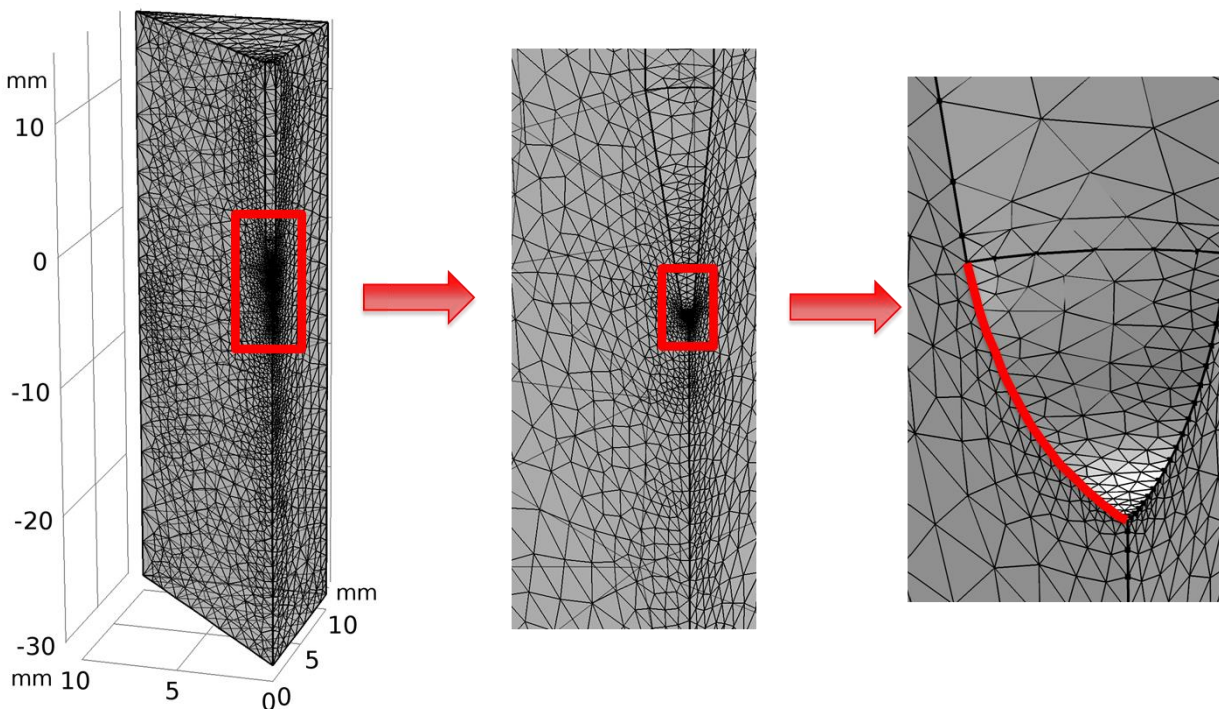


Figure A. 2 Mesh of an example model

Figure A.2 shows the mesh of the model with pin spacing of 2×2 cm and electrode gap of 3 cm. In this case, the whole domain was discretized into 25,107 tetrahedral elements and the average element quality is 0.858. The mesh is extremely fine on the electrode tip where the curve with the radius of 0.1 mm was discretized into 20 elements. The finer the mesh is, the more accurate the results would be. A mesh independence study could be done to improve the mesh of the model. The model can be simulated with a stationary solver. A direct solver named MUMPS is used in this model. It takes approximately 20 minutes for the simulation of one case.

2. DBD Actuator

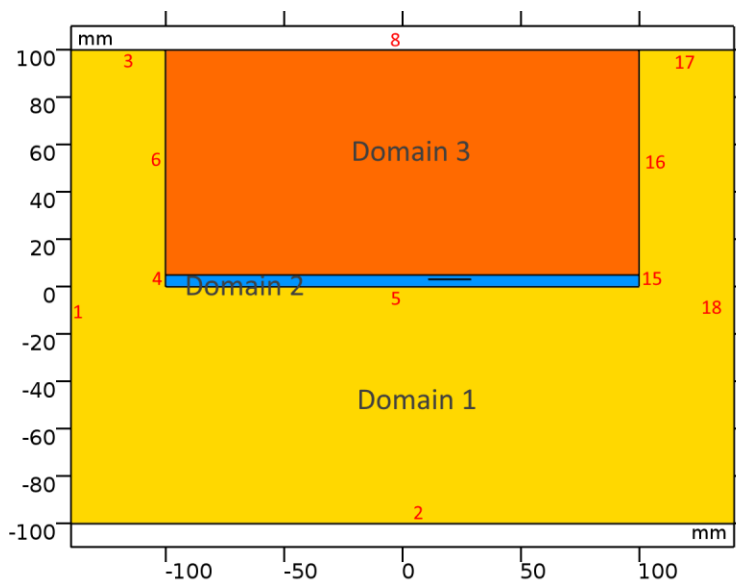


Figure A. 3 Calculation domain of the DBD actuator model.

The DBD actuator model consists of three computation domain as shown in Figure A.3. The domains 1 and 3 are air and domain 2 is the dielectric plate. This 2D model has 26 boundaries and some of them are marked red above. The rest are marked in a zoomed view of the electrodes and the dielectric plate. Please note the boundary 10 is the down boundary of the interface of domains 2 and 3, while 11 denotes the upper boundary. The boundary 9 is the middle line between boundaries 10 and 11. It is an auxiliary line to build up the model, and has no physical meaning. In addition, the tip of electrodes is a half circle. Each of them is made of two boundaries whose number ranges from 19 to 26.

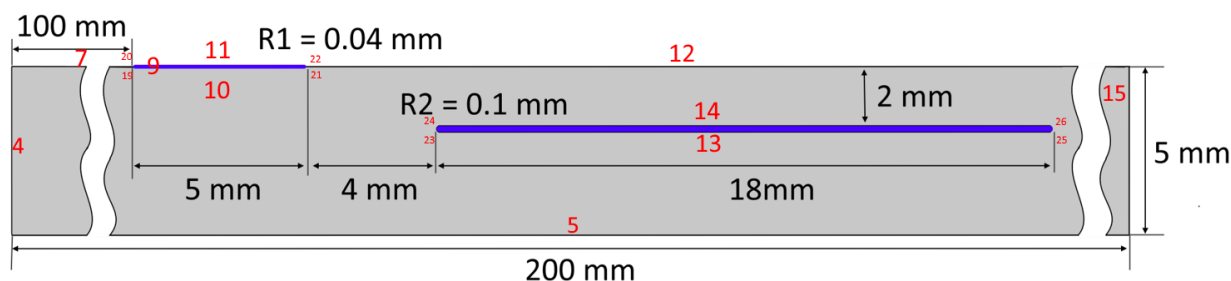


Figure A. 4 Zoomed view of the DBD actuator

Different from the EHD dryer model, the DBD actuator model is a two-species model (positive and negative ions). It also considers the surface charge accumulated on the dielectric surface. In addition, the physical fields in this model change periodically with respect to the AC voltage. So the model is much more complicated than the EHD dryer model. The Table 4 presents the physics

and equations involved in the DBD actuator. Although the Laplacian electric field is calculated, it is not included in the table because it is very similar to the Poissonian electric field.

Table 4 Physics and equations in the DBD actuator model

Physics	Poissonian electric field	Charge transport	Surface charge	Laminar flow
Equations	$\nabla \cdot \mathbf{D} = \rho_v$ $\mathbf{E} = -\nabla V$	$\nabla \cdot (-D_i \nabla c_i - z_i u_{m,i} F c_i \nabla V) = R_i$ $\mathbf{N}_i = -D_i \nabla c_i - z_i u_{m,i} F c_i \nabla V$	$\frac{\partial \rho_s}{\partial t} = \mathbf{n} \cdot \mathbf{J}_i + \mathbf{n} \cdot \mathbf{J}_e$ $-\mathbf{n} \cdot (\mathbf{D}_1 - \mathbf{D}_2) = \rho_s$	$\rho(\mathbf{u} \cdot \nabla) \mathbf{u} =$ $\nabla \cdot [-\rho \mathbf{I} + \mu(\nabla \mathbf{u} + (\nabla \mathbf{u})^T)] + \mathbf{F}$ $\rho \nabla \cdot (\mathbf{u}) = 0$ $\mathbf{F} = \rho_v \cdot \mathbf{E}_p$
Initial value	$V=0$	$\rho_v=0$	$\rho_s=0$	$P = 0$ (relative) $\mathbf{u} = 0$
Domains	1, 2, 3	1, 3	Interface between 2 & 3	3
Features	E_p V_p Poissonian Electric field & Potential	$\rho_v = \rho_1 + \rho_2$ Space charge density =Positive ion density+negative ion density	ρ_s Surface charge density	P \mathbf{u} Pressure & Velocity

In the DBD actuator model, two “transport of diluted species” interfaces are applied to simulate the movement of positive ions and negative ions. The space charge density is the sum of the positive ion density and negative ion density. The surface charges accumulated on the dielectric surface are also taken into consideration. Due to the presence of surface charge, the electric field above and below the dielectric surface is different. We assume that the space charge above the dielectric would deposit as surface charge. When the y component of the electric field above the dielectric surface is negative, the positive ions will be driven by the electric force to the surface, otherwise, the negative ions will deposit on the dielectric surface. The mechanism can be mathematically expressed as

$$\mathbf{n} \cdot \mathbf{J}_e = 0 \quad (\text{A.1})$$

$$\mathbf{n} \cdot \mathbf{J}_i = -\mu_c \cdot \text{up}(E_y) * \text{if}(\text{up}(E_y) < 0, \rho_1, \rho_2) \quad (\text{A.2})$$

Since electron is neglected, the electron current density J_e is 0, while the ion current density is not. In the Equation A.2, μ_c is the ion mobility, which is assumed the same for positive and negative ions, $u_p(E_y)$ is the y component of the electric field above the dielectric surface, ρ_1 and ρ_2 are the charge density of positive ion and negative ion, respectively.

Table 5 Boundary conditions in the DBD actuator model

Boundaries	Poissonian electric field	Positive charge	Negative charge	Laminar flow
1, 2, 3, 17, 18 Outer boundary	$n \cdot D = 0$ Zero charge	$-n \cdot D_i \nabla C_i = 0$ Outflow	$-n \cdot D_i \nabla C_i = 0$ Outflow	N/A
8 Outer boundary	$n \cdot D = 0$ Zero charge	$-n \cdot D_i \nabla C_i = 0$ Outflow	$-n \cdot D_i \nabla C_i = 0$ Outflow	$\mathbf{u} = \mathbf{u}_0$ Inlet
7, 12 Dielectric surface	$\frac{\partial \rho_s}{\partial t} = n \cdot J_i + n \cdot J_e$ $-n \cdot (D_1 - D_2) = \rho_s$ Surface charge density	$-n \cdot D_i \nabla C_i = 0$ Outflow	$-n \cdot D_i \nabla C_i = 0$ Outflow	$\mathbf{u} = 0$ No slip wall
4, 5, 15 Dielectric plate	N/A	$-n \cdot \mathbf{N}_i = 0$ No flux	$-n \cdot \mathbf{N}_i = 0$ No flux	N/A
22 Discharge electrode tip	$V = V_0$ Electric Potential	$c_1 = c_{0,1}$ Inflow	$c_2 = c_{0,2}$ Inflow	$\mathbf{u} = 0$ No slip wall
11, 20 Upside of discharge electrode	$V = V_0$ Electric Potential	$c_1 = 0$ Concentration	$c_2 = 0$ Concentration	$\mathbf{u} = 0$ No slip wall
10, 19, 21	$V = V_0$ Electric Potential	N/A	N/A	N/A

Downside of discharge electrode				
13, 14, 23, 24, 25, 26 Grounded electrode	$V = 0$ Ground	N/A	N/A	N/A
6 Auxiliary line	N/A	N/A	N/A	$\mathbf{u} = \mathbf{u}_0$ Inlet
16 Auxiliary line	N/A	N/A	N/A	$[-P_0 + \mu(\nabla \mathbf{u} + (\nabla \mathbf{u})^T)] \mathbf{n}$ $= P_0 \mathbf{n}, P_0 = 0$ Outlet, zero pressure

Table 5 shows the boundary conditions in the DBD actuator model. In order to have a clear and all-inclusive view, these boundaries are categorized into a few groups. It can be found that the boundary conditions in the “positive charge transport” are very similar to those in the “negative charge transport”. The difference between them is on the discharge electrode tip. In the positive discharge phase, positive ions are produced near the tip and then they flow into the whole domain. In the negative discharge phase, negative ions are produced and then distributed over the whole domain. The amount of produced ions are determined by a MATLAB routine based on Kaptzov’s hypothesis and Peek’s formula.

Please note that the boundaries 4, 5, and 15 should have the same boundary conditions as boundaries 7 and 12. However, most of surface charges are accumulated on the boundaries 7 and 12. In order to simplify the model, the surface charge density on the boundaries 4, 5 and 15 is neglected.

The boundaries 6 and 16 are boundary of domain 3. We only consider the airflow in the domain 3 to reduce the calculation time. In addition, if the airflow is simulated in all domains, the presence of the dielectric plate would create some vortices when the air molecules bump into its edge. The disturbance of airflow created by the dielectric plate would make it hard to analyze to influence of DBD on the airflow acceleration.

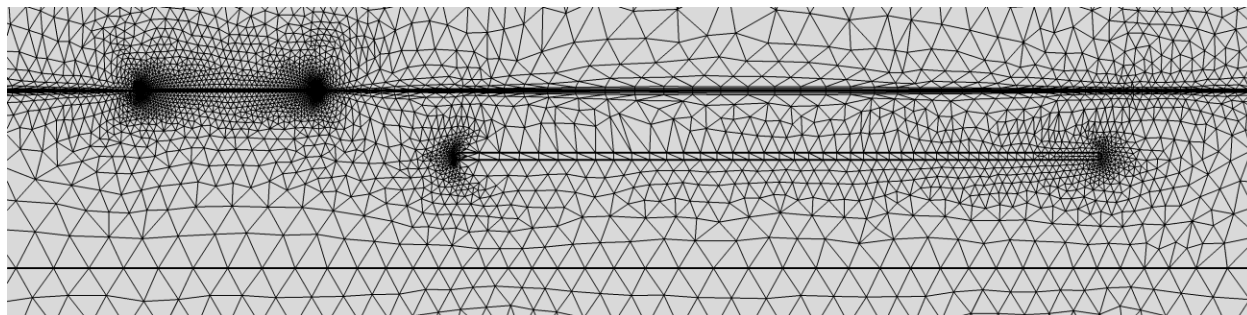


Figure A. 5 Mesh of the DBD actuator model

The entire domain is discretized into 15908 triangular elements and 1180 quadrilateral elements with an average element quality of 0.8109. The same as the EHD dryer model, even though the simulation results match with the experimental data pretty well, the numerical model might still require a mesh independence study in order to generate more accurate results.

The DBD actuator is powered by an AC voltage as:

$$V_{ap} = V_{max} \cdot \sin(2\pi f \cdot t) \quad (\text{A.3})$$

Therefore, the performance of the DBD actuator can be affected by the voltage level V_{max} and frequency f . Since the applied voltage changes over time, the model needs to be calculated with a time-dependent solver. In this model, the electric field, space charge and surface charge are fully coupled, and solved with a direct solver MUMPS. This model can also be solved with segregated steps and other solvers such as PARDISO and SPOOLES. A deeper understanding of the settings in COMSOL are required in order to speed up the calculation.

It takes approximately 5 voltage cycles to reach electric stability and at least 30 cycles to reach mechanical stability. This model is simulated from 0 ms to 50 ms with a time step of 0.02ms when the frequency is 1 kHz. It takes more than 6 hours to run one case. The computing time would exponentially increase when a parametric study is conducted.

3. Extended DBD Actuator

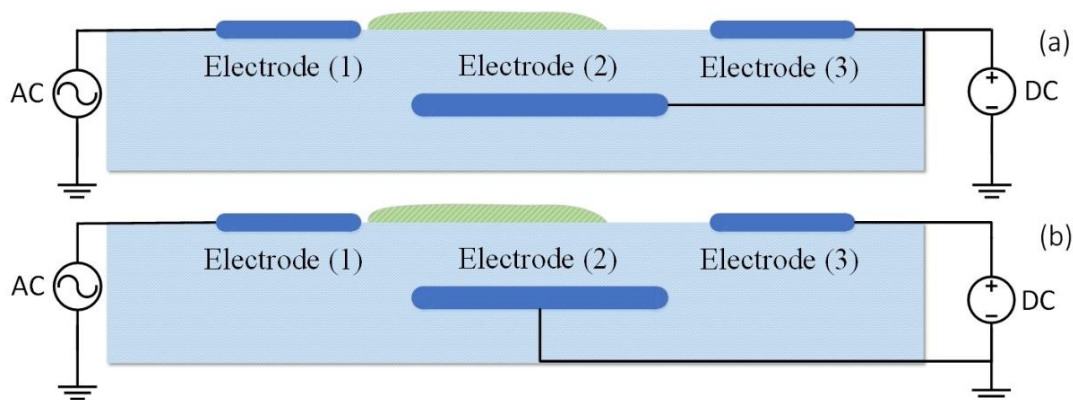


Figure A. 6 Unscaled sketch of the extended DBD actuator in two configurations.

The extended DBD actuator model is developed based on the DBD model. However, there is a third electrode with specific boundary conditions in the extended DBD actuator, which results in the different performance.

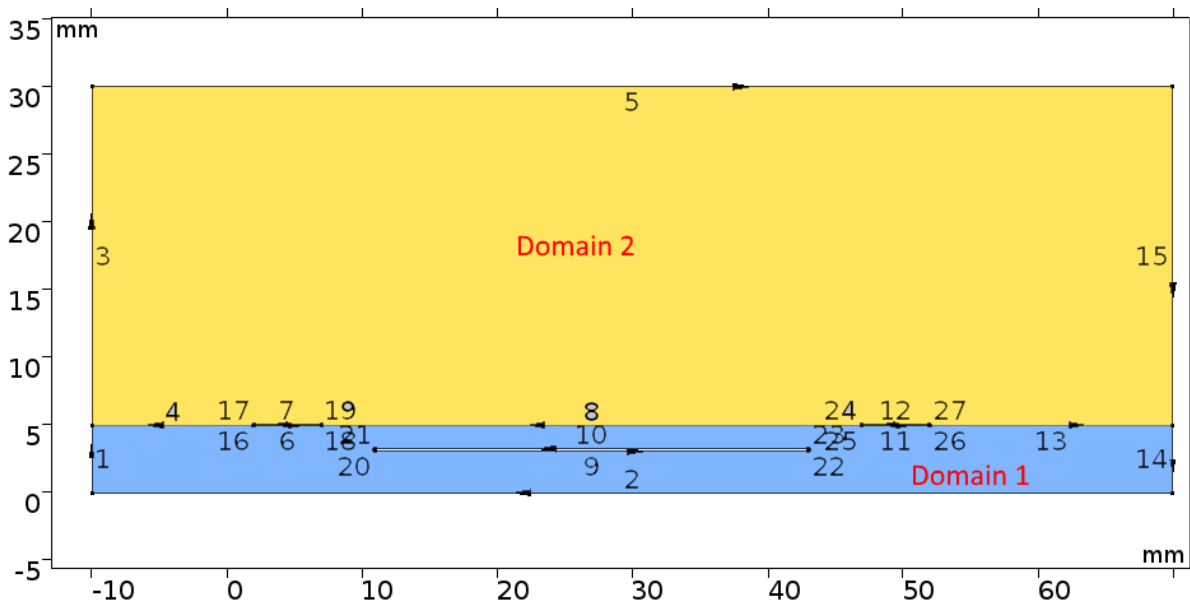


Figure A. 7 Calculation domain of the extended DBD actuator model.

The extended DBD model has been well polished. It has two domains, one for the dielectric plate and the other for the air space. The physics and the equations in this model are very similar to those in the traditional DBD actuator model.

Table 6 Physics and equations in the extended DBD actuator model

Physics	Poissonian electric field	Charge transport	Surface charge	Laminar flow
Equations	$\nabla \cdot \mathbf{D} = \rho_v$ $\mathbf{E} = -\nabla V$	$\nabla \cdot (-D_i \nabla c_i - z_i \mu_{m,i} F c_i \nabla V) = R_i$ $\mathbf{N}_i = -D_i \nabla c_i - z_i \mu_{m,i} F c_i \nabla V$	$\frac{\partial \rho_s}{\partial t} = \mathbf{n} \cdot \mathbf{J}_i + \mathbf{n} \cdot \mathbf{J}_e$ $-\mathbf{n} \cdot (\mathbf{D}_1 - \mathbf{D}_2) = \rho_s$	$\rho(\mathbf{u} \cdot \nabla) \mathbf{u} = \nabla \cdot [-p \mathbf{I} + \mu(\nabla \mathbf{u} + (\nabla \mathbf{u})^T)] + \mathbf{F}$ $\rho \nabla \cdot (\mathbf{u}) = 0$ $\mathbf{F} = \rho_v \cdot \mathbf{E}_p$
Initial value	$V=0$	$\rho_v=0$	$\rho_s=0$	$P = 0$ (relative) $u = 0$
Domains	1 & 2	2	Interface between 1 & 2	2
Features	E_p V_p Poissonian Electric field & Potential	$\rho_v = \rho_1 + \rho_2$ Space charge density = Positive ion density + negative ion density	ρ_s Surface charge density	P u Pressure & Velocity

As shown in Figure A.6, the electrode (2) can be either grounded or connected to a positive DC voltage. The boundary conditions in these two models are different on the electrode (2). Table 7 shows the boundary conditions for 26 boundaries included in the model.

Table 7 Boundary conditions in the extended DBD actuator model

Boundaries	Poissonian electric field	Positive charge	Negative charge	Laminar flow
3 Outer boundary	$\mathbf{n} \cdot \mathbf{D} = 0$ Zero charge	$-\mathbf{n} \cdot D_i \nabla c_i = 0$ Outflow	$-\mathbf{n} \cdot D_i \nabla c_i = 0$ Outflow	$[-p \mathbf{I} + \mu(\nabla \mathbf{u}_2 + (\nabla \mathbf{u}_2)^T)] \mathbf{n}$ $-\mathbf{f}_0 \mathbf{n}, f_0 = 0$ Open Boundary
5 Outer boundary	$\mathbf{n} \cdot \mathbf{D} = 0$ Zero charge	$-\mathbf{n} \cdot D_i \nabla c_i = 0$ Outflow	$-\mathbf{n} \cdot D_i \nabla c_i = 0$ Outflow	$[-p \mathbf{I} + \mu(\nabla \mathbf{u}_2 + (\nabla \mathbf{u}_2)^T)] \mathbf{n}$ $-\mathbf{f}_0 \mathbf{n}, f_0 = 0$ Open Boundary
15	$\mathbf{n} \cdot \mathbf{D} = 0$ Zero charge	$-\mathbf{n} \cdot D_i \nabla c_i = 0$ Outflow	$-\mathbf{n} \cdot D_i \nabla c_i = 0$ Outflow	$[-p \mathbf{I} + \mu(\nabla \mathbf{u}_2 + (\nabla \mathbf{u}_2)^T)] \mathbf{n}$

Outer boundary				$-f_0 \mathbf{n}$, $f_0 = 0$ Open Boundary
1, 2, 14 Dielectric plate	$\mathbf{n} \cdot \mathbf{D} = 0$ Zero charge	N/A	N/A	N/A
4, 8, 13 Dielectric surface	$\frac{\partial \rho_s}{\partial t} = \mathbf{n} \cdot \mathbf{J}_i + \mathbf{n} \cdot \mathbf{J}_e$ $-\mathbf{n} \cdot (\mathbf{D}_1 - \mathbf{D}_2) = \rho_s$ Surface charge density	$-\mathbf{n} \cdot D_i \nabla c_i = 0$ Outflow	$-\mathbf{n} \cdot D_i \nabla c_i = 0$ Outflow	$\mathbf{u} = \mathbf{0}$ No slip wall
19 Tip of the electrode (1)	$V = V_{AC}$ Electric Potential	$c_1 = c_{1,1}$ Inflow	$c_2 = c_{1,2}$ Inflow	$\mathbf{u} = \mathbf{0}$ No slip wall
7, 17 Upside of discharge electrode (1)	$V = V_{AC}$ Electric Potential	$c_1 = 0$ Concentration	$c_2 = 0$ Concentration	$\mathbf{u} = \mathbf{0}$ No slip wall
6, 16, 18 Downside of discharge electrode (1)	$V = V_{AC}$ Electric Potential	N/A	N/A	N/A
24 Tip of the electrode (3)	$V = V_{DC}$ Electric Potential	$c_1 = c_{3,1}$ Inflow	$c_2 = c_{3,2}$ Inflow	$\mathbf{u} = \mathbf{0}$ No slip wall
12, 27 Upside of discharge electrode (3)	$V = V_{DC}$ Electric Potential	$c_1 = 0$ Concentration	$c_2 = 0$ Concentration	$\mathbf{u} = \mathbf{0}$ No slip wall
11, 25, 26 Downside of discharge electrode (3)	$V = V_{DC}$ Electric Potential	N/A	N/A	N/A
9, 10, 20, 21, 22, 23	$V = \mathbf{0}$ or $V = V_{DC}$ Ground	N/A	N/A	N/A

**Grounded
electrode**



The traditional DBD model is simulated in cases with different external flows. However, as a primary study, the extended DBD model is investigated in the case with zero external flow. Therefore, the boundary conditions of 3, 5 and 15 are set as open boundary. In addition, the boundary conditions of the electrode (2) (including boundaries 9, 10, 20, 21, 22 and 23) have significant influence on the performance of the actuator.

When the electrode (2) is connected to the DC voltage, there should never have discharge on the electrode (3). However, if the electrode (2) is grounded and the DC voltage is above a critical value, a positive discharge would occur between electrodes (2) and (3). The amount of the positive ion is determined by a MATLAB routine, which is very similar to the MATLAB routine applied on the boundary 19.

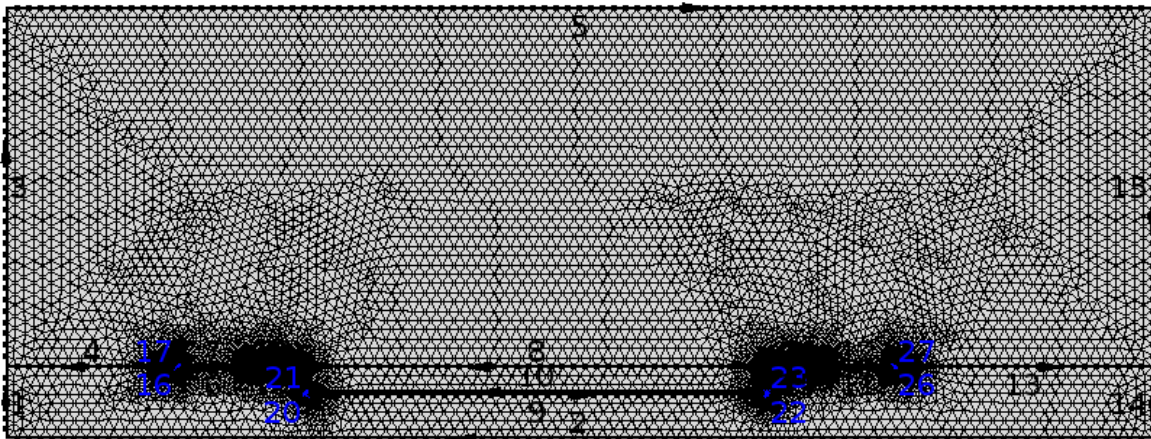


Figure A. 8 Mesh of the extended DBD model

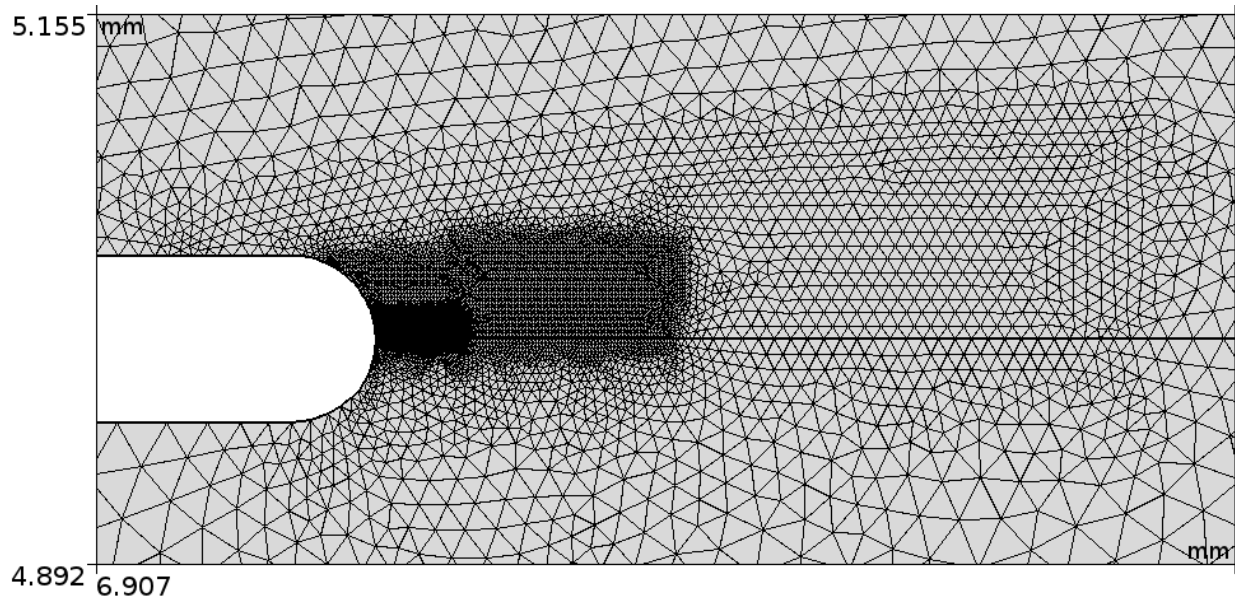


Figure A. 9 Zoomed view of the mesh near the tip of electrode (1)

Figures A.8 and A.9 show the mesh of the extended DBD model. The mesh is extremely fine in the region close to the electrode tips. The whole geometry is discretized into 67,917 triangular elements, 1,563 edge elements and 24 Vertex elements. The average element quality is 0.89, which is higher than that in the traditional DBD model.

The model also needs to be solved with a time dependent solver. The setting of the solver in this model is the same to that in the traditional DBD model. It would take more than 8 hours to run one case.

Curriculum

Vitae

Name: Chaoao Shi

Post-secondary Education and Degrees: Zhejiang University
Hangzhou, Jiangsu, China
2011-2015 B.E.

Western University
London, Ontario, Canada
2016-2018 M.Sc.

Honors and Awards: Award for Outstanding Graduate Symposium Presentation
Western University
May 2017

First Place Best Presentation Award at ESA Conference
University of Ottawa, ON, Canada
June 2017

Related Work Experience

Teaching Assistant
Western University
2016-2017

Research Assistant
Western University
2016-2017

Publications:

C.A. Shi, A. Martynenko, T. Kudra, P. Wells, K. Adamiak, and G. S. P. Castle, "Electrically-induced mass transport in a multiple pin-plate electrohydrodynamic (EHD) dryer." *Journal of Food Engineering*, 211, pp: 39-49, Oct. 2017.

C.A. Shi, K. Adamiak, and G. S. P. Castle, "Numerical study of the characteristics of a dielectric barrier discharge plasma actuator", *Journal of Physics D: Applied Physics*, 51, 095201, 2018

Conferences:

C.A. Shi, K. Adamiak, and G. S. P. Castle, "Electrostatic Characteristics of DBD Investigated using a Numerical Model", *presented in Annual Meeting of Electrostatic Society of America (ESA), Ottawa, Canada, June 2017.*

C.A. Shi, K. Adamiak, and G. S. P. Castle, "Numerical Simulation of a DBD Actuator for Airflow Control", *presented in International Symposium on Electrohydrodynamics (ISEHD), Ottawa, Canada, June 2017.*